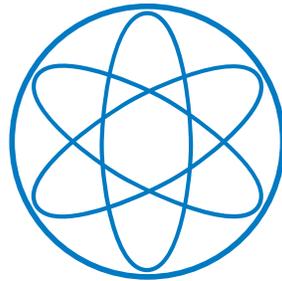PHYSIK-DEPARTMENT

Equatorial Wave Dynamics

Diploma Thesis
by
Emanuel Schmidt

TECHNISCHE UNIVERSITÄT MÜNCHEN

Acknowledgments

Foremost, I am very grateful to my advisors at the Royal Netherlands Institute for Sea Research (NIOZ), Prof. Dr. Leo Maas and Anna Rabitti, for the endless time they spent supporting me and for their motivation and their enthusiasm.

I would like to thank my advisor at TUM, Prof. Dr. Leo van Hemmen, for giving me the opportunity to write this thesis abroad, for his encouragement to this project and particularly for introducing me to Prof. Dr. Leo Maas.

My special thanks go to all my colleagues at NIOZ and my fellows living at residence De Potvis for the good times. I have been fortunate that the NIOZ funded my internship, particularly the accommodation. Furthermore, I would like to acknowledge the help I received from the staff at the International Office of TUM with the formalities of the ERASMUS scholarship.

This thesis would not have been possible without back up from my family, and especially from my wife Lucia.

Contents

List of Symbols

Only basic symbols that keep their meaning throughout the whole thesis are listed here. Symbols that are used locally are explained in the respective context.

$\vec{u}$	Velocity vector
r_0	Mean Earth radius
$\Omega, \vec{\Omega}$	Angular frequency and angular velocity of the Earth's rotation
$g, \vec{g}$	Gravitational acceleration, gravity vector
$\varrho_*, \varrho_0, \varrho'$	Reference density, hydrostatic density, density perturbation
$p, p_0, \tilde{p}$	Pressure, hydrostatic pressure, dynamical pressure $p - p_0$
b	Buoyancy acceleration, see eq. (2.2.3)
N	Buoyancy frequency, see eq. (2.4.3)
λ, φ, r	Longitude, latitude and radial coordinate, see figure 2.1
u, v, w	Zonal, meridional and vertical velocity components, see figure 2.1
$f, \tilde{f}$	Traditional Coriolis parameter $2\Omega \sin \varphi$, nontraditional Coriolis parameter $2\Omega \cos \varphi$
β	The $\beta-$plane parameter, $\beta = 2\Omega/r_0$ at the Equator
H, D	Real water depth, mean water depth, see figure 2.2
η, h_b	Sea surface elevation, bottom topography, see figure 2.2
L	Typical horizontal or zonal length scale
U	Typical horizontal or zonal velocity scale
$\hat{}$	Hats mark dimensionless quantities
δ	Aspect ratio, see eq. (2.7.2)
Ro	Rossby number, see eq. (2.7.2)
ω, k	Angular frequency, wavenumber
$c_{\text{ph}} \equiv c, c_{\text{gr}}$	Phase velocity $c_{\text{ph}} = \frac{\omega}{k}$, group velocity $c_{\text{gr}} = \frac{\partial \omega}{\partial k}$
ψ	Stream function
ν	Kinematic viscosity

Chapter 1

Introduction

If one visualizes the Earth as a whole, likely the picture of a blue marble arises which is well-known from space images. Both a marble and the Earth are almost spherical, and spheres are the most symmetric geometric objects. Hence, one is tempted to think that the global ocean circulation obeys some spherical symmetries, but this is not true in general. Owing to the shape of the continents, the circulation patterns in the Northern Hemisphere and the Southern Hemisphere are very different.

In the North, a characteristic contribution to the global circulation is the formation of deep water. Highly saline and warm surface water that is transported northwards starts sinking as soon as it is cooled down in the arctic regions. On the Southern Hemisphere, the Antarctic Circumpolar Current that flows clockwise from west to east around Antarctica constitutes the largest ocean current on Earth. It is mainly driven by the Westerlies and reaches its magnitude due to the absence of continental boundaries south of Cape Hoorn.

Of course, the role of the tropical ocean as a coupler between these two unequal regions is crucial. It is however often ignored in this context that the equatorial area has its own dynamics and its own typical phenomena which are yet far from being understood. From the observational point of view, this is mainly due to its huge extent, but also theoretical descriptions are challenging. For example, the approximation commonly used to simplify the Coriolis force breaks down in the equatorial region.

Many ocean models neglect these facts, and often a white stripe replaces the inadequate model outcome in this sector. In trying to provide tools towards a better understanding of the big picture, it seems thus promising to zoom in on equatorial dynamics and particularly on the role waves play in this field. This motivates the following study.

Some basic principles of equatorial oceanography as well as the governing equations for rotating fluids are briefly introduced in the sections 1.1 to 1.3. A detailed outline of the thesis can be subsequently found in section 1.4.

1.1 The equatorial ocean

Seawater is basically a diluted solution of ions. It is commonly characterized by its salinity S (typically about 3.5% in the open ocean) and its temperature T. Together with the pressure p that in first instance depends on depth, these two quantities determine the density ϱ of seawater.

The equatorial ocean may be defined as the region from about 5° South to about 5° North latitude. This reach is small compared to the extent in longitude, being larger than 120° for the Pacific and larger than 40° for the Atlantic. The sea is an important player in the Earth's climate system, contributing about one third to a half to the total polewards heat transport which is of the order of $PW = 10^{15}$ W. A considerable part of this heat passes through or even originates from the Tropics, as this region is warm year-round (Dijkstra, 2008).
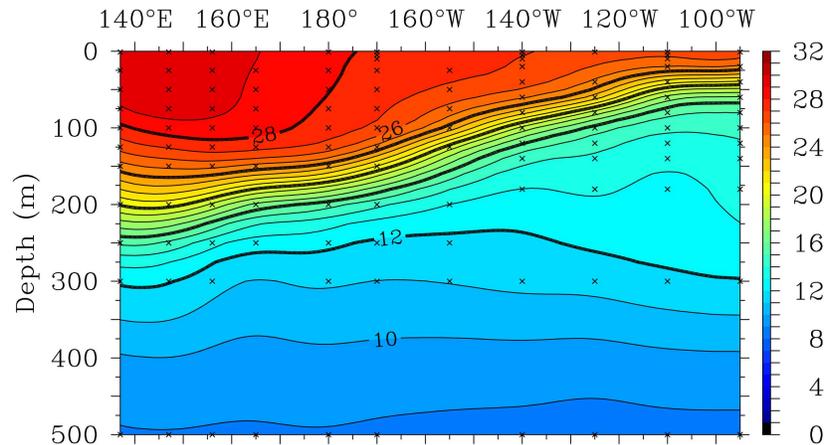
Figure 1.1: Mean temperature profile of the equatorial Pacific between 2ºN and 2ºS in April 2013 obtained from the TAO-buoys. The strong gradient in the yellowish region forming the thermocline can be seen clearly. Crosses indicate the measurement positions of the buoys (picture generated in May 2013 from original data on `http://www.pmel.noaa.gov/tao/`) .

In the following, three phenomena are presented that are typical for the Equator.

Equatorial thermocline. A thermocline is a thin transition region in which the temperature changes rapidly compared to the neighboring layers. As it can be seen from figure 1.1, there is a pronounced thermocline at the Equator represented by the strong temperature gradient around the 20°C isotherm (yellow). Its depth changes from about 250 m in the East to 50 m in the West, and this inclination is remarkable. In the conventional equatorial wave theory, the thermocline is modeled as interface between two fluid layers along which surface waves can travel, see chapter 3.

The data underlying figure 1.1 is obtained from moored sensors belonging to the Tropical Atmosphere Ocean project (TAO). The about 70 TAO-moorings in the tropical Pacific Ocean are sending continuously real-time oceanographic data to shore.

Sea surface height. Satellites are a powerful tool for global long-term observations of the sea surface. In 1992, the satellite altimeter TOPEX/POSEIDON became fully operational, running a 10-day orbiting cycle and enabling sea level measurements with an accuracy of about 4 cm by means of radar altimetry. After appropriate filtering, large-scale sea level signals with amplitudes down to 1 cm can be detected (Chelton and Schlax, 1996). The mission produced continuous data over years, ending only in 2006.

Disturbances on the sea surface can be related to waves. These are not necessarily surface waves, as will be discussed in chapter 3 where also some observational results will be shown.

Equatorial deep jets. Figure 1.2 shows a typical equatorial zonal (longitudinal) current profile. Going down in depth, strong east-west currents are found that alternate in sign. These are the Equatorial Deep Jets which are trapped within about 1° off the Equator and extend a few hundred meters in the vertical, see Dengler and Quadfasel (2002). They are found in all equatorial basins, and their generation is often attributed to waves reaching their maxima in the interior of the fluid but the detailed mechanism is not understood yet. According to Brandt et al. (2011), the Atlantic Deep Jets oscillate on an inter-annual time scale, whereas the oscillatory behavior in the other oceans remains unclear at the moment.

Current profiles like the one in figure 1.2 are taken by means of Acoustic Doppler Current Profilers (ADCPs), which can be moored or be lowered from ships (LADCP). Further conclusions on the
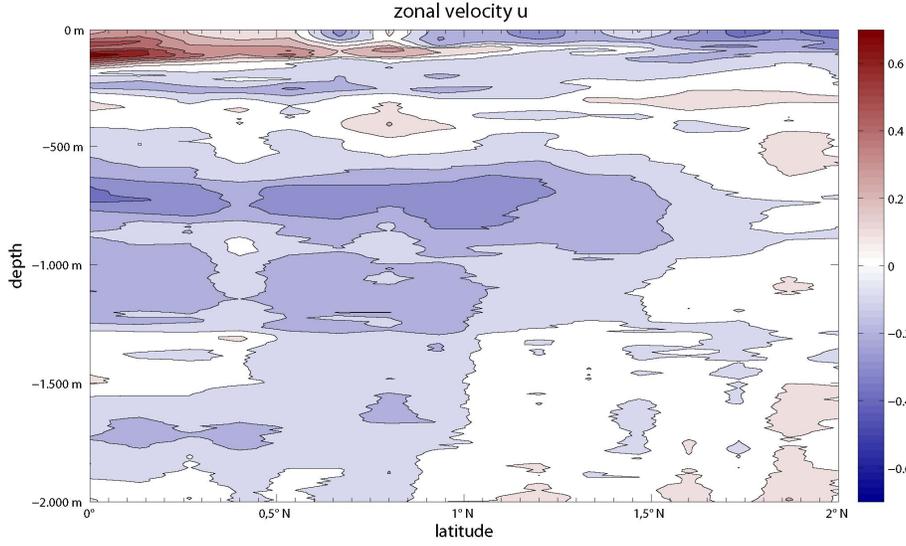
Figure 1.2: Unfiltered zonal (longitudinal) velocity profiles from LADCP measurements north of the Equator. Current structures characteristically alternating in sign constitute the equatorial deep jets, like the deep-red eastward Equatorial Under Current (EUC) at around 100 m depth, and the strong westward Equatorial Intermediate Current (EIC) at around 700 m depth.. The data was taken during cruise 64PE279 of the NIOZ Research Vessel Pelagia in winter 2007 led by Hans van Haren.

current velocities can be drawn from the data of floaters belonging to the WOCE and ARGO projects. According to Dengler and Quadfasel (2002), zonal (longitudinal) and meridional (latitudinal) velocities are of $\mathcal{O}(10\,\frac{\text{cm}}{\text{s}})$ down to thousands of meters which is a particularly high value for deep currents. The maximum zonal velocities in the jets can even be a little bit higher. Vertical velocities are typically of $\mathcal{O}(0.1\,\frac{\text{cm}}{\text{s}})$ and hence much lower.

All three effects involve waves as agents propagating disturbances. Moreover, they are thought to play a role in coupled atmosphere-ocean phenomena like El Niño in the Pacific (see the review of Dijkstra and Burgers, 2002) and the climate variability of the tropical Atlantic (see Brandt et al., 2011). The detailed description of these couplings is however beyond the scope of this work, and the reader may be referred to the literature.

1.2 The full set of equations

From a physicist's point of view, the dynamics of the ocean are described by five equations that connect the five variables speed $\vec{u}$, density ϱ, pressure p, temperature T and salinity S to each other:

$$\varrho \frac{D\vec{u}}{Dt} = -\nabla p - \varrho \nabla \Phi^* + \mathcal{F} \tag{1.2.1a}$$

$$\frac{D\varrho}{Dt} + \varrho \operatorname{div}\vec{u} = 0 \tag{1.2.1b}$$

$$\varrho = \varrho(p, T, S) \tag{1.2.1c}$$

$$\varrho \frac{DT}{Dt} = \nabla \cdot (\varrho K_T \nabla T) + \frac{Q_T}{C_p} \tag{1.2.1d}$$

$$\varrho \frac{DS}{Dt} = \nabla \cdot (\varrho K_S \nabla S) + Q_S \tag{1.2.1e}$$

Here, $\frac{D}{Dt} = \partial_t + (\vec{u}_R \cdot \nabla)$ is the material derivative[1] resulting from the usage of an Eulerian velocity field. The first equation describes momentum conservation, involving the gravitational potential Φ^* with $-\nabla \Phi^* = \vec{g}$, where $\vec{g}$ is the gravity vector. The shorthand notation

$$\mathcal{F} = (\lambda + \mu)\nabla(\nabla \cdot \vec{u}) + \mu \triangle \vec{u} + \vec{f}_V$$

is used for the friction terms and a possible external forcing $\vec{f}_V$. The Lamé parameters λ and μ result from the assumption of linear elasticity, as explained in detail in Chorin (1992). These terms however will be neglected mostly in the following, which results in the Euler equation that allows an easier first access to many relevant phenomena. Consequently, also the boundary conditions have to be simplified as one is dealing with a first order PDE. The second equation expresses the conservation of mass.

A general problem in the physical description of the oceans appears in equation (1.2.1c): there is no exact expression for the equation of state of seawater, relating the density ϱ to the state variables p, T and S. However, there are good empirical formulas resulting from fits on experimental data, and a simple, linear approximation may be sufficient to demonstrate some main features, as described in Dijkstra (2008).

The last two equations (1.2.1d) and (1.2.1e) express the conservation of energy and salinity, stated in a standard form that is widely used in physical oceanography, see for example Gill (1982). The diffusion coefficients for the diffusive fluxes $\nabla \cdot (\varrho K_F \nabla F)$ of temperature and salt are denoted by K_T and K_S, C_p is the heat capacity and Q_T and Q_S represent the source terms of temperature and salinity, respectively. Examples for such processes are precipitation, evaporation, freshwater outflow from rivers or heating due to radiation.

The formulation of appropriate boundary conditions is another crucial ingredient completing the system (1.2.1a)-(1.2.1e). As they depend strongly on the particular problem under consideration, this will be done case by case at a later stage.

1.3   Fictitious forces in a co-rotating frame

Since the Earth is rotating and observations are made on the Earth in most of the cases, the equations have to be transformed to the co-rotating frame, which will be done in this section. A rotation around a fixed axis $\vec{\Omega} = f(\vec{X}_0, t) \cdot \vec{\Omega}_0$ that may vary in strength with position and time is described by a velocity

$$\frac{d\vec{X}}{dt} \equiv \vec{U} = \vec{\Omega} \times \vec{X}.$$

Using the fact that a vector cross-product can be written as a multiplication by an antisymmetric matrix $R \in M(3 \times 3)$, one can rewrite this differential equation and give a formal solution,

$$\frac{d}{dt}\vec{X} = f(\vec{X}_0, t) R_0 \vec{X} \qquad \Rightarrow \qquad \vec{X} = \vec{X}_0 e^{\int_{t_0}^{t} f \, dt' R_0}.$$

Note that for arbitrary $\vec{\Omega}(\vec{X})$, the system will be not integrable, besides from special cases considered in the theory of spinning tops.

Consider now a coordinate transformation $\vec{x}_I = \vec{X} + x_R^i \hat{e}_i$ from the inertial frame I to a co-rotating frame R at position $\vec{X}$. Here, $\hat{e}_i$ denotes the $i-$th unit vector of the co-rotating frame R. As the unit vectors of this frame change according to $\frac{d\hat{e}_i}{dt} = \vec{\Omega} \times \hat{e}_i$, the velocity can be written as

$$\vec{u}_I \equiv \frac{d\vec{x}_I}{dt} = \frac{d\vec{X}}{dt} + \frac{dx_R^i}{dt}\hat{e}_i + x_R^i \frac{d\hat{e}_i}{dt} = \vec{\Omega} \times \vec{X} + \vec{u}_R + x_R^i(\vec{\Omega} \times \hat{e}_i).$$

The velocity $\vec{u}_R \equiv \frac{dx_R^i}{dt}\hat{e}_i$ is the velocity observed in the rotating frame. The acceleration is then found to be

$$\vec{a}_I \equiv \frac{d\vec{u}_I}{dt} = (\frac{d}{dt}\vec{\Omega}) \times \vec{x}_I + \vec{\Omega} \times (\vec{\Omega} \times \vec{x}_I) + 2(\Omega \times \vec{u}_R) + \vec{a}_R. \tag{1.3.1}$$

---

[1]In the following, partial derivatives $\frac{\partial f}{\partial x}$ are denoted more compact as $\partial_x f$ or simply f_x.

The first three terms represent the *fictitious forces* modifying the acceleration $\vec{a}_R = \frac{d\vec{u}_R}{dt}$ observed in the rotating frame:

- The first term represents the Euler force caused by changes of rotation strength in time. Note that it still depends on $\vec{x}_I = \vec{X} + \vec{x}_R$.

- The second term is the centrifugal force, pointing outwards perpendicularly to the rotation axis, and it can be written

$$-\vec{\Omega} \times (\vec{\Omega} \times \vec{x}_I) = \frac{\Omega^2}{2}\nabla x_I^2 - \vec{\Omega}(\vec{\Omega} \cdot \vec{x}_I) \tag{1.3.2}$$

- The third term is called the Coriolis force, which is caused by the change of the unit vectors in time. This force applies to movement relative to the co-rotating frame.

The tiny variations of the Earth's rotation in space and time are neglected in the following. Assuming that the angular speed vector is constant in time and space, it reads consequently $\vec{\Omega} = \Omega_\oplus \hat{e}_z$ and the Euler force vanishes and the centrifugal force eq. (1.3.2) can be written as a gradient of a potential,

$$-\vec{\Omega} \times (\vec{\Omega} \times \vec{x}_I) = \frac{1}{2}\nabla\left(\Omega^2(x_I^2 - z^2)\right).$$

Making the transition to the Euler picture, the velocity $\vec{u}_R(\vec{x}_0, t)$ becomes the velocity field $\vec{u}_R(\vec{x}_R, t)$, and the material derivative $\frac{D}{Dt} = \partial_t + (\vec{u}_R \cdot \nabla)$ has to be used instead of the ordinary time derivative. The momentum equation (1.2.1a) reads in the rotating frame

$$\frac{D\vec{u}_R}{Dt} + 2(\vec{\Omega} \times \vec{u}_R) = -\frac{1}{\varrho}\nabla p + \nabla\Phi + \frac{1}{\varrho}\mathcal{F}, \tag{1.3.3}$$

where the *geopotential* $\Phi(\vec{x}_I) = \Phi^* - \frac{\Omega^2}{2}(x_I^2 - z^2)$ was introduced by combining the gravitational potential and the centrifugal potential. Eq. (1.3.3) constitutes together with eq. (1.2.1b)-(1.2.1e) the full set of governing equations in a co-rotating frame.

1.4 Aim and outline of the thesis

The aim of this work is the systematic study of the different types of waves occurring at the Equator, accounting for the mathematical and dynamical peculiarities characterizing the low latitudes. Adequate simplified sets of equations shall be derived from the governing equations and analytical solutions to those sets of equations shall be sought. Where appropriate, numerical techniques will be applied or improved that allow comparison to other approaches.

By doing so, one main goal is to include the full Coriolis force and hence, to overcome the so-called *traditional approximation*. The latter is commonly used in geophysical fluid dynamics. It basically neglects the angular velocity components of the Earth's rotation that are perpendicular to the radius vector originating from the Earth's center, which contribute however most to the Coriolis force at the Equator.

The study is thought to be a continuation and a complement to work already done or ongoing at NIOZ by means of geometrical construction principles (Harlander and Maas, 2007) and ray tracing. Therefore, it spares these techniques and furthermore, it focuses on linear and mainly on inviscid theory. Various other methods like stream function-based approaches, boundary layer solutions and numerical approximations are used instead. Moreover, the thesis shall be self-contained in a sense that it is accessible not only to experts in this field but to any interested physicist.

Outline of the thesis.   In this chapter, the most basic principles of equatorial wave dynamics were introduced. Chapter 2 presents the fundamental approximations used in physical oceanography, which come along with many denominations commonly used in this subject. Moreover, a suitable coordinate system and different possible boundary conditions are introduced.

Waves in this field basically split into two classes, and this classification is reflected in the structure of the thesis. Three chapters are dedicated to surface waves (and interface waves), which constitute the first class. Chapter 3 introduces the standard textbook approach to equatorial waves attributed to Matsuno (1966) and discusses its limitations. Chapter 4 inspects to what extent equatorial Kelvin waves, a concept from chapter 3, can be generalized to a nontraditional setting. This allows for a comparison to recent results by other authors. Chapter 5 attempts a similar generalization for surface waves with nonzero meridional velocity, which are the counterpart of equatorial Kelvin waves in the customary textbook approach. Again, the findings are compared to recent results by others.

The second class of waves are internal waves, and they are the subject of the subsequent three chapters. Chapter 6 presents their main properties, points out the difficulties arising in our context by means of the work of Stewartson and Rickard (1969) and introduces the concept of wave attractors on the basis of a particular example. Chapter 7 puts Stern's equation forward as the natural relation describing internal waves at the Equator, discusses its solvability in an inviscid setting and compiles a boundary layer solution. Chapter 8 is dedicated to numerical solutions of this equation. An enhanced version of an existing method reveals its deficiency, a new method is presented that overcomes this problem and finally, forcing is exemplarily taken into account. Finally, chapter 9 provides a summary and an outlook.

Chapter 2

Common approximations

Unfortunately, the full set of equations (1.3.3) and (1.2.1b)-(1.2.1e) turns out to be extremely difficult to solve, not only in terms of analytic solutions but also numerically. Already the question whether and under which conditions smooth solutions to the three-dimensional Navier-Stokes equation exist is still open. While one is interested in analytic solutions to better understand the underlying principles, even numerical models need simplifications to keep the computational effort reasonable. In this chapter, the different sets of equations studied in the remaining chapters are derived, starting from the full set of equations. For example, an important simplification could be achieved by combining geopotential and pressure in eq. (1.3.3) into one common potential, which leads to the Boussinesq approximation.

The approximations presented in this chapter are commonly used in physical oceanography. It is indispensable to introduce them properly in order to be able to find their limitations at a later stage.

2.1 The Boussinesq approximation

The Boussinesq approximation applies to fluids whose density varies only slightly around a fixed reference value. The basic idea is to neglect the influence of the density variations on the inertia terms. It is pointed out by many authors like, for example, LeBlond and Mysak (1978) that this assumption is realistic for seawater since the relative density changes are indeed of $\mathcal{O}(10^{-3})$. Therefore, ϱ is split into three parts: a constant reference density ϱ_* that could be for example a mean value, a stationary part $\varrho_0(\vec{x})$ reflecting the hydrostatic equilibrium and a (wave-induced) density perturbation $\varrho'(\vec{x}, t)$, according to

$$\varrho = \varrho_* + \varrho_0(\vec{x}) + \varrho'(\vec{x}, t) \qquad \text{where} \qquad \varrho_* \gg \varrho_0 \gg \varrho'. \tag{2.1.1}$$

The first inequality allows to do the actual approximation, whereas the latter inequality makes a subsequent linearization possible, which will be carried out in section 2.4.

Now consider the hydrostatic equilibrium state characterized by $\vec{u} \equiv 0$. In this case, the momentum equation simplifies, giving the hydrostatic equation

$$\nabla p_0 = - \left(\varrho_* + \varrho_0(r) \right) \nabla \Phi. \tag{2.1.2}$$

This relation defines thus the equilibrium pressure p_0. Subtracting it from eq. (1.3.3) and using the fact that $1 + \frac{\varrho_0 + \varrho'}{\varrho_*} \approx 1$, one finds

$$\frac{D\vec{u}_R}{Dt} + 2(\vec{\Omega} \times \vec{u}_R) = -\nabla \left(\frac{\tilde{p}}{\varrho_*} \right) - \frac{\varrho'}{\varrho_*} \nabla \Phi + \frac{1}{\varrho_*} \mathcal{F}. \tag{2.1.3}$$

In the latter equation, only the so-called dynamical part of the pressure, $\tilde{p} = p - p_0$ enters this equation. The index R will be dropped from now on at the velocity $\vec{u} \equiv \vec{u}_R$ as rotation will always be present in the following.

2.2   The anelastic approximation

The underlying idea is to treat seawater to be incompressible *on the time scales under consideration*. This is possible as the speed of sound $c_s = (1.5 \pm 0.7) \cdot 10^3 \frac{\text{m}}{\text{s}}$ is much faster than all processes we are interested in; the fluid adjusts in the whole domain quasi instantaneous to pressure changes. But in return, one has to restrict to isentropic processes in absence of diffusion. Then, eq. (1.2.1d) and eq. (1.2.1e) read $\frac{DT}{Dt} = 0$ and $\frac{DS}{Dt} = 0$, respectively, and by acting with the material derivative on the equation of state (1.2.1c), one obtains

$$\frac{D}{Dt}\varrho(p,T,S) = \left(\frac{\partial \varrho}{\partial p}\right)\frac{Dp}{Dt} + \left(\frac{\partial \varrho}{\partial T}\right)\frac{DT}{Dt} + \left(\frac{\partial \varrho}{\partial S}\right)\frac{DS}{Dt} = \left(\frac{\partial \varrho}{\partial p}\right)\frac{Dp}{Dt} \equiv \frac{1}{c_s^2}\frac{Dp}{Dt}. \qquad (2.2.1)$$

The definition $\left(\frac{\partial \varrho}{\partial p}\right) = \frac{1}{c_s^2}$ for the speed of sound has been used in the latter equation. Taking the limit $c_s \to \infty$ then gives

$$\frac{D\varrho}{Dt} = 0 \qquad \text{and thus} \qquad \text{div}\,\vec{u} = 0. \qquad (2.2.2)$$

This is the continuity equation for an incompressible fluid! Reinserting the expression eq. (2.1.1) for the density in eq. (2.2.2), the equation determining the density perturbation $\varrho'(\vec{x}, t)$ is found that closes the system again,

$$(\vec{u} \cdot \nabla)\,\varrho_0 + \frac{D\varrho'}{Dt} = 0.$$

This equation is mostly called the *buoyancy equation*, since it is often formulated in terms of the buoyancy $b(\vec{x}, t)$, reading

$$\frac{g}{\varrho_*}\,(\vec{u} \cdot \nabla)\,\varrho_0 + \frac{Db}{Dt} = 0, \qquad \text{where} \qquad b = g\frac{\varrho'}{\varrho_*}. \qquad (2.2.3)$$

Note that the friction terms simplify due to eq. (2.2.2), too, reading $\mathcal{F} = \mu\triangle\vec{u}_R + \vec{f}_V$ and leaving the dynamic viscosity μ as remaining parameter.

2.3   An appropriate coordinate system

One possible coordinate choice in order to describe the Earth's rotation is (λ, φ, r), where $\lambda \in [0, 2\pi]$ gives the longitude, $\varphi \in [-\pi/2, +\pi/2]$ gives the latitude and r is the distance to the Earth's center, see figure 2.1. They are connected to the spherical coordinates (λ, ϑ, r) used normally in physics via

$$\varphi = \frac{\pi}{2} - \vartheta \qquad \text{and hence} \qquad \hat{e}_\varphi = -\hat{e}_\vartheta.$$

The corresponding velocities are (u, v, w), where the *zonal* component u describes motion along a circle of latitude, the *meridional* component v describes movement along a meridian and a positive w describes movement directed outwards. If gravitational contributions of the moon and the sun are neglected and the Earth's mass is considered to be concentrated at the origin, the geopotential is given by

$$\Phi = g \cdot r - \frac{\Omega^2}{2}r^2 \cos^2\varphi.$$

Even when this simple form of the gravitational part is used, the equipotential surfaces are not spherical symmetric because of the centrifugal part. Indeed, the Earth is oblate also due to the centrifugal force, and the geoid[1] is more accurately fitted by an ellipsoid. Oblate spheroidal coordinates are a better choice, certainly for numerical models, but very inconvenient for analytic studies.

---

[1]The geoid is the equipotential surface of Φ obtained from gravimeters on satellites like GRACE and GOCE.
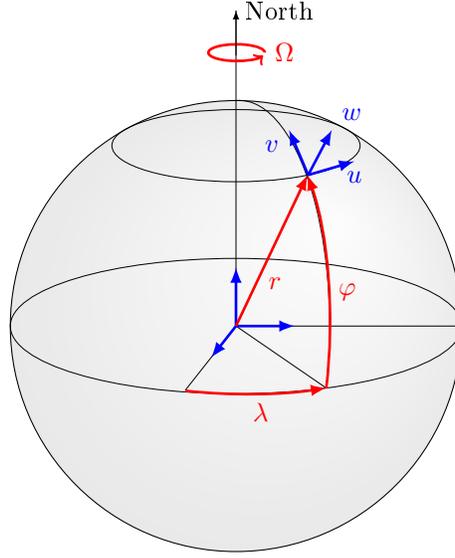
Figure 2.1: Spherical coordinates and velocity directions commonly used in physical oceanography. The correct order for a right-handed coordinate system is (λ, φ, r) and (u, v, w), respectively. The direction of λ is called the *zonal direction*, the direction of φ is called the *meridional direction*.

Spherical coordinates can however also be interpreted as the limit of oblate coordinates in case of small deformations. It is then reasonable to keep $\hat{e}_r \| \vec{g}$ in this limit by dropping the centrifugal term, such that the surface of the sphere still is an equipotential surface. For this reason, often *both* spherical coordinates are chosen and the centrifugal term in Φ is dropped to compensate for that. As the maximum of the centrifugal force, reached at the Equator, is $\Omega_\oplus^2 r_0 \approx 0.034\, \frac{\mathrm{m}}{\mathrm{s}^2} \ll g$, the associated errors are expected to be rather small. Then *the meaning of the coordinates changes* whereas the equations look the same, as pointed out in Olbers et al. (2012); Gill (1982).

Using the horizontal and vertical Coriolis parameters (or Coriolis frequencies) $f = 2\Omega \sin \varphi$ and $\tilde{f} = 2\Omega \cos \varphi$, respectively, the Coriolis term reads in the new coordinates

$$2\vec{\Omega} \times \vec{u} = 2\Omega \begin{pmatrix} -v \sin \varphi + w \cos \varphi \\ u \sin \varphi \\ -u \cos \varphi \end{pmatrix} = \begin{pmatrix} -fv + \tilde{f}w \\ fu \\ -\tilde{f}u \end{pmatrix}, \quad \text{where} \quad \vec{\Omega} = \begin{pmatrix} 0 \\ \Omega \cos \varphi \\ \Omega \sin \varphi \end{pmatrix}. \qquad (2.3.1)$$

The terms of the Coriolis force associated with f are usually called the *traditional terms*, as they are retained in the common approach. Likewise, the terms containing $\tilde{f}$ constitute the *nontraditional terms* since they are often dropped.

For the momentum equation (2.1.3) and the continuity equation (2.2.2), additional *curvature terms* appear due to the changes of the unit vectors to spherical coordinates. The transformation yields:

$$\frac{Du}{Dt} + \frac{uw}{r} - \frac{uv}{r} \tan \varphi - fv + \tilde{f}w \;=\; -\frac{1}{\varrho_* r \cos \varphi} \partial_\lambda \tilde{p} + \mathcal{F}_\lambda \qquad (2.3.2a)$$

$$\frac{Dv}{Dt} + \frac{wv}{r} + \frac{u^2}{r} \tan \varphi + fu \;=\; -\frac{1}{\varrho_* r} \partial_\varphi \tilde{p} + \mathcal{F}_\varphi \qquad (2.3.2b)$$

$$\frac{Dw}{Dt} - \frac{u^2 + v^2}{r} - \tilde{f}u \;=\; -\frac{1}{\varrho_*} \partial_r \tilde{p} - b + \mathcal{F}_r \qquad (2.3.2c)$$

$$w\frac{g}{\varrho_*}\partial_r\varrho_0 + \frac{Db}{Dt} \;=\; 0 \qquad\qquad (2.3.2\text{d})$$

$$\frac{1}{r\cos\varphi}\left(\partial_\lambda u + \partial_\varphi(v\cos\varphi)\right) + \frac{1}{r^2}\partial_r(r^2 w) \;=\; 0 \qquad\qquad (2.3.2\text{e})$$

Now, the buoyancy equation (2.3.2d) is included, and b is also used in eq. (2.3.2c). The terms $\mathcal{F}_{\lambda,\varphi,r}$ again denote the friction and forcing terms, but are now divided by ϱ_*. The material derivative now is given by

$$\frac{D}{Dt} = \partial_t + \frac{u}{r\cos\varphi}\partial_\lambda + \frac{v}{r}\partial_\varphi + w\partial_r.$$

In the appendix A.2, further details on spherical coordinates are listed.

2.4 The equatorial β-plane

An important concept to deal with curvature terms in oceanography is the $\beta-plane$, corresponding to a linearization of the trigonometric functions appearing in the governing equations. To do so, the coordinates are scaled for later convenience with respect to the mean Earth radius r_0 and a reference latitude φ_0 according to:

$$\begin{aligned}
x &= r_0\cos\varphi_0\lambda \\
y &= r_0(\varphi - \varphi_0) \\
z &= r - r_0
\end{aligned} \qquad\qquad (2.4.1)$$

Of course, $\varphi_0 = 0$ is chosen since the Equator is considered. A Taylor approximation up to first order around this point can be done for the trigonometric functions, i.e. $\sin\varphi \approx \varphi$ and $\cos\varphi \approx 1$. Furthermore, $\frac{r_0}{r} \approx 1$ can be assumed as the ocean forms a thin shell[2]. Consequently, the material derivative becomes

$$\frac{D}{Dt} = \partial_t + \frac{r_0\cos\varphi_0}{r\cos\varphi}u\partial_x + \frac{r_0}{r}v\partial_y + w\partial_z \approx \partial_t + u\partial_x + v\partial_y + w\partial_z$$

and all other differential operators look again like their Cartesian analogs. The Coriolis terms are expanded in the same way[3],

$$\begin{aligned}
f &= 2\Omega\left(\varphi + \mathcal{O}(\varphi^3)\right) = y\beta + \mathcal{O}(y^3), \\
\tilde{f} &= 2\Omega\left(1 + \mathcal{O}(\varphi^2)\right) = \tilde{f}_0 + \mathcal{O}(y^2),
\end{aligned}$$

where the common parameters $\beta = \frac{2\Omega}{r_0}$ and $\tilde{f}_0 = 2\Omega$ are used for the first time. This is also the reason for the name $\beta-plane\ approximation$. Dropping forcing and friction for the moment, the same steps

---

[2]This is called the *thin shell approximation*. The relative accuracy of these steps is still about 98% in a region of $\pm 10^0$ latitude around the Equator and a depth up to $10\,\text{km}$.

[3]Note that the expansions look different for $\varphi_0 \neq 0$. Additional parameters f_0 and $\tilde{\beta}$ are needed, and the other parameters change as well.

are applied to the system (2.3.2a)-(2.3.2e), yielding:

$$\frac{Du}{Dt} - vy\left(\frac{u}{r_0^2} + \beta\right) + w\left(\frac{uw}{r_0} + \tilde{f}_0\right) = -\frac{1}{\varrho_*}\partial_x \tilde{p} \tag{2.4.2a}$$

$$\frac{Dv}{Dt} + \frac{wv}{r_0} + uy\left(\frac{u}{r_0^2} + \beta\right) = -\frac{1}{\varrho_*}\partial_y \tilde{p} \tag{2.4.2b}$$

$$\frac{Dw}{Dt} - \frac{u^2 + v^2}{r_0} - \tilde{f}u = -\frac{1}{\varrho_*}\partial_z \tilde{p} - b \tag{2.4.2c}$$

$$-wN^2 + \frac{Db}{Dt} = 0 \tag{2.4.2d}$$

$$\partial_x u + \partial_y v + \partial_z w = 0 \tag{2.4.2e}$$

Additionally, the so-called Brunt–Väisälä frequency or *buoyancy frequency*

$$N^2 = -\frac{g}{\varrho_*}\partial_z \varrho_0 \tag{2.4.3}$$

has been introduced, a quantity originally arising from the concept of local static stability. A fluid parcel oscillates with this frequency around its original position after a slight displacement. Hence, $N^2 > 0$ in a stable stratified fluid column, and instability arises if $N \in \mathbb{C}$. Its importance arises from the fact that it can be directly measured in some cases, and there are extended definitions including sound waves, see Gerkema et al. (2008).

2.5 Linearization for small amplitude motions

All considerations in the following are focused on waves, which are supposed to be small disturbances from a ground state. This makes it possible to linearize the system (2.4.2a)-(2.4.2e) around this state by writing

$$\vec{u} = \vec{u}_0 + \vec{u}', \qquad \text{where} \qquad \vec{u}' \ll \vec{u}_0.$$

The choice of a ground state always needs careful justification. Despite the fact that there are strong zonal currents at the Equator in reality, the choice $\vec{u}_0 \equiv 0$ is made in the following. For any other state, it is not clear at this stage whether it exists *besides* the waves or *because of* the waves. This also allows for immediately writing $\vec{u}$ instead of $\vec{u}'$, just omitting all products of $\vec{u}$ and its derivatives. However, with this notation, one has to keep in mind that cross-terms of $\vec{u}_0$ and $\vec{u}'$ will enter the equations when considering other ground states, changing them significantly. The resulting equations are:

$$u_t - \beta y v + \tilde{f}_0 w = -\frac{1}{\varrho_*}\tilde{p}_x \tag{2.5.1a}$$

$$v_t + \beta y u = -\frac{1}{\varrho_*}\tilde{p}_y \tag{2.5.1b}$$

$$w_t - \tilde{f}_0 u = -\frac{1}{\varrho_*}\tilde{p}_z - b \tag{2.5.1c}$$

$$-wN^2 + \partial_t b = 0 \tag{2.5.1d}$$

$$u_x + v_y + w_z = 0 \tag{2.5.1e}$$

This system is much simpler to treat than eq. (2.4.2a)-(2.4.2e), but one always has to be careful: the linear waves might amplify locally, and then the hypothesis of small amplitudes is not justified anymore.
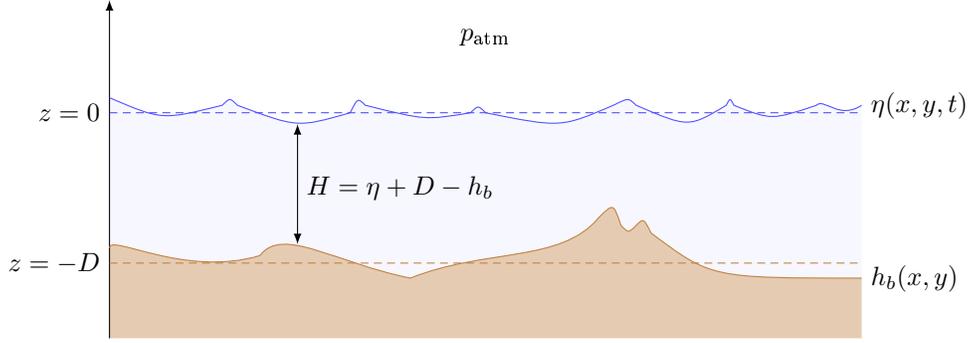
Figure 2.2: Denomination of the limiting surfaces.

2.6   Boundary conditions

Boundary conditions are fundamental ingredients of all problems in fluid dynamics, as they strongly influence the nature of solutions or even the solvability. Only the basic vertical boundary conditions and their most common simplifications are described here, whereas all other boundary conditions will be introduced for each specific problem.

As depicted in figure 2.2, the sea surface amplitude $\eta(x, y, t)$ and the static bottom topography $h_b(x, y)$ are defined in a way that the whole layer depth is

$$H = \eta(x, y, t) + D - h_b(x, y).$$

The hydrostatic pressure follows from equation (2.1.2), which however determines it only up to a constant. Demanding it to be equal to the atmospheric pressure p_{atm} at $z = 0$, it becomes

$$p_0(z) = -g \left(\varrho_* z + \int_0^z \varrho_0(\zeta) \, d\zeta \right) + p_{\mathrm{atm}}. \tag{2.6.1}$$

With this definition, pressure changes due to the variable sea surface η, for instance, are described conveniently by the *perturbation pressure*

$$\tilde{p} = p - p_0.$$

This redefinition has to be kept in mind, but it is advantageous as one is dealing with perturbative quantities only.

If friction is neglected, the only boundary conditions that can be satisfied at the top and the bottom are

$$p|_{z=\eta} = p_{\mathrm{atm}}, \qquad \left. \frac{D\left(z - \eta(x, y, t)\right)}{Dt} \right|_{z=\eta} = 0 \quad \text{and} \quad \left. \frac{D\left(z + D - h_b(x, y)\right)}{Dt} \right|_{z=-D+h_b} = 0. \tag{2.6.2}$$

The first condition is a *dynamic* boundary condition, whereas the latter two relations are *kinematic* boundary conditions. As there may still be velocity components parallel to the boundaries, this case is also called *free-slip*. On the contrary, the order of the momentum equation is raised by one if friction and external forcing are taken into account. Then, the *no-slip* condition can be imposed at the bottom, reading

$$\vec{u}|_{z=-D+h_b} = 0,$$

and external forcing terms like wind stress can be included at the sea surface. An excessive treatment of various boundary conditions, including those for T and S that are not discussed here, can be found in Dijkstra (2008).

Linearized boundary conditions. For wave-like perturbations, the boundary conditions can be linearized like it has been done for the other equations in the previous section. To this end, the perturbation pressure and the vertical velocity are expanded in a Taylor series:

$$\tilde{p}(x,y,\eta) = \tilde{p}(x,y,0) + \eta\tilde{p}_z(x,y,0) + \mathcal{O}(\eta^2) \quad \approx \tilde{p}(x,y,0)$$
$$w(x,y,\eta) = w(x,y,0) + \eta w_z(x,y,0) + \mathcal{O}(\eta^2) \quad \approx w(x,y,0)$$

Neglecting all terms that contain products of perturbations in eq. (2.6.2), the kinematic and dynamic boundary conditions at the surface read then

$$\tilde{p}|_{z=0} = \varrho_* g\eta \qquad \text{and} \qquad w|_{z=0} = \eta_t. \tag{2.6.3}$$

Hence, the boundary conditions can be applied just at $z = 0$!

Rigid lid approximation. *Internal waves* are waves that reach their maximal amplitude in the interior of a fluid, and not at the surface. The so-called rigid lid approximation is used in this case: combining the constraints in eq. (2.6.3) into a single equation, one finds that $\tilde{p}_t|_{z=0} = \varrho_* g\, w|_{z=0}$. It can be derived from scaling arguments very similar to those that will be presented in section 2.7 that

$$w|_{z=0} \approx 0 \tag{2.6.4}$$

is a reasonable assumption for internal waves, so the surface can be considered to be flat and vertically fixed. As pointed out for example in Gerkema et al. (2008), the deeper reasoning for this approach lies in the different speed scales for surface waves ($\sim \sqrt{Dg}$) and internal waves ($\sim \sqrt{Dg'}$). It is important to note that this approximation usually does not mean that the pressure perturbation has to be zero on the surface, but rather that the surface is covered by a rigid plate that absorbs the pressure variations else leading to surface elevations.

2.7 Scale analysis

Scale analysis is a powerful tool used in all areas of fluid mechanics throughout, as it enables to elucidate the dominant balances of a system under certain assumptions. Characteristic scales L, D, U, W and P are introduced by replacing all dimensional quantities to a corresponding dimensionless quantity of $\mathcal{O}(1)$ (these dimensionless quantities will be tagged with a hat in the following):

$$x = L\hat{x} \qquad\qquad y = L\hat{y} \qquad\qquad z = D\hat{z} \qquad\qquad t = \frac{L}{U}\hat{t} \tag{2.7.1}$$
$$u = U\hat{u} \qquad\qquad v = U\hat{v} \qquad\qquad w = W\hat{w} \qquad\qquad \tilde{p} = P\hat{p}$$

As the momentum equations are linear in t, the *advective time scale* $T = L/U$ can be chosen without loss of generality. Note that $\hat{p}$ represents the dimensionless *dynamical* pressure. To simplify the notation, three dimensionless parameters are widely used, namely

$$\text{Ro} = \frac{U}{2\Omega L}, \qquad\qquad \delta = \frac{D}{L}, \qquad\qquad l = \frac{L}{r_0}. \tag{2.7.2}$$

The dimensionless Rossby number Ro describes the ratio between inertial acceleration and Coriolis acceleration, δ is called the aspect ratio (for almost all problems $\delta \ll 1$) and l is called the metric ratio (which is not necessarily small). Inserting those scales in the continuity equation, one finds

$$\frac{U}{L}\hat{u}_{\hat{x}} + \frac{U}{L}\hat{v}_{\hat{y}} + \frac{W}{D}\hat{w}_{\hat{z}} = 0. \tag{2.7.3}$$

Hence, by fixing $W = U \cdot D / L = \delta U$, the equation takes the same form as its dimensional counterpart,

$$\hat{u}_{\hat{x}} + \hat{v}_{\hat{y}} + \hat{w}_{\hat{z}} = 0.$$

In the following, the buoyancy terms are omitted since they are not necessary to point out the main features. The dimensionless version of the momentum equations (2.5.1a)-(2.5.1c) turns out to be:

$$\hat{u}_{\hat{t}} - \frac{1}{\text{Ro}} \left(l \hat{y} \hat{v} - \delta \hat{w} \right) = -\frac{P}{U^2 \varrho_*} \hat{p}_{\hat{x}} \tag{2.7.4a}$$

$$\hat{v}_{\hat{t}} + \frac{l}{\text{Ro}} \hat{y} \hat{u} = -\frac{P}{U^2 \varrho_*} \hat{p}_{\hat{y}} \tag{2.7.4b}$$

$$\delta^2 \hat{w}_{\hat{t}} - \frac{\delta}{\text{Ro}} \hat{u} = -\frac{P}{U^2 \varrho_*} \hat{p}_{\hat{z}} \tag{2.7.4c}$$

From these equations, different cases of interest will be inspected on their corresponding scales in the following.

Speed of sound c_s of seawater (Gill, 1982)	$(1.5 \pm 0.7) \cdot 10^3 \, \frac{\text{m}}{\text{s}}$
Vertical Coriolis frequency $\tilde{f}_0$ at the Equator	$1.46 \cdot 10^{-4} \frac{1}{\text{s}}$
Parameter β at the Equator	$2.17 \cdot 10^{-11} \frac{1}{\text{m s}}$
Mean ocean depth $\overline{H}$	$4 \, \text{km}$
Horizontal velocities at the Equator (Dijkstra, 2008)	$\lesssim 1 \, \frac{\text{m}}{\text{s}}$
Vertical upwelling velocity at the Equator (Dijkstra, 2008)	$\lesssim 2.3 \cdot 10^{-5} \, \frac{\text{m}}{\text{s}} = 2 \, \frac{\text{m}}{\text{d}}$
Buoyancy frequency N^2 away from the thermocline	$\approx 10^{-5} - 10^{-4} \frac{1}{\text{s}^2}$

Table 2.1: Typical values of some representative quantities.

2.7.1 Shallow water equations

This very famous set of equations is obtained in case of a small aspect ratio, $\delta \ll 1$. If we assume additionally $\delta \ll \text{Ro}$ and $\delta \ll l$, the terms of order δ can be dropped in the system (2.7.4a)-(2.7.4c), and thus the dimensional equations

$$u_t - \beta y v = -\frac{1}{\varrho_*} \tilde{p}_x \tag{2.7.5a}$$

$$v_t + \beta y u = -\frac{1}{\varrho_*} \tilde{p}_y \tag{2.7.5b}$$

$$0 = -\frac{1}{\varrho_*} \tilde{p}_z \tag{2.7.5c}$$

$$u_x + v_y + w_z = 0 \tag{2.7.5d}$$

are inferred.

Now, there are two ways to proceed. The first one is to assume that the horizontal velocities u and v do not depend on z as the pressure terms do neither, or in other words, vertical shear is excluded. This assumption would lead to the shallow water equations even if the nonlinear terms were still present, but it might appear less natural in this case. Then, the continuity equation can be integrated over depth easily, yielding

$$\int_{h_b - D}^{\eta} (u_x + v_y + w_z) \, dz = (Hu)_x + (Hv)_y + \eta_t = 0,$$

where the kinematic boundary conditions in eq. (2.6.2) have been used. Using eq. (2.6.1) and the pressure condition in eq. (2.6.2), one finds $\tilde{p} = p - p_0 = g\left(\varrho_*\eta + \int_0^\eta \varrho_0(z)\,d\tilde{z}\right) \approx g\varrho_*\eta$ as $\varrho_0 \ll \varrho_*$. Altogether, the standard form of the shallow-water equations in the equatorial $\beta-$plane reads then:

$$u_t - \beta y v = -g\eta_x \tag{2.7.6a}$$

$$v_t + \beta y u = -g\eta_y \tag{2.7.6b}$$

$$(Hu)_x + (Hv)_y + \eta_t = 0 \tag{2.7.6c}$$

A lower limit for the horizontal length scale L follows from the condition $\delta \ll l$, which also can be stated as

$$L \gg \sqrt{Dr_0} \approx 160\,\mathrm{km}, \tag{2.7.7}$$

corresponds to about $2°$ of latitude around the Equator. Only on length scales satisfying this condition, the shallow-water approximation is expected to work well, premising the validity of all other conditions (for D, the value $\overline{H}$ from table 2.1 was used).

Depth-integrated equations. Instead of *assuming* that the velocities are independent of z, one can just depth-integrate the momentum equations and obtain *exact* results. This is however only possible in the linearized case, as then there are no nonlinear terms in $\vec{u}$. The depth-integrated quantities are defined as

$$\overline{f}(x,y) = \int\limits_{h_b - D}^{\eta} f(x,y,z)\,dz,$$

and derivatives under the integral are handled by means of the relation

$$\partial_x \left[\int\limits_{b(x)}^{a(x)} f(x,\cdots,z)\,dz\right] = \int\limits_b^a f_x\,dz + f\,a_x|_{z=a} - f\,b_x|_{z=b}. \tag{2.7.8}$$

The resulting set of equations is very similar to eq. (2.7.6a)-(2.7.6c):

$$\overline{u}_t - \beta y\overline{v} = -gH\eta_x \tag{2.7.9a}$$

$$\overline{v}_t + \beta y\overline{u} = -gH\eta_y \tag{2.7.9b}$$

$$\overline{u}_x + \overline{v}_y + \eta_t = 0 \tag{2.7.9c}$$

Upon dropping all terms quadratic in the perturbations in both systems, i.e. replacing $H = \eta + D - h_b$ by $D = \mathrm{const.}$, they give identical results.

Essentially, the second derivation may allow for interpretation in terms of a completely depth-integrated setting, if results are obtained from the linearized shallow water equations.

2.7.2 Geostrophic balance

If, in addition to the conditions for a shallow-water approximation, the Rossby number satisfies $\mathrm{Ro} \ll 1$, then the Coriolis force balances the pressure gradient in first instance. As the material derivative is dropped, a time-independent solution results. The appropriate pressure scale is now $P = \frac{U^2\varrho_*}{\mathrm{Ro}}$. Dropping again terms of order δ in the system (2.7.4a)-(2.7.4c), one may expand all variables in a formal power series of Ro, that is

$$\hat{u} = \hat{u}^{(0)} + \mathrm{Ro}\,\hat{u}^{(1)} + \cdots, \qquad \hat{p} = \hat{p}^{(0)} + \mathrm{Ro}\,\hat{p}^{(1)} + \cdots,$$

$\hat{v}$ and $\hat{w}$ similar. In this way the famous geostrophic equations are derived, reading

$$l\hat{y}\hat{v}^{(0)} = \hat{p}_{\hat{x}}^{(0)} \qquad\qquad\qquad \hat{u}_{\hat{x}}^{(0)} + \hat{v}_{\hat{y}}^{(0)} = 0 \qquad\qquad (2.7.10\text{a})$$

$$-l\hat{y}\hat{u}^{(0)} = \hat{p}_{\hat{y}}^{(0)} \qquad\qquad\qquad \hat{u}_{\hat{z}}^{(0)} = \hat{v}_{\hat{z}}^{(0)} = 0 \qquad\qquad (2.7.10\text{b})$$

$$0 = \hat{p}_{\hat{z}}^{(0)} \qquad\qquad\qquad\qquad \hat{w} \equiv 0 \qquad\qquad (2.7.10\text{c})$$

The equations in the right column are derived using the equations in the left column, the continuity equation and the (simplified) boundary condition $\hat{w}^{(0)} = 0$ at the bottom.

A quick check of the condition $\mathrm{Ro} \ll 1$ yields

$$U \ll 2\Omega L \gg 23\,\frac{\mathrm{m}}{\mathrm{s}},$$

where the relation (2.7.7) was used for the latter estimation. As typical horizontal velocities observed in the ocean are at most of $\mathcal{O}(1\,\frac{\mathrm{m}}{\mathrm{s}}) < 23\,\frac{\mathrm{m}}{\mathrm{s}}$, the geostrophic balance is expected to work well on the corresponding length scales. The importance of these equations comes from the fact that many of the large scale ocean currents, like the Gulf stream or the Kuroshio, are (almost) in geostrophic balance.

2.7.3   Non-rotating approximation

The case $\mathrm{Ro} \gg 1$ is briefly discussed for the sake of completeness, where the time derivatives balance the pressure gradient and the influence of the Coriolis terms is small. Now, $P = U^2 \varrho_*$ is the proper pressure scale, as then an expansion similar to the one done in the preceding section is possible. The crucial difference is that $\frac{1}{\mathrm{Ro}} \ll 1$ has to be used as an expansion parameter.

This yields just the well-known momentum equations of a non-rotating fluid, basically eq. (1.2.1a). But note that the term proportional to δ^2 cannot be dropped anymore, as it is not necessarily small: estimating for example $U \approx 1\,\frac{\mathrm{m}}{\mathrm{s}}$, the condition $\mathrm{Ro} \gg 1$ means that

$$L \ll \frac{U}{2\Omega} \approx 1.4\,\mathrm{km}.$$

Thus, at small length scales, the influence of the Coriolis force can be neglected in first instance. An example for wave phenomena at these scales are capillary-gravity waves, and one may conclude that they are not significantly modified by the Earth's rotation.

As one is usually interested in larger length scales in equatorial oceanography, the non-rotating case is of minor interest and is therefore not tackled in this work.

2.7.4   Non-traditional approach

In the precedent considerations, only the radial part (i.e. the projection of $\vec{\Omega}$ on $\hat{e}_r$) of the Earth's rotation was taken into account for the Coriolis terms. The other terms were neglected by assuming $\delta \ll l$ in the system (2.7.4a)-(2.7.4c). This is usually called the *traditional approximation*, and the idea goes back to Laplace, see Gerkema et al. (2008) for a comprehensive review of the topic.

Exactly at the Equator however, the radial part of $\vec{\Omega}$ vanishes! The scale on which in this region the tangential component of $\vec{\Omega}$ and the radial component are equally strong can be determined by setting the ratio between the corresponding factors equal to one,

$$\frac{l}{\delta} = \frac{L^2}{r_0 D} = 1, \qquad \Rightarrow \qquad L = \sqrt{D r_0} \approx 160\,\mathrm{km}.$$

The approach that takes into account the full Coriolis force is called the *non-traditional approach*. It was used less often in the past as the name already suggests, also because a *zonal* length scale of $160\,\mathrm{km}$ seems to be too small to be relevant at the Equator.

Clearly, the equatorial region cannot be identified with a square constituted by one horizontal length scale L, since it looks more like a belt. Hence, it is very natural to introduce horizontally anisotropic length scales, as it will be done at a later stage in section 7.1. It will then turn out that the standard textbook method presented here overestimates the impact of the traditional terms, which is a clear sign for the importance of the non-traditional terms at the Equator.

Chapter 3

Classical equatorial wave theory

This chapter is dedicated to recapitulate some topics of the existing, well-established theory on equatorial waves. This approach goes mainly back to Matsuno (1966), using the shallow-water equations. Buoyancy is absent meaning $N \equiv 0$, and so are the nontraditional components of the Coriolis force. The waves described in this model can be thought of as surface waves like in section 3.1 or as interface waves at a density step like in the following sections, then being internal waves.

The unforced wave solutions presented here eventually allow to treat forced systems in the low frequency limit using the method of Green's functions. This method will not be described in detail here, as it can be found in many recent textbooks, like Dijkstra (2008). Based on it, adjustment processes on time-dependent changes in the forcing (like the surface wind stress) can be modeled. Furthermore, this theory gains its importance by providing a crucial part in recent theories of El Niño, which is however a coupled ocean-atmosphere phenomenon and also goes beyond the scope of this work - a comprehensive review on this topic can be found in Dijkstra and Burgers (2002).

3.1 Equatorial Kelvin waves

Classical *Kelvin waves* arise from a balance between Coriolis force and a topographic boundary. They are named after Lord Kelvin, who proposed them for the first time in Thomson (1879).

In an *equatorial Kelvin wave* however the Coriolis force balances itself. This is possible due to the sign change in the traditional terms of the Coriolis force: on both hemispheres, objects traveling eastwards are deflected towards the Equator, and in this way a *stationary* balance between pressure gradient and Coriolis force can be established in the meridional direction. Hence, these waves are characterized by a vanishing meridional velocity,

$$v \equiv 0.$$

In order to maintain this balance, Kelvin waves will always travel eastwards.

In the simplified approach retained in this chapter, the equatorial ocean is considered as a thin layer with $D \ll L$. Then the shallow water equations (2.7.6a)-(2.7.6c) can be used. Moreover, the variations of w with time are neglected and the initial system reads:

$$u_t = -g\eta_x \tag{3.1.1a}$$
$$\beta y u = -g\eta_y \tag{3.1.1b}$$
$$Du_x + \eta_t = 0 \tag{3.1.1c}$$

In the last line, a term $(\eta u)_x$ is neglected as it is quadratic in the perturbations. Combining eq. (3.1.1a) and eq. (3.1.1c), two wave equations are found,

$$u_{tt} - c^2 u_{xx} = 0 \qquad \text{and} \qquad \eta_{tt} - c^2 \eta_{xx} = 0, \qquad \text{where} \qquad c^2 = Dg.$$
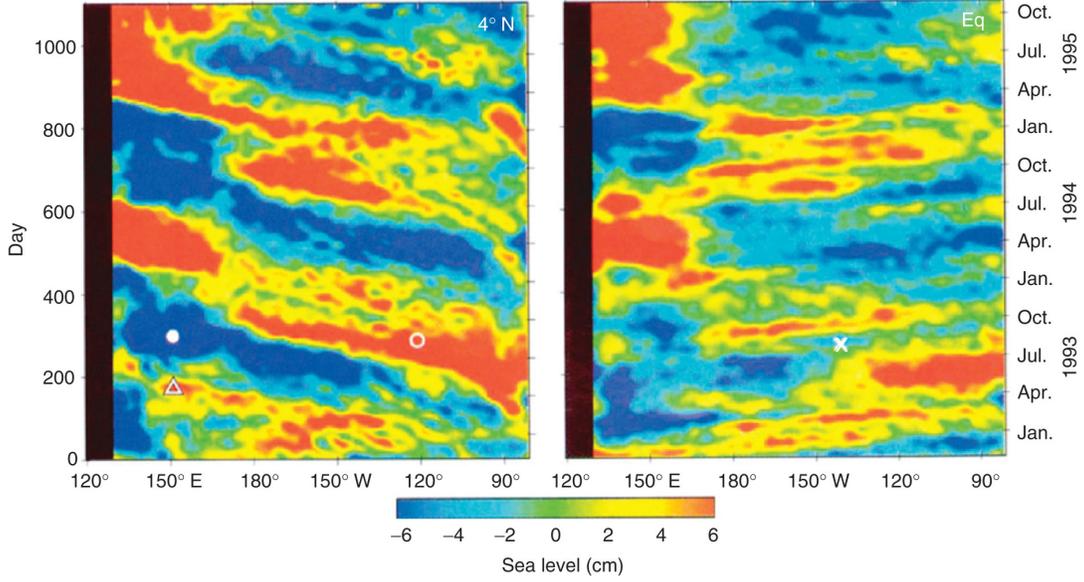
Figure 3.1: Sea level anomalies from TOPEX/POSEIDON data at two different latitudes. The disturbances at 4º N shown in the left picture are moving westwards in time, they might consist of Rossby waves described in section 3.3. The disturbances right at the Equator shown in the left picture move eastwards and are commonly interpreted as equatorial Kelvin waves (picture from Chelton and Schlax, 1996).

Eliminating η between eq. (3.1.1a) and eq. (3.1.1b) and inserting an ansatz $u \propto e^{i(kx-\omega t)} f(y)$ in the resulting equation yields an equation governing the meridional dependency. This equation can be easily integrated,

$$\partial_y (\ln f) = -\frac{k\beta}{\omega} y = -\frac{\beta}{c_{\mathrm{ph}}} y, \qquad \text{such that} \qquad f = e^{-\frac{\beta}{2c_{\mathrm{ph}}} y^2}.$$

As mentioned before, the (zonal) phase velocity of the wave has thus to be positive in order to avoid unbounded solutions that are exponentially increasing for large $|y|$,

$$c_{\mathrm{ph}} \equiv \frac{\omega}{k} = +\sqrt{Dg} \qquad \text{and} \qquad c_{\mathrm{gr}} \equiv \frac{\partial \omega}{\partial k} = c_{\mathrm{ph}}.$$

The positive sign is crucial as it indicates that these waves can only travel eastwards, like the disturbances shown in the right-hand side of figure 3.1.

For the physical fields, only the real part of the functions is considered, and the whole set of solutions reads:

$$u_k = U \cos\left(k(x - \sqrt{Dg} \cdot t) + \phi\right) e^{-\frac{\beta}{\sqrt{Dg}} y^2} \tag{3.1.2}$$

$$w_k = -Uk(z + D) \sin\left(k(x - \sqrt{Dg} \cdot t) + \phi\right) e^{-\frac{\beta}{\sqrt{Dg}} y^2} \tag{3.1.3}$$

$$\eta_k = -\sqrt{\frac{D}{g}} u \tag{3.1.4}$$

Note that there is a phase shift of $\frac{\pi}{2}$ between u and w. The vertical velocity w is obtained from the continuity equation. It again satisfies the linearized boundary conditions

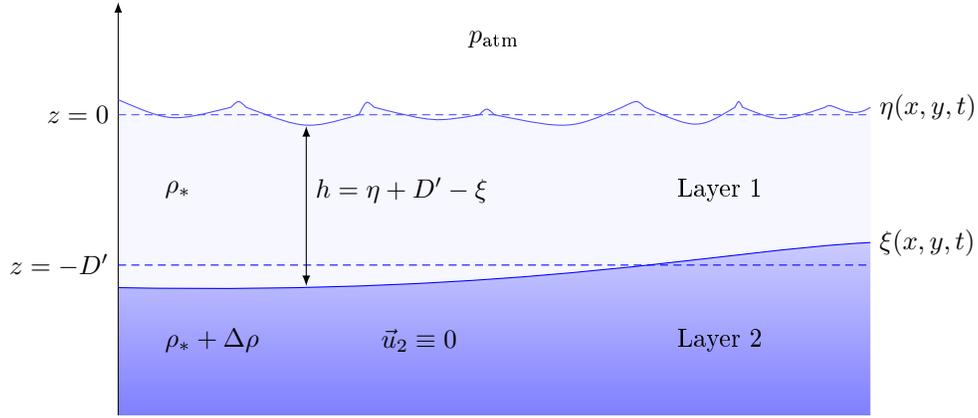$$w|_{z=0} = \eta_t \quad \text{and} \quad w|_{z=-D} = 0.$$

Figure 3.2: Denomination of surfaces and general setting in the reduced gravity model, ξ is the deviation of the thermocline/interface from its mean value $-D'$. Layer 2 is regarded to be motionless and infinitely deep.

Remarkably, there exists a stationary flow for $k = 0$, reading

$$u_0 = U e^{-\frac{\beta}{\sqrt{Dg}} y^2}, \qquad w_0 = 0 \quad \text{and} \quad \eta_0 = -\sqrt{\frac{D}{g}} U e^{-\frac{\beta}{\sqrt{Dg}} y^2}.$$

This flow can however only exist in a zonally unbounded or periodically bounded domain, like a gas planet. In the real ocean, there are zonal boundaries and for a basin of zonal length L, boundary conditions may be formulated as

$$u|_{x=x_0} = u|_{x=x_0+L} = 0.$$

This lastly leads to a quantization of the zonal wave number, $k = \frac{\pi}{L} n$ with $n \in \mathbb{Z}/\{0\}$ and fixes the phase ϕ. The particular solution is then obtained by superposition of the general solution,

$$u = \sum_k a_k u_k, \qquad \cdots$$

where the amplitudes a_k can be determined for instance from initial conditions.

With $D = \mathcal{O}(10^3 \, \text{m})$, a typical velocity for an equatorial Kelvin wave traveling at the surface is $c = \mathcal{O}(10^2 \, \frac{\text{m}}{\text{s}})$, which is very high and much faster than expected. The scale on which it decays in the meridional direction is called the equatorial Rossby deformation radius $L_R = \sqrt{\frac{c}{\beta}}$, and a typical value for the surface wave is $L_R = \mathcal{O}(10^3 \, \text{km})$! This is quite large for an equatorial phenomenon and may violate the assumptions made in order to use the β–plane.

One possible way out of this dilemma is provided by inspecting waves traveling at the thermocline, like it is done in the following.

3.2 Reduced gravity model

Layer models allow to conveniently include phenomena occurring in the interior of the sea, especially in numerical models, where the number of layers can be increased easily. The reduced gravity model or $1\frac{1}{2}$ layer model is a simple way to describe internal wave propagation along the equatorial thermocline (see section 1.1) analytically, but one should be aware that it gives a rather coarse model of reality.

For this purpose, consider two layers of water with different densities separated by a material surface modeling the thermocline, as depicted in figure 3.2.

Now, the neutral position of this interface is at $-D'$, and its dynamical position is described by the field $\xi(x, y, t)$. Hence, the thickness h of the upper Layer 1 is $h = \eta + D' - \xi$ (typical values for D' are several $100\,\mathrm{m}$, and several $10\,\mathrm{m}$ for ξ). This layer has density ϱ_*, and it is governed by the original equations. Here, the quantities in this layer shall wear *no index*. A higher density $\varrho_* + \Delta\varrho$ is assumed in the lower Layer 2 which is furthermore supposed to be motionless and infinitely deep. Then, the hydrostatic equation

$$\partial_z p_2 = -(\varrho_* + \Delta\varrho)g \tag{3.2.1}$$

applies for the pressure p_2. At the interface, there are two new boundary conditions, namely

$$p|_{z=-D'+\xi} = p_2|_{z=-D'+\xi} \qquad \text{and} \qquad \left.\frac{D\,(z + D' - \xi)}{Dt}\right|_{z=-D'+\xi} = 0.$$

Note that in the first boundary condition the actual pressure appears, i.e. $p = p_0 + \tilde{p}$, as the hydrostatic background pressure is different for each layer.

First, a crucial relation between the sea surface elevation and the thermocline elevation can be established. Evaluating the dynamic boundary condition, it is found that

$$p_2 = -g(\varrho_* + \Delta\varrho)(z + D' - \xi) + \varrho_* gh + p_{\mathrm{atm}}. \tag{3.2.2}$$

But from eq. (3.2.1) it becomes clear that the horizontal gradient $\nabla_H \equiv (\partial_x, \partial_y)^T$ of p_2 vanishes. Computing ∇_H of eq. (3.2.2) then yields

$$\nabla_H \xi = -\frac{\varrho_*}{\Delta\varrho}\nabla_H \eta. \tag{3.2.3}$$

This insight is very important, as it states that *small changes in sea surface are related to big changes in the thermocline elevation.* In practice, the sea surface elevation is obtained for example from satellite data like already depicted in figure 3.1, and eq. (3.2.3) then allows an interpretation in terms of thermocline changes.

Similar to what was done in the derivation of the shallow water equations, the continuity equation can be integrated vertically in the upper Layer 1 from $z = -D' + \xi$ to $z = \eta$ by means of the relation (2.7.8). The outcome of this procedure is a set of equations that looks like the shallow-water set, except for the substitutions

$$g\nabla\eta \longrightarrow g'\nabla h \qquad \text{and} \qquad D \longrightarrow D', \qquad \text{where} \qquad g' = \frac{\Delta\varrho}{\varrho_*}g.$$

This means that the factor g' called the *reduced gravity* appears in the equations instead of g, and the layer thickness h replaces η. A comprehensive derivation of these latter relations can be found for example in Dijkstra (2008).

Hence, all results obtained in the preceding section should remain valid but the numerical values change as now $c = \sqrt{D'g'}$. As mentioned in section 2.1, typical relative density differences in the ocean are of $\mathcal{O}(10^{-3})$. Taking a realistic upper layer depth of $D' = \mathcal{O}(10^2\,\mathrm{m})$, a typical velocity for an equatorial Kelvin wave traveling at the thermocline is therefore $c = \mathcal{O}(1\,\frac{\mathrm{m}}{\mathrm{s}})$. This value is considerably lower and agrees with the speeds obtained from observations like the ones shown in figure 3.1. It also yields a more realistic Rossby deformation radius $L_R \approx \mathcal{O}(10^2\,\mathrm{km})$.

3.3 Waves with nonzero meridional velocity

In the shallow water approach used in this chapter, a whole bunch of waves with nonzero meridional velocity appears, too. They result from the following set of equations:

$$
\begin{align}
u_t - \beta y v &= -g'h_x \tag{3.3.1a}\\
\epsilon v_t + \beta y u &= -g'h_y \tag{3.3.1b}\\
D'(u_x + v_y) + h_t &= 0, \tag{3.3.1c}
\end{align}
$$

Here, the dimensionless number ϵ was implemented. It can be derived from scaling arguments similar to those presented in section 2.7, that neglecting the term v_t corresponds to taking the limit in which the zonal length scale L is much bigger than the equatorial Rossby deformation radius $L_R = \sqrt{\frac{c}{\beta}}$ (see, for example, Dijkstra, 2008). Thus, $\epsilon = 1$ is assumed for the complete analysis of the system, but later on the so-called *long wave limit* can be achieved easily by setting $\epsilon = 0$ in all resulting equations.

To tackle the full system, a single equation for v can be derived as follows: firstly, an equation describing the time evolution of the vertical component of the vorticity $\nabla \times \vec{u}$ is derived by cross-differentiating eq. (3.3.1a) and eq. (3.3.1b), stating

$$\partial_t \left(\epsilon v_x - u_y - \frac{\beta}{D'} y h \right) + \beta v = 0. \tag{3.3.2}$$

The variables u and h can then be eliminated by computing $(3.3.1b)_{tt} - g \cdot (3.3.1c)_{ty} - \beta y \cdot (3.3.1a)_t - D'g' \cdot (3.3.2)_x$. The demanded relation reads

$$\partial_t \left(\epsilon v_{tt} - c^2 (\epsilon v_{xx} + v_{yy}) + (\beta y)^2 v \right) - c^2 \beta v_x = 0. \tag{3.3.3}$$

Here, $c = \sqrt{D'g'}$ is understood. Looking for plane-wave solutions of the form $v = V(y) e^{i(kx - \omega t)}$, a differential equation that determines the meridional structure is found,

$$\frac{d^2}{dy^2} V + \left(\epsilon \left(\frac{\omega}{c} \right)^2 - \epsilon k^2 - \frac{k\beta}{\omega} \right) V - \left(\frac{\beta}{c} \right)^2 y^2 V = 0. \tag{3.3.4}$$

Introducing dimensionless quantities for convenience according to

$$\hat{y} = \sqrt{\frac{\beta}{c}} y \qquad\qquad \hat{\omega} = \frac{\omega}{\sqrt{\beta c}} \qquad\qquad \hat{k} = \sqrt{\frac{c}{\beta}} k$$

and choosing an ansatz $V(\hat{y}) = e^{-\hat{y}^2/2} \mathcal{H}(\hat{y})$, eq. (3.3.4) eventually transforms into *Hermite's eigenvalue problem*

$$\mathcal{H}_n'' - 2\hat{y}\mathcal{H}_n' + 2n\mathcal{H}_n = 0, \qquad 2n + 1 = \epsilon\hat{\omega}^2 - \epsilon\hat{k}^2 - \frac{\hat{k}}{\hat{\omega}}. \tag{3.3.5}$$

For integer eigenvalues $n \in \mathbb{N}_0$, the Hermite polynomials $\mathcal{H}_n = (-1)^n e^{\hat{y}^2} (d/d\hat{y})^n e^{-\hat{y}^2}$ that are well-known from quantum mechanics constitute appropriate solutions which remain bounded as $\hat{y} \to \pm\infty$. The meridional structure is then covered by *parabolic cylinder functions*, $V_n = e^{-\hat{y}^2/2} \mathcal{H}_n$.

The other fields can then be obtained by eliminating one variable from eq. (3.3.1a)-(3.3.1c), respectively. Using the relation $\mathcal{H}_n' = 2n\mathcal{H}_{n-1}$, the whole solution reads

$$v_{n,k} = (-1)^n e^{i(kx-\omega t)} e^{\hat{y}^2/2} \frac{d^n}{d\hat{y}^n} e^{-\hat{y}^2} = e^{i(kx-\omega t)} V_n(y) \tag{3.3.6a}$$

$$u_{n,k} = i \frac{2n\hat{k}V_{n-1} - \hat{\omega}\hat{y}V_n}{\hat{k}^2 - \hat{\omega}^2} e^{i(kx-\omega t)} \tag{3.3.6b}$$

$$h_{n,k} = i \frac{H}{c} \frac{2n\hat{\omega}V_{n-1} - \hat{k}\hat{y}V_n}{\hat{k}^2 - \hat{\omega}^2} e^{i(kx-\omega t)}. \tag{3.3.6c}$$

Note that here $\hat{\omega} = \hat{\omega}(n, \hat{k})$ is understood. The first meridional structure functions are depicted in figure 3.3. As one can see from this picture, the waves are confined to a region of a few L_R next to the Equator. Therefore, these waves are also called *equatorially trapped*.
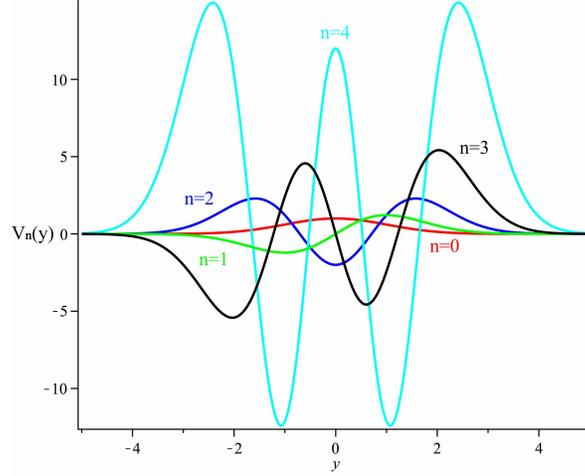
Figure 3.3: The first five meridional structure functions $V = e^{-\hat{y}^2/2}\mathcal{H}_n$. For odd n, the functions are indeed odd and their extrema *all* lie off the Equator. Likewise, the functions are even for even n.

Classification of solutions. In order to see all different types of waves in this model, $\epsilon = 1$ is taken in the following. The dispersion relation is obtained from the definition (3.3.5) of the eigenvalue n, which is most easily regarded as a quadratic equation for $\hat{k}(\hat{\omega})$:

$$\hat{k}^2 + \frac{\hat{k}}{\hat{\omega}} + (2n + 1 - \hat{\omega}^2) = 0, \qquad \hat{k}_{1/2} = -\frac{1}{2\hat{\omega}} \pm \frac{1}{2}\sqrt{\left(\frac{1}{\hat{\omega}} - 2\hat{\omega}\right)^2 - 8n} \tag{3.3.7}$$

Three different types of waves appear to be contained in this dispersion relation that is discussed in the following. An overview is depicted in figure 3.4.

For a given $n > 0$, two real roots are provided if the determinant is positive, which is the case if

$$\hat{\omega} < \sqrt{\frac{1}{2} + n - \sqrt{n(n+1)}} \qquad \text{or} \qquad \hat{\omega} > \sqrt{\frac{1}{2} + n + \sqrt{n(n+1)}}. \tag{3.3.8}$$

Here $\hat{\omega} > 0$ is understood. For low frequencies obeying the left inequality, the term $\hat{\omega}^2$ in the left-hand side of eq. (3.3.7) can be neglected. The approximate result

$$\hat{\omega} \approx \frac{-\hat{k}}{\hat{k}^2 + (2n + 1)} \tag{3.3.9}$$

is a typical dispersion relation for a *Rossby wave*. These waves are always traveling westwards, as the zonal phase velocity $\hat{\omega}/\hat{k}$ is negative. However, the group velocity can still become positive for high wave numbers.

The inequality on the right-hand side of eq. (3.3.8) holds in case of high frequencies. Dropping the term with $1/\hat{\omega}$ in the left-hand side of eq. (3.3.7) then gives back

$$\hat{\omega} \approx \pm\sqrt{\hat{k}^2 + (2n + 1)}, \tag{3.3.10}$$

which approximates the dispersion relation for *Poincaré waves* or *gravity-inertial waves* that travel in either direction.

Lastly, if $n = 0$, eq. (3.3.7) can be written as $(\hat{\omega} + \hat{k})(\hat{\omega}^2 - \hat{\omega}\hat{k} - 1) = 0$. From the second bracket, the third type of wave has the dispersion relation

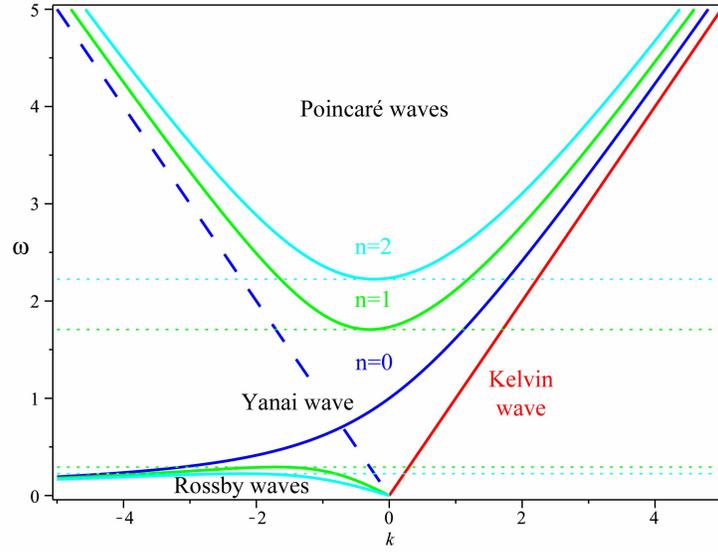$$\hat{k} = \hat{\omega} - \frac{1}{\hat{\omega}}. \tag{3.3.11}$$

Figure 3.4: Wave spectrum for the shallow-water approach. As pointed out in the text, the Kelvin wave (red line) is added artificially whereas its counterpart with negative phase velocity has to be discarded (dashed blue line). The dotted lines indicate the limiting frequencies from eq. (3.3.8).

This wave is called *Yanai wave* or *mixed Rossby-gravity wave*, as it behaves like a Rossby wave for small frequencies and like a gravity-inertial wave for large frequencies. So far, it is the only wave without a frequency gap, as can be seen from figure 3.4.

The other root in case of $n = 0$ is $\hat{\omega} = -c\hat{k}$, which implies that the meridional velocity is $v = C \cdot e^{-y^2/2} e^{ik(x+ct)}$. The remaining fields then must not be computed with eq. (3.3.6b) and eq. (3.3.6c), as the denominator becomes zero. Going back to the original system (3.3.1a)-(3.3.1c) and assuming that

$$u = \tilde{u}(y)e^{ik(x+ct)} \qquad \text{and} \qquad h = \tilde{h}(y)e^{ik(x+ct)},$$

the meridional structure is found to be determined by the differential equations

$$y\tilde{u} - \tilde{u}' = i\left(\frac{1}{\hat{k}}(1 - \hat{y}^2) - \hat{k}\right)e^{-\frac{\hat{y}^2}{2}} \qquad \text{and} \qquad y\tilde{h} - \tilde{h}' = i\frac{c}{g}\left(\hat{k} - \frac{\hat{y}^2}{\hat{k}}\right)e^{-\frac{\hat{y}^2}{2}}.$$

The solutions to these equations turn out to be proportional to $e^{\hat{y}^2/2}$ (except for the very special case $\hat{k} = \frac{1}{\sqrt{2}}$) and therefore do not match the boundary conditions.

However, there is another wave belonging to the full spectrum, namely the equatorial Kelvin wave already discussed in section 3.1. Since an equation for v was deduced to find solutions to the problem, the case $v \equiv 0$ belonging also to the spectrum of the full system eq. (3.3.1a)-(3.3.1c) got lost. Thus, it has to be added "by hand" again, and consequently, also the Kelvin wave is shown in figure 3.4. Altogether, these wave solutions form a complete set of eigenfunctions for the unforced system.

Long wave limit. Forced problems and adjustment processes usually are handled in the long wave limit, that corresponds to setting $\epsilon = 0$ as mentioned above. Then the dispersion relation from eq. (3.3.5) simplifies to

$$\hat{\omega} = \frac{-\hat{k}}{(2n+1)}.$$

This matches with the long wave limit $k \to 0$ of eq. (3.3.9) and hence represents non-dispersive long Rossby waves that apparently always travel westwards. Having the maxima of their amplitude beside
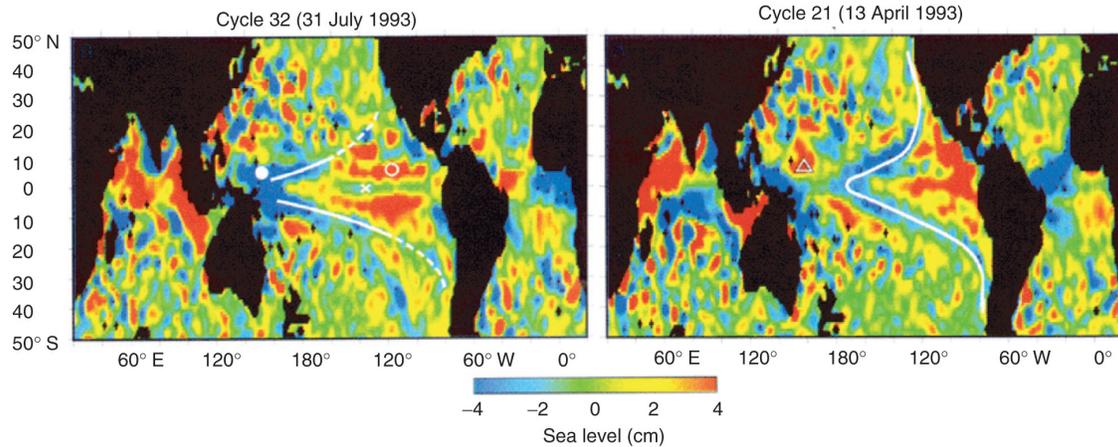
Figure 3.5: A Long Rossby wave traveling across the Pacific, sea level anomalies from TOPEX/PO-SEIDON data. The propagation speed decreases away from the Equator due to the change of the Coriolis force (picture from Chelton and Schlax, 1996).

the Equator like depicted in figure 3.3, long Rossby waves of even order are thought to constitute the disturbances in the left-hand side of figure 3.1 and in figure 3.5.

Another interesting property of these waves is the fact that, at zonal boundaries, Rossby waves reflect partly into equatorial and coastal Kelvin waves and vice versa. Experimental evidence for this was given (amongst others) by Boulanger and Fu (1996), who furthermore explain 80% of their sea level data (that was filtered to keep only the slow variations) only by means of Kelvin waves and first order Rossby waves.

3.4   Limitations of this approach

On a first glimpse, the classical shallow water theory of equatorial waves gives a self-contained picture of large-scale processes. It becomes particularly interesting as it provides a complete set of functions (in terms of Hermite polynomials) that allow to describe disturbances and forcing. However, several questionable points come along with this theory, that are calling for improvements.

One flaw lies in the usage of the reduced gravity model. This model involves an infinitely steep thermocline and a completely motionless lower layer, both of them clearly being coarse approximations. Moreover, the choice for this model rather than for a surface wave model is often reasoned with the better matching of observed velocity, which seems to be a somewhat arbitrary argument. Lastly it should be mentioned that the velocity field obtained in this approach can satisfy the appropriate boundary conditions at the interface, but *not* at the upper surface (as this would lead to the dispersion relation for surface waves again). The surface elevation is determined differently.

Another interesting point lies in the interpretation of the shallow water equations, as already mentioned before. Regarding them as depth integrated relations, all interior dynamics within a layer are neglected. However, not all of the more general solutions that will be derived in the following chapters will transform into Matsuno's solutions in a suitable limit or after depth integration, respectively. This is in a way questioning the validity of the shallow water equations here.

Furthermore, the experimental verification of this kind of long-term theories is difficult in real context: the data is quite noisy on the long time scales considered here, and it involves many processes on shorter time scales such as tides. Hence, it has to be preprocessed and filtered strongly, which in turn might influence the results in some cases. Finally, there is always some piece of interpretation needed.

Chapter 4

Nontraditional equatorial Kelvin waves

In the following, the relevance of Kelvin wave-like solutions (i.e. $v \equiv 0$) that include the full Coriolis force and (constant) buoyancy terms is discussed for processes in the equatorial ocean. Raymond (2001) analyzed similar solutions for the atmospheric case, but without applying boundary conditions. This latter step however is crucial in the oceanographic case, as it will finally inhibit a wide class of nontraditional equatorial Kelvin waves.

In order to verify the results, the limit is inspected, in which the classical Kelvin waves presented in the preceding chapter occur.

The full system eq. (2.5.1a)-(2.5.1e) is considered for $v \equiv 0$, where also the time derivative of w is included again:

$$u_t + 2\Omega w = -\frac{1}{\varrho_*}\tilde{p}_x \tag{4.0.1a}$$

$$\frac{2\Omega}{r_0}yu = -\frac{1}{\varrho_*}\tilde{p}_y \tag{4.0.1b}$$

$$w_t - 2\Omega u = -\frac{1}{\varrho_*}\tilde{p}_z - b \tag{4.0.1c}$$

$$-wN^2 + \partial_t b = 0 \tag{4.0.1d}$$

$$u_x + w_z = 0 \tag{4.0.1e}$$

The buoyancy frequency N^2 is taken to be constant for the sake of simplicity, corresponding to a linear stratification. Assuming that the time dependence of b is given by $e^{-i\omega t}$, one can use eq. (4.0.1d) to eliminate b from eq. (4.0.1c). From the continuity equation (4.0.1e), a stream function $\psi(x, y, z)$ is introduced, such that

$$u = -\psi_z e^{-i\omega t} \qquad \text{and} \qquad w = \psi_x e^{-i\omega t}. \tag{4.0.2}$$

Here, the time dependence is separated for further convenience. The pressure can be eliminated from eq. (4.0.1a)-(4.0.1c) by pairwise combination of derivatives of these equations, this corresponds to taking the curl. Using the abbreviations $\alpha^2 = \frac{N^2}{\omega^2} - 1$ and $\tilde{\omega} = \omega - \frac{N^2}{\omega} = -\alpha^2\omega$ in the following, the new system then reads:

$$\psi_{zz} - \alpha^2 \psi_{xx} = 0 \tag{4.0.3a}$$

$$2\Omega\partial_z\left(\frac{y}{r_0}\psi_z + \psi_y\right) = i\tilde{\omega}\psi_{yx} \tag{4.0.3b}$$

$$-2\Omega\partial_x\left(\frac{y}{r_0}\psi_z + \psi_y\right) = i\omega\psi_{yz} \tag{4.0.3c}$$

At this stage, two remarks can be made: firstly, this system would still be valid if N and hence also α were functions of z. But as the way of solving it would then change drastically, this case is not inspected here.

Secondly, the so-called *hydrostatic term* w_t is taken into account here in contrast to what was done in the classical theory. In case of no buoyancy ($N \equiv 0$), it was found that the absence of this term immediately leads to $u_y = u_z = 0$ and renders the solutions useless, like in Fruman (2009). Otherwise, it results only in a redefinition of $\tilde{\omega}$.

The aim is now to find reasonable solutions to this system, for different limiting cases of the ratios between the parameters as well as for different boundary conditions.

4.1 Problems with fixed boundaries

Most settings in oceanography involve at least one fixed boundary, typically at the bottom, where the normal velocity must vanish. In the following, it is inspected whether solutions to eq. (4.0.3a)-(4.0.3c) can satisfy this type of boundary condition.

New coordinates can be introduced that are motivated by the characteristic curves of the respective equations, reading

$$\chi_+ = x + \alpha z \qquad\qquad \chi_- = x - \alpha z \qquad\qquad \xi = \frac{y^2}{2r_0}.$$

The solution of the Laplace equation (4.0.3a) then can be written as a superposition of two functions depending either on χ_+ or on χ_-,

$$\psi = G^+(\chi_+, \xi) + G^-(\chi_-, \xi).$$

Inserting this in the two remaining equations (4.0.3b) and (4.0.3c), they can be decoupled easily and thus yield one equation for each component of ψ,

$$
\begin{aligned}
\partial_{\chi_+}\left[\left(\frac{i\omega}{2\Omega} + \frac{1}{\alpha}\right)\partial_\xi + \partial_{\chi_+}\right]G^+(\chi_+, \xi) &= 0 \\
\partial_{\chi_-}\left[\left(\frac{i\omega}{2\Omega} - \frac{1}{\alpha}\right)\partial_\xi + \partial_{\chi_-}\right]G^-(\chi_-, \xi) &= 0.
\end{aligned}
$$

Using the abbreviation $\gamma^\pm = \frac{i\omega}{2\Omega} \pm \frac{1}{\alpha}$ and integrating once, both equations take the same form,

$$\left(\gamma^\pm \partial_\xi + \partial_{\chi_\pm}\right) G^\pm(\chi_\pm, \xi) = C^\pm(\xi). \tag{4.1.1}$$

Here, the $C^\pm$ are arbitrary functions of ξ only. Dropping the index for a moment, the solution of the latter equation turns out to be

$$G(\chi, \xi) = G_H(\xi - \gamma\chi) + \frac{1}{\gamma}\int\limits_{\xi_0}^{\xi} C(\tilde{\xi})\,d\tilde{\xi}. \tag{4.1.2}$$

This solution of the inhomogeneous equation (4.1.1) was obtained by the method of characteristics, see Courant and Hilbert (1968). The solution G_H of the corresponding homogeneous equation depends only on $(\xi - \gamma\chi)$. Note however that the constants $C^\pm$ do not have any physical meaning. As they depend on y only and consequently drop out by computing the velocities from ψ, we set them to zero. Hence, the stream function reads

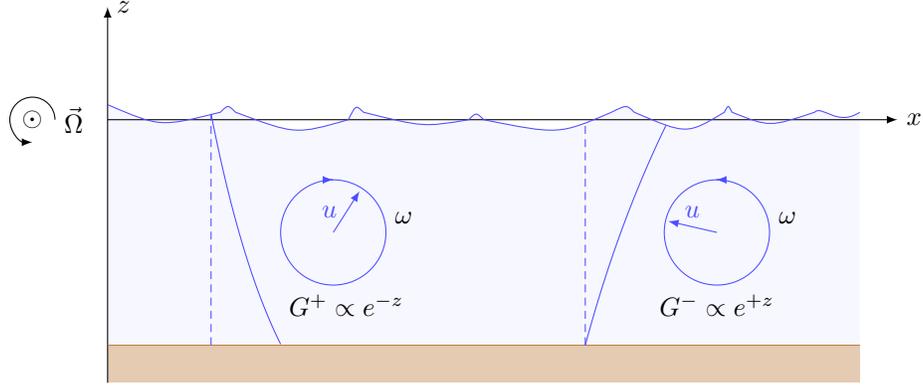$$\psi = G^+(\xi - \gamma^+\chi_+) + G^-(\xi - \gamma^-\chi_-),$$

Figure 4.1: The different behavior at $y = 0$ of the nontraditional solutions G^+ and G^-, respectively: both the rotation direction of $\vec{u}$ and the vertical shear are opposite. The wavelength of the co-rotating component G^- is shortened in comparison to the traditional case, whereas the wavelength of the component $G^+$is prolonged, see text.

or in the old coordinates

$$\psi = G^+ \left(\frac{y^2}{2r_0} - i(\frac{\omega}{2\Omega} - \frac{i}{\alpha})(x + \alpha z) \right) + G^- \left(\frac{y^2}{2r_0} - i(\frac{\omega}{2\Omega} + \frac{i}{\alpha})(x - \alpha z) \right) \qquad (4.1.3)$$

Next, a fixed boundary is considered, which can be chosen without loss of generality at $z = 0$. The condition $\psi_x|_{z=0} \equiv w|_{z=0} = 0$ reads in terms of the new coordinates

$$\partial_{\chi_+} G^+ \big|_{\chi_+ = \chi} + \partial_{\chi_-} G^- \big|_{\chi_- = \chi} = 0,$$

where $\chi_+ = \chi_- = \chi$ at $z = 0$. Using the explicit form of the solution (4.1.2), the condition

$$-\gamma^+ \left(G_H^+ \right)' (\xi - \gamma^+ \chi) = \gamma^- \left(G_H^- \right)' (\xi - \gamma^- \chi) \qquad \forall \chi, \xi \qquad (4.1.4)$$

results. This cannot be satisfied by *any* functions as $\gamma^+ \neq \gamma^-$ by assumption which verifies the claim that boundary conditions at a fixed boundary cannot be satisfied.

Consequently, nontraditional equatorial Kelvin waves are expected to exist neither in a surface wave setting with a fixed boundary at the bottom nor in the case of internal waves using the rigid-lid-approximation that was described in section 2.6.

An attempt to a physical interpretation. To clarify the effect seen here, a single plane wave is considered in the case of no stratification by choosing $G(X) = Ae^{-k\frac{2\Omega}{\omega}X}$ and $N = 0$. The stream function reads consequently

$$\psi = G^+ + G^- = e^{-\frac{y^2}{2}\frac{k\beta}{\omega}} \left(A^+ e^{ik(1-\frac{2\Omega}{\omega})x} e^{-k(1-\frac{2\Omega}{\omega})z} + A^- e^{ik(1+\frac{2\Omega}{\omega})x} e^{+k(1+\frac{2\Omega}{\omega})z} \right).$$

First of all, one notices that the vertical shear of both components is opposite: while the first component decays for increasing z, the second one decays for decreasing z. Secondly, by computing the contributions $u^\pm$ and $w^\pm$ of each part $G^\pm$ to the velocities separately from eq. (4.0.2), the complex phases between zonal and vertical velocity are found to be

$$\frac{u^+}{w^+} = -i = e^{-i\frac{\pi}{2}} \qquad \text{and} \qquad \frac{u^-}{w^-} = i = e^{+i\frac{\pi}{2}}.$$

Working out these phases with respect to the time dependence $e^{-i\omega t}$, it becomes clear that the real parts of these velocities rotate like:

$$\Re(u^+) \propto \sin\left(\omega t + \phi(\vec{x})\right) \qquad\qquad \Re\left(u^-\right) \propto + \sin\left(\omega t + \phi(\vec{x})\right)$$
$$\Re(w^+) \propto \cos\left(\omega t + \phi(\vec{x})\right) \qquad\qquad \Re\left(w^-\right) \propto - \cos\left(\omega t + \phi(\vec{x})\right)$$

This means that the velocities induced by G^- have the *same* sense of rotation as the Earth's rotation, described by 2Ω, whereas the velocities induced by G^+ rotate in the opposite direction. Somewhat surprisingly, the wavelength of the co-rotating component G^- is shortened compared to the traditional case, and the wavelength of the component $G^+$is prolonged:

$$\lambda^- = \frac{2\pi}{k}\left(\frac{\omega}{\omega+2\Omega}\right) \qquad \lambda^+ = \frac{2\pi}{k}\left(\frac{\omega}{\omega-2\Omega}\right) \qquad \lambda^{\mathrm{trad}} = \frac{2\pi}{k}$$

In the limit of $2\Omega = \omega$, the wavelength of G^- gets halved, while the wavelength of G^+ becomes infinitely long. For $2\Omega = 0$, the shift vanishes as it is supposed to. Figure 4.1 illustrates this situation at $y = 0$.

On a first glimpse, the effect seems to be similar to the classical Doppler effect, but here in the case of waves interacting with a background rotation. Yet, one has to be careful as the term that actually causes this shift is the one reflecting the changes of the $y-$component of $\vec{\Omega}$. In this simple model however the nontraditional component $\tilde{f}_0$ is taken to be constant. Together with the variable $y-$component, the absolute value of $\vec{\Omega}$ is *not* constant. This side effect of the $\beta-$plane approximation renders an exact physical interpretation of this effect difficult.

4.2 Exponentially decaying solutions

The question arises whether solutions can be accepted that decay exponentially far away from a surface instead of vanishing at a fixed boundary (i.e., the bottom), like it is often practiced in atmospheric contexts. These so-called deep water waves do not feel the influence of the bottom at all and are trapped near the surface.

The boundary condition $\psi|_{z=-D} = 0$ is thus replaced by the asymptotic condition,

$$\lim_{z\to-\infty} \psi = 0. \tag{4.2.1}$$

By inserting an ansatz $\tilde{p} = e^{-i\omega t}(P^+ G^+ + P^- G^-)$ with a priori unknown constants $P^\pm$ in the original system eq. (4.0.1a)-(4.0.1c), the pressure can be expressed in terms of the stream function according to

$$\tilde{p} = -\varrho_* 2\Omega\alpha e^{-i\omega t}(\gamma^+ G^+ - \gamma^- G^-). \tag{4.2.2}$$

With the convenient choice $G_k(X) = A_k e^{-Xk/(\frac{\omega}{2\Omega}+1)}$, only $G_k^- = A_k^- e^{-\frac{y^2}{2}\frac{k\beta}{\omega+2\Omega}} e^{k(ix+z)}$ vanishes for $z \to -\infty$ and hence, $G_k^+ \equiv 0$. The surface boundary condition $\tilde{p}_t = \varrho_* g w$ at $z = 0$ from eq. (2.6.3) then yields the dispersion relation

$$k = \frac{\omega^2}{g}\left(\frac{2\Omega}{\omega} - \sqrt{1 - (\frac{N}{\omega})^2}\right).$$

Clearly, the wave number k will become complex in case of $N > \omega$ which leads to a rather complicated mixed oscillating *and* decaying behavior both in x and z.

Additionally, there is another serious problem: as the wave number in the zonal direction only differs by a factor i by the wave number in the vertical direction, the asymptotic condition (4.2.1) can only be satisfied for *deep water waves*, that is, for modes with

$$k \gg \frac{1}{D}.$$

As typically $D \sim 4\,\mathrm{km}$, this leads to relatively short waves that do not match very well with observations. Therefore, this atmospheric approach remains somewhat doubtful in the oceanographic case. Even if this type of waves can exist in reality, they might just not be the waves that where observed so far.

4.3   Traditional shallow water limit

The classical shallow water equatorial Kelvin wave presented in section 3.1 can be found from the more general but unfeasible solutions derived in section 4.1 in a certain limit. This not only affirms the proceeding so far, but also elucidates the character of the "classical" solutions. The following assumptions are necessary:

1. Constant density, meaning no buoyancy such that $N = 0$ and $\alpha^2 = -1$, like in the traditional case.

2. High frequencies with respect to the Earth's rotation, i.e. $\omega \gg 2\Omega$ such that $\gamma^+ = \gamma^- = \frac{i\omega}{2\Omega}$. This assumption is crucial as it enables to satisfy boundary conditions despite eq. (4.1.4) by *neglecting the terms in our solution that are created by the nontraditional Coriolis components.*

3. Later on, the long wave limit $1 \gg |kD|$ is taken with respect to the depth of the basin, which also implies $1 \gg |kz|$. This renders the theory a shallow water approach.

Again, a basin with flat bottom at $z = -D$ is considered here. Now, a smart choice for the arbitrary functions is $G(X) = \sum_k G_k = \sum_k A_k e^{-k\frac{2\Omega}{\omega}X}$. Then the stream function resulting from eq. (4.1.3) is

$$\psi_k = G_k^+ + G_k^- = e^{-\frac{y^2}{2}\frac{k\beta}{\omega}} e^{ikx} \left(A_k^+ e^{-kz} + A_k^- e^{+kz} \right).$$

The boundary condition at the bottom, $\psi_x|_{z=-D} = 0$, fixes one of the constants and we are left with

$$\psi_k = e^{-\frac{y^2}{2}\frac{k\beta}{\omega}} e^{ikx} A_k \left(e^{-k(z+D)} - e^{+k(z+D)} \right).$$

By means of the pressure computed in eq. (4.2.2), the remaining two boundary conditions in eq. (2.6.3) at the upper boundary can be evaluated:

$$\tilde{p}_t|_{z=0} = -i\varrho_* \omega^2 e^{-i\omega t} \left(G^+ - G^- \right)\big|_{z=0} \stackrel{!}{=} \varrho_* g \, w|_{z=0} = i\varrho_* g k e^{-i\omega t} \left(G^+ + G^- \right)\big|_{z=0}$$

$$\Rightarrow \qquad \omega^2 = -gk \left. \frac{G^+ + G^-}{G^+ - G^-} \right|_{z=0} \tag{4.3.1}$$

The ratio between the positive and the negative contributions then has to be estimated in the long wave approximation $1 \gg |kD|$. Then a Taylor expansion $e^{\pm kD} \approx 1 \pm kD$ of the exponential in G^{+-} reproduces the traditional dispersion relation, as

$$\left. \frac{G^+ + G^-}{G^+ - G^-} \right|_{z=0} \approx -kD \qquad \Rightarrow \qquad \frac{\omega^2}{k^2} = gD = c^2, \qquad c > 0. \tag{4.3.2}$$

Still, only a positive phase velocity can be accepted to get bounded solutions. Eventually, the stream function of a traditional Kelvin wave is obtained in this limit (see section 2.7), reading

$$\psi_k e^{-i\omega t} = \tilde{A}_k e^{-y^2 \frac{\beta}{2c}} e^{ik(x-ct)} \left(z + D \right). \tag{4.3.3}$$

This computation can clarify an important assumption obviously underlying the shallow water theory presented in chapter 3: frequencies under consideration have to be considerably higher than the Earth's
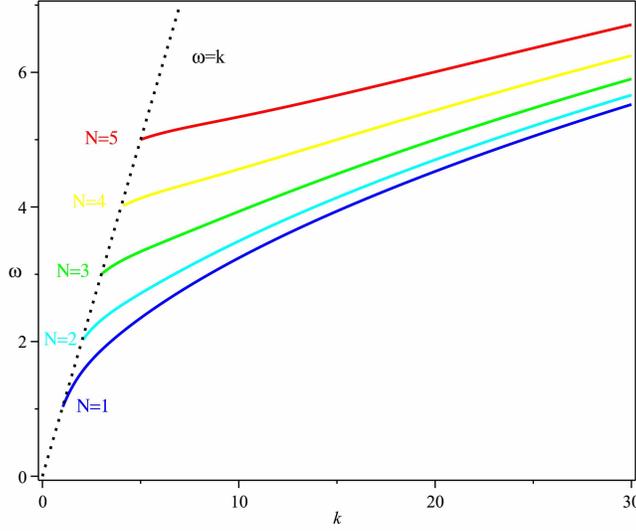
Figure 4.2: For traditional Kelvin waves in a stratified fluid, numerical solutions to the dispersion relation eq. (4.4.3) are shown for different values of N. All other constants are taken to be 1.

rotation frequency to be able to neglect the nontraditional Coriolis terms. As the long wave postulation sets an upper limit to k and the dispersion relation is known, a range can be given for ω, that is

$$2\Omega \ll \omega \equiv ck \ll \frac{c}{D}.$$

If this is evaluated by inserting again the typical magnitudes established in chapter 3, one finds that the angular frequency should obey

$$
\begin{aligned}
\mathcal{O}(10^{-4}\,\mathrm{s}^{-1}) &\ll \omega \ll \mathcal{O}(10^{-1}\,\mathrm{s}^{-1}) && \text{(surface wave) and} \\
\mathcal{O}(10^{-4}\,\mathrm{s}^{-1}) &\ll \omega \ll \mathcal{O}(10^{-2}\,\mathrm{s}^{-1}) && \text{(reduced gravity model).}
\end{aligned}
$$

This corresponds roughly speaking to wave periods between 12 hours and 1 minute. Applications of the classical theory should therefore be checked carefully with regard to these limits.

4.4 Kelvin waves in a stratified fluid

It is possible to relax the restrictions made in the preceding section, neglecting however the non-traditional terms ($\gamma^+ \approx \gamma^-$) to be able to meet boundary conditions, but dropping the long wave approximation and including buoyancy. In case of $\omega^2 < N^2$, α is real and γ splits in a real and an imaginary part, neither of which can be neglected easily. Thus, $\omega^2 > N^2$ is demanded in the following, and it is more convenient to use the real parameter $\tilde{\alpha} = \alpha/i = \sqrt{1 - (N/\omega)^2}$. The condition on the frequency then changes and reads

$$\omega^2 \gg 4\Omega^2 + N^2.$$

Again using $G(X) = \sum_k G_k = \sum_k A_k e^{-k2\Omega X/\omega}$, the contributions for a particular k are

$$\psi_k = e^{-\frac{y^2}{2}\frac{k\beta}{\omega}} e^{ikx} \left(A_k^+ e^{-\tilde{\alpha}kz} + A_k^- e^{-+\tilde{\alpha}kz} \right). \tag{4.4.1}$$

Following the same line as in the previous section and demanding a vanishing ψ at the lower boundary, the solution is first recast as

$$\psi_k = A_k e^{-\frac{y^2}{2}\frac{k\beta}{\omega}} e^{ikx} \sinh(\tilde{\alpha}k(z+D)). \tag{4.4.2}$$

At the upper boundary, the linearized boundary conditions eq. (2.6.3) can be applied again. Similar to eq. (4.3.1), one ends up with

$$\omega^2 = -\frac{gk}{\tilde{a}}\left.\frac{G^+ + G^-}{G^+ - G^-}\right|_{z=0} = \frac{gk}{\tilde{a}}\tanh(\tilde{\alpha}kD). \tag{4.4.3}$$

This dispersion relation looks very similar to the one describing surface gravity waves in a non-rotating fluid! In fact, it is considerably more complicated since the factor $\tilde{\alpha}$ appears that includes stratification but also depends on ω. Some numerical results are shown in figure 4.2. The affinity between surface gravity waves and equatorial Kelvin waves can be clearly seen from this similarity, especially as the rotation manifests itself only in the meridional structure.

4.5   Consequences

Dropping the traditional approximation and inspecting the most simple case of a constant nontraditional term $\tilde{f}_0$ already prevents equatorial Kelvin waves from meeting boundary conditions at a fixed boundary, as it is needed in most of the common settings in oceanography. This important result is not yet covered by the work of Raymond (2001) which focuses more on atmospheric applications. In turn, deep water Kelvin waves with exponentially decaying behavior in the vertical direction might be found, but the short wavelengths that are necessary for the deep water limit do not match with the observations mentioned in chapter 3.

Furthermore, these findings make it unlikely that nontraditional Kelvin waves can be found in more elaborate systems, using for example spherical coordinates instead of the $\beta-$plane approximation.

In the light of section 2.7, the shallow water equations can be regarded to be the lowest order system of a formal power series expansion in the aspect ratio δ of the full set of equations, see section 2.7. In this manner, Dellar and Salmon (2005) computed the nontraditional corrections for some higher orders of δ in a similar setting, including Kelvin waves. The fact that there are no solutions of the Kelvin type to the full system including all boundary conditions, as pointed out in section 4.1, renders at least the Kelvin part of these computations doubtful. Particularly, the convergence of a formal power series like this is not guaranteed by definition.

The classical theory in chapter 3 neglected the nontraditional terms by means of scaling arguments, starting up from the shallow water equations. Only afterward, the low frequency limit is taken that spares only the long Rossby waves. But here, the classical solutions can be reproduced from the full system (4.0.1a)-(4.0.1e) in case of $\omega \gg 2\Omega$, which sets a *lower limit* to the frequency. To a reader who is familiar with inertial waves that will be introduced in section 6.1, this result might be somewhat surprising, since these waves only exist for frequencies $\omega < 2\Omega$. Most likely, these types of oscillating solutions are just not related to internal waves.

As shown in the preceding section, stratification can be included into traditional Kelvin wave theory without any problems, bearing the resemblance to surface gravity waves.

All in all, it seems to be questionable to interpret disturbances moving eastwards automatically as equatorial Kelvin waves. This kind of solutions ceases obviously if one adds only little more realistic ingredients like linear stratification or constant nontraditional terms. As a consequence, there is need for alternative approaches to explain the observed eastwards traveling disturbances near the Equator, like those shown in figure 3.1.

Chapter 5

Other nontraditional equatorial surface waves

In the following, meridional bounded solutions on a nontraditional equatorial $\beta-$plane are inspected that have a non-vanishing meridional velocity. This is an attempt to generalize the work of Matsuno (1966) presented in section 3.3. However, like the Kelvin waves in the preceding section, they turn out to be unable to meet boundary conditions on a fixed surface, except for very special geometries. Despite this serious deficiency, wave-like solutions to this problem are presented here, as they can be compared to other recent efforts.

Similar work was done for example by Fruman (2009) using a hydrostatic model, who concluded erroneously that solutions like those derived in the following are able to satisfy vertical boundary conditions[1]. Roundy and Janiga (2012) recently did a similar analysis for a non-hydrostatic model including buoyancy, but they do not give the explicit expressions of the solutions nor compare them to other approaches.

5.1   Governing equation

To keep things simple, a non-hydrostatic homogenous model is considered. The solutions will turn out to be of a similar form as the solutions obtained in section 3.3, but the method of obtaining them is completely different, as one now has to start from the nontraditional equations

$$\partial_t \vec{u} + 2\vec{\Omega} \times \vec{u} = -\nabla \frac{\tilde{p}}{\varrho_*}, \qquad \text{where} \qquad \vec{\Omega} = \Omega \left(\hat{e}_y + \frac{y}{r_0} \hat{e_z} \right). \tag{5.1.1}$$

Taking the curl yields the vorticity balance

$$\partial_t (\nabla \times \vec{u}) + \beta v \hat{e}_z - 2\Omega L \vec{u} = 0, \qquad \text{where} \qquad L = \partial_y + \frac{y}{r_0} \partial_z.$$

Now, it is assumed that all quantities are proportional to $e^{-i\omega t}$, such that the substitution $\partial_t \to -i\omega$ can be made. Taking the curl again gives then, after using $\nabla \cdot \vec{u} = 0$ as well as the latter equation,

$$i\omega \triangle \vec{u} + \beta \begin{pmatrix} v_y - w_z \\ -v_x \\ u_z \end{pmatrix} - \frac{2\Omega}{i\omega} L \begin{pmatrix} 0 \\ 0 \\ \beta v \end{pmatrix} + \frac{(2\Omega)^2}{i\omega} L^2 \vec{u} = 0. \tag{5.1.2}$$

---

[1] The vertical velocity in eq. (2.24) in Fruman (2009) satisfies the boundary conditions, but it is not a solution to the whole system due to a wrong integration constant.

Here, the square of L has to be computed using Leibniz's rule, $L^2 = \partial_y^2 + 2\frac{y}{r_0}\partial_z\partial_y + \left(\frac{y}{r_0}\right)^2\partial_z^2 + \frac{1}{r_0}\partial_z$. These governing equations are to be solved in the following. The key to do so lies in the fact that the second line constitutes an equation for v alone.

First, proportionality to e^{ikx} is assumed for all quantities by substituting $\partial_x \to ik$, such that a particular Fourier component is considered. This is possible without loss of generality as there are no mixed derivatives or couplings, respectively, that involve the zonal direction. Furthermore, a normalized frequency $\hat{\omega} = \frac{\omega}{2\Omega}$ is used. The second line then eventually reads

$$\left[-\left((\hat{\omega}k)^2 + \frac{\hat{\omega}k}{r_0}\right) + \left(\hat{\omega}^2 - 1\right)\partial_y^2 + \left(\hat{\omega}^2 - \left(\frac{y}{r_0}\right)^2\right)\partial_z^2 - 2\frac{y}{r_0}\partial_y\partial_z - \frac{1}{r_0}\partial_z\right]v = 0. \qquad (5.1.3)$$

Characteristic curves. The behavior of this latter equation is shortly analyzed by means of its characteristics. This also provides a more convenient set of coordinates.

Eq. (5.1.3) has oscillatory solutions only if it is of the hyperbolic type. The condition for this to happen will turn out to be $\omega < 2\Omega$ or $\hat{\omega} < 1$, respectively. Anticipating this result, scales can be introduced that facilitate the analysis by making the factor in front of ∂_y^2 equal to one:

$$(k,l) = \frac{1}{r_0}(\hat{k},\hat{l}) \qquad y = r_0\sqrt{1-\hat{\omega}^2}\,\hat{y} \qquad (x,z) = r_0(\hat{x},\hat{z}) \qquad t = (2\Omega)^{-1}\hat{t}.$$

With these scales, eq. (5.1.3) becomes consequently

$$\left[-\mu^2 - \partial_{\hat{y}}^2 + \left(\hat{\omega}^2 - (1-\hat{\omega}^2)\hat{y}^2\right)\partial_{\hat{z}}^2 - 2\hat{y}\partial_{\hat{y}}\partial_{\hat{z}} - \partial_{\hat{z}}\right]v = 0, \qquad (5.1.4)$$

where $\mu^2 = \left(\hat{\omega}\hat{k}\right)^2 + \hat{\omega}\hat{k}$. This relation is an extended version of the equation (7.2.1) derived by Stern (1963) that will be covered in detail in chapter 7. Two additional terms appear: μ^2 is due to the zonal wave propagation which is ruled out in Stern's original equation, and the factor $\hat{\omega}^2\hat{y}^2$ appears in front of $\partial_{\hat{z}}^2$ because this model is non-hydrostatic. One should thus be able to compare the solutions obtained here to results from the Stern equation by looking at the case $\hat{\omega}^2 \ll 1$, $k = 0$ at a later stage.

In order to classify the PDE (5.1.4), the factors in front of the derivatives are identified as

$$A = -1, \qquad B = -\hat{y} \qquad \text{and} \qquad C = \hat{\omega}^2 - (1-\hat{\omega}^2)\hat{y}^2.$$

such that $\delta = AC - B^2 = -\hat{\omega}^2\left(1+\hat{y}^2\right) < 0$, following here Bronstein and Semendjajew (2000), p. 541. The equation is indeed hyperbolic for all values of $\hat{y}$, if $\hat{\omega} < 1$ as it was assumed before.

The relation determining the two characteristics is

$$\frac{d\hat{z}}{d\hat{y}} = \frac{B \pm \sqrt{-\delta}}{A} = \hat{y} \pm \hat{\omega}\sqrt{\hat{y}^2+1}.$$

This means that new coordinates resulting from $\hat{z} - \int\frac{B\pm\sqrt{-\delta}}{A}\,d\hat{y} = \chi^{\pm}$ will render the PDE of the form $\partial_{\chi^+}\partial_{\chi^-}v + \cdots = 0$, where *no second derivatives* but only a mixed derivative appears. In contrast, the *mixed derivative* can be removed formally by introducing $\tilde{\xi} = \chi^+ + \chi^-$ and $\tilde{\eta} = \chi^+ - \chi^-$, such that

$$\tilde{\xi} = 2\hat{z} - 2\int\frac{B}{A}\,d\hat{y} = 2\hat{z} - \hat{y}^2$$

$$\tilde{\eta} = -2\int\frac{\sqrt{-\delta}}{A}\,d\hat{y} = \hat{\omega}\hat{y}\sqrt{\hat{y}^2+1} + \hat{\omega}\log\left(2\left(\sqrt{\hat{y}^2+1}+\hat{y}\right)\right)$$

Unfortunately, the latter coordinate is too complicated to work with, but as it is only a function of $\hat{y}$, it is worth to try a simpler approach. Hence, introduce more convenient coordinates via

$$\xi = \hat{z} - \hat{y}^2/2 \qquad \text{and} \qquad \eta = \hat{y}. \qquad (5.1.5)$$

Eq. (5.1.4) then indeed takes a much simpler form, namely

$$\left[\mu^2 + \partial_{\eta}^2 - \hat{\omega}^2(1+\eta^2)\partial_{\xi}^2\right]v = 0.$$

5.2 General free solutions

Adopting all manipulations made so far in the whole system (5.1.2) and using the continuity equation in the first line to replace w_z, the governing equations read

$$\left(-\hat{\omega}^2 k^2 + \hat{\omega}^2(1+\eta^2)\partial_\xi^2 - \partial_\eta^2\right)\vec{u} - i\hat{\omega}\begin{pmatrix} \frac{2}{\sqrt{1-\hat{\omega}^2}}\left(v_\eta - \eta v_\xi\right) + i\hat{k}u \\ -i\hat{k}v \\ u_\xi \end{pmatrix} + \begin{pmatrix} 0 \\ 0 \\ \frac{1}{\sqrt{1-\hat{\omega}^2}}\left(v_\eta - \hat{\omega}^2\eta v_\xi\right) \end{pmatrix} = 0. \tag{5.2.1}$$

First, the equation in the second line is solved by transforming it to Hermite's differential equation in two steps. First, a separation ansatz $v = e^{\hat{l}\xi}V(\eta)$ is inserted, yielding

$$\left[\mu^2 + \partial_\eta^2 - \hat{\omega}^2(1+\eta^2)\hat{l}^2\right]V(\eta) = 0. \tag{5.2.2}$$

By taking $V = e^{-\hat{\omega}\hat{l}\frac{\eta^2}{2}}\mathcal{H}(\sqrt{\hat{\omega}\hat{l}}\eta)$, one finally arrives at Hermite's equation (with $n \in \mathbb{N}_0$):

$$\mathcal{H}_n'' - 2\sqrt{\hat{\omega}\hat{l}}\eta\mathcal{H}_n' + 2n\mathcal{H}_n = 0, \qquad \text{where} \qquad 2n+1 = \frac{\hat{\omega}}{\hat{l}}\left(\hat{k}^2 - \hat{l}^2 + \frac{\hat{k}}{\hat{\omega}}\right). \tag{5.2.3}$$

The solutions are the Hermite polynomials $\mathcal{H}_n$ that were already discussed in section 3.3. Again, only solutions satisfying the quantization condition of n being integer can be accepted, as all other solutions diverge for $y \to \pm\infty$. This yields again the dispersion relation on the right-hand side of eq. (5.2.3).

Note that this transformation works out only for an exponential separation ansatz $v \propto e^{\hat{l}\xi}$, as an oscillatory ansatz $v \propto e^{i\hat{l}\xi}$ would render some coefficients in the dispersion relation imaginary, such that no $n \in \mathbb{N}_0$ could be found[2].

Writing the latter dispersion relation again in terms of dimensional quantities yields

$$\omega_n = -\beta\frac{k - (2n+1)l}{k^2 - l^2}. \tag{5.2.4}$$

First of all, this result is quite different from the dispersion relation eq. (3.3.5) given by Matsuno (1966); in a way it is even simpler as it is linear in ω. The reason for this lies in the non-hydrostaticity of our model, as can be seen by comparison to the *hydrostatic* model that Fruman (2009) uses. The dispersion relation he finds *looks the same* as eq. (3.3.7) given by Matsuno (1966). However, Fruman's quantities are defined completely different, and his model only provides solutions for the stratified case and breaks down for $N = 0$.

Furthermore, eq. (5.2.4) resembles the dispersion relation of Rossby waves induced by the $\beta-$effect, see for example Dijkstra (2008). In eq. (5.2.4), there is however a difference of squared wave numbers in the denominator instead of a sum. The underlying assumption of an exponential rather than an oscillatory behavior in the vertical here is essential. As the vertical wave number also applies to the meridional coordinate, an imaginary number would destroy the proper asymptotic limit. Figure 5.1 shows the dispersion relation for fixed l and several n.

Altogether, a single component of the meridional velocity that is characterized by the wave numbers $(\hat{k}, \hat{l}, n)$ can be written

$$v_{\hat{k},\hat{l},n} = \sqrt{1-\hat{\omega}_n^2}e^{i\left(\hat{k}\hat{x}-\hat{\omega}_n\hat{t}\right)+\hat{l}\left(\hat{z}-(1+\hat{\omega}_n)\frac{\hat{y}^2}{2}\right)}\mathcal{H}_n\left(\hat{y}\sqrt{\hat{\omega}_n\hat{l}}\right). \tag{5.2.5}$$

Here, a frequency-dependent amplitude factor was put in for further convenience. From this result, the other velocity components can be determined: clearly, they must be proportional to the same

---

[2]Strictly speaking, the resulting analogon of eq. (5.2.2) in case of an oscillatory ansatz can be solved in terms of Whittaker functions. But then, it is by no means clear how to solve the remaining PDEs for u and w. Moreover, problems with discontinuities of the Whittaker functions at $y = 0$ appear.
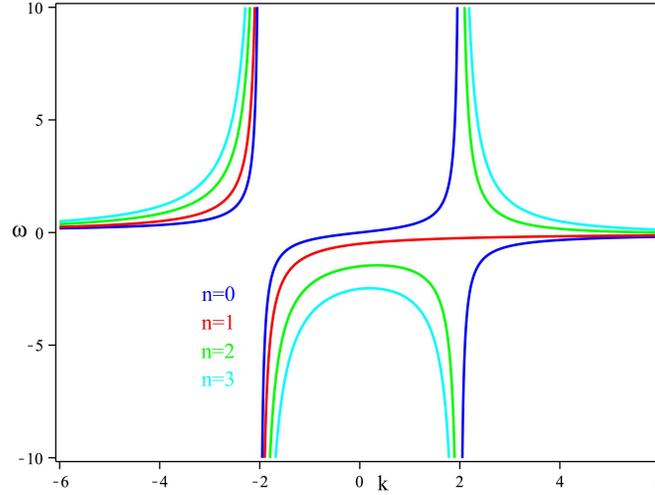
Figure 5.1: The dimensionless dispersion relation corresponding to eq. (5.2.4) for $l = 2$ and several values of n.

exponential function as v. The key to the solutions for u and w lies in the recurrence relations for Hermite polynomials

$$X \cdot \mathcal{H}_n(X) = \frac{1}{2}\mathcal{H}_{n+1}(X) + n\mathcal{H}_{n-1}(X) \qquad \text{and} \qquad \mathcal{H}'_n(X) = 2n\mathcal{H}_{n-1}(X).$$

They permit to convert the $y-$dependencies as well as the derivatives with respect to y simply into algebraic relations. Hence, the components of u and w belonging to a certain $v_{\hat{k},\hat{l},n}$ can only be linear combinations of $\mathcal{H}_{n-1}$ and $\mathcal{H}_{n+1}$, like in section 3.3.

It remains to determine the coefficients of this linear combinations, which is easily done by first computing u from the first line of eq. (5.2.1) that does not depend on w, and then proceeding with the third line. The result is

$$u_{\hat{k},\hat{l},n} = - \; i\sqrt{\frac{\hat{l}}{\hat{\omega}_n}}e^{i\left(\hat{k}\hat{x}-\hat{\omega}_n\hat{t}\right)+\hat{l}\left(\hat{z}-(1+\hat{\omega}_n)\frac{\hat{y}^2}{2}\right)} \left(\frac{\hat{\omega}_n - 1}{\hat{l} - \hat{k}}n\mathcal{H}_{n-1} + \frac{1}{2}\frac{\hat{\omega}_n + 1}{\hat{l} + \hat{k}}\mathcal{H}_{n+1}\right) \qquad (5.2.6)$$

$$w_{\hat{k},\hat{l},n} = \; \sqrt{\frac{\hat{l}}{\hat{\omega}_n}}e^{i\left(\hat{k}\hat{x}-\hat{\omega}_n\hat{t}\right)+\hat{l}\left(\hat{z}-(1+\hat{\omega}_n)\frac{\hat{y}^2}{2}\right)} \left(-\frac{\hat{\omega}_n - 1}{\hat{l} - \hat{k}}n\mathcal{H}_{n-1} + \frac{1}{2}\frac{\hat{\omega}_n + 1}{\hat{l} + \hat{k}}\mathcal{H}_{n+1}\right), \quad (5.2.7)$$

where the argument of the Hermite polynomials is still understood to be $\hat{y}\sqrt{\hat{\omega}_n\hat{l}}$. Of course, it turns out that these solutions also satisfy the continuity equation.

The contribution to the pressure field follows from the first momentum equation in eq. (5.1.1), yielding

$$\hat{p} = \frac{\tilde{p}}{\varrho_* 2\Omega r_0} = i\frac{1 - \hat{\omega}^2}{\hat{l} - \hat{k}}\frac{1}{\sqrt{\hat{\omega}\hat{l}}}e^{i\left(\hat{k}\hat{x}-\hat{\omega}\hat{t}\right)+\hat{l}\left(\hat{z}-(1+\hat{\omega})\frac{\hat{y}^2}{2}\right)} \left(n\mathcal{H}_{n-1} - \frac{1}{2}\mathcal{H}_{n+1}\right). \qquad (5.2.8)$$

The meridional dependence in the exponential reads in dimensional coordinates

$$\hat{l}(1 + \hat{\omega})\frac{\hat{y}^2}{2} = l\frac{2\Omega}{2\Omega - \omega}\frac{y^2}{2},$$

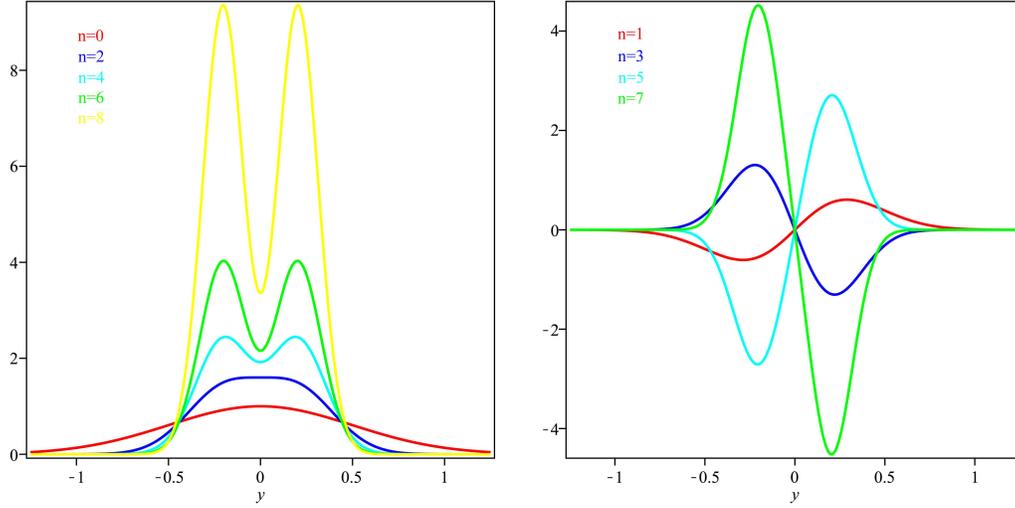which again resembles the Doppler effect-like factors occurring in section 4.1.

Figure 5.2: Functions of the type $e^{\frac{(2n+1)}{2\hat{\omega}}\hat{y}^2}\mathcal{H}_n\left(i\sqrt{2n+1}\cdot\hat{y}\right)$ for $\hat{\omega}=-0.25$. The purely real functions for even n are shown on the left-hand side, the purely imaginary functions for odd n on the right-hand side. Note that the different modes all look similar, in contrast to figure 3.3. Although the real amplitude differences are much bigger, the amplitudes are chosen arbitrary to fit the figure.

5.3   Zonally symmetric solutions

In order to compare the results obtained so far with results stated in Maas and Harlander (2007) that are derived from Stern's equation[3], the limiting case of low frequencies $|\hat{\omega}|\ll 1$ and zonal symmetry $k=0$ has to be considered. Then, the dispersion relation eq. (5.2.4) becomes just

$$\hat{\omega}_n = -\frac{2n+1}{\hat{l}}.$$

This allows to eliminate the wave number $\hat{l}$ but in turn implies that the scale factor $\sqrt{\hat{\omega}_n\hat{l}}$ inside the Hermite polynomials becomes imaginary. These functions look quite different from Hermite polynomials with a real argument, especially as they have only two extremal points at *any* order. In figure 5.2, they are depicted for some values of n.

In Stern's model, the meridional velocity field corresponds to the derivative of a stream function, $v = -\psi_{\hat{z}}^{\mathrm{Stern}} \equiv -\hat{l}\psi^{\mathrm{Stern}}$. For a given frequency $\hat{\omega}$, this velocity here takes the form

$$v_{\hat{\omega},n} = e^{-i\hat{\omega}\hat{t}-\frac{(2n+1)}{\hat{\omega}}(\hat{z}-\frac{\hat{y}^2}{2})}\mathcal{H}_n\left(i\sqrt{2n+1}\cdot\hat{y}\right) \propto \psi^{\mathrm{Stern}}. \tag{5.3.1}$$

Unlike in Maas and Harlander (2007), these solutions are not traveling waves, rather they oscillate in time only. This is caused by a crucial difference in the boundary conditions and will be commented in the next section.

5.4   Comparison to other work

It is quite notable that the velocity components (u,v,w) all share the same non-trivial z dependency in the solutions presented in this section. This is contrary to the classical solutions of Matsuno, where only the vertical velocity is (linearly) dependent on z. It is thus *not* possible to go from the solutions

---

[3]Stern's equation will be treated in section 7.1.

presented in section 5.2 to Matsuno's solutions by taking a certain limit, like it was possible with the equatorial Kelvin waves in section 4.3.

One possible reason lies in the interpretation of the shallow water equations already mentioned in subsection 2.7.1: upon depth integration, all interior effects are neglected. Or, if one prefers to *assume* that the horizontal velocity components u and v do not depend on z, whole classes of solutions that show a different behavior might be excluded a priori.

If this is the case, then the solutions presented here belong to the same class as the ones presented by Fruman (2009) and Roundy and Janiga (2012), being substantially different from Matsuno's shallow-water solutions. However, there are subtle differences within this class. Fruman uses the hydrostatic approximation but adds buoyancy in his work, while Roundy and Janiga include buoyancy without doing the hydrostatic approximation in their recent publication. Nevertheless, the dispersion relations of both models are consistent with each other and with the one obtained here, again supporting the conjecture made above.

Moreover, there are some delusive similarities between the different classes of solutions: if the dispersion relation of Fruman (2009) is plotted for a constant vertical wave number, it looks exactly like the classical dispersion relation depicted in figure 3.4. Hence, one is tempted to think that his work just generalizes Matsuno's theory. This is absolutely not the case, as can be seen, for example, by the fact that all solutions in his model break down if the buoyancy is taken to be zero. In total contrast, Matsuno's model does not account for buoyancy at all.

By comparing the solutions for the zonally symmetric case depicted in figure 5.2 to the Hermite polynomials in figure 3.3, it appears that all even complex Hermite polynomials have a structure roughly akin to the mode $n = 2$ in figure 3.3. Of all various waves found in the classical theory, it is this mode which is mainly used to explain experimental results as mentioned at the end of section 3.3. Supposed that the solutions from section 5.3 indeed play a role, a unique attribution of experimental results however seems to be difficult.

So far, there are at least two different classes of models for trapped waves on an equatorial β-plane, suffering both from different flaws. While Matsuno's theory is based on the traditional approximation, all attempts presented here fail to satisfy proper *vertical* boundary conditions due to the coupling in the coordinates[4]. This latter problem seems to be a general difficulty when dealing with nontraditional surface waves on a $\beta-$plane.

Equatorial trapping versus meridional oscillation.   Maas and Harlander (2007) give in their eq. (4.8) traveling wave solutions for the zonally symmetric case (Stern equation) that satisfy boundary conditions at constant values of ξ as defined in eq. (5.1.5). Their solutions do not have to obey a dispersion relation. This difference is however not surprising, as they are considering *meridionally unbounded* waves, contrary to what was done here.

The waves presented here are in fact not "traveling" in y-direction due to the boundary condition $\vec{u} \to 0$ for $y \to \pm\infty$, the trapping, which in turn does imply a dispersion relation. One may understand this again as a consequence of the coupling between $y-$ and $z-$direction of the system: among other difficulties, it is seemingly impossible to impose an asymptotic boundary condition in one of these directions, say y, while demanding fixed boundaries in the other direction, say z, or vice versa.

One way out of this dilemma might be the introduction of fixed boundaries in $y-$direction. This approach finds its justification in the presence of turning surfaces for inertial-internal gravity waves that are acting as impenetrable walls and will be presented in the next chapter.

---

[4]It was however already pointed out in section 3.4 that in a reduced gravity model, the classical solutions do not obey the proper boundary conditions at the sea surface, either.

Chapter 6

Internal waves

All waves tackled so far were basically *surface waves* that have their maximum amplitude on the sea surface and decay with increasing depth. This type of waves are the most familiar to us, as we can perceive them easily with the naked eye. Even waves traveling along the interface between two fluid layers like in the reduced-gravity model presented in chapter 3 are surface waves in a mathematical sense.

In this chapter, internal waves having a continuous vertical structure are introduced that persist even if surface effects are not taken into account. Since their amplitude is maximal in the interior of the sea, they are much harder to observe. An overview of their sometimes counter-intuitive properties is given in the first section, while the second section is dedicated to the difficulties arising from the specific situation in the Earth's ocean and their possibly singular behavior. Lastly, the astonishing concept of wave attractors is demonstrated on the basis of a particular example.

6.1 Inertial-internal gravity waves

In order to get oscillatory motions, restoring forces that support such motions are indispensable. In a rotating stratified fluid like the ocean, buoyancy as well as inertia due to angular momentum can exert restoring forces to a water parcel. Internal waves induced by perturbing the stratification in density or angular momentum are called consequently *internal gravity waves* and *inertial* (or *gyroscopic*) *waves*, respectively. A basic example that takes into account both effects is considered in the following, which leads to *mixed inertial - internal gravity waves*.

In order to illustrate the general and essential properties of such waves, the framework is simplified by neglecting the $\beta-$effect and restricting to the $f-$plane in the following. To do so, the constant coefficients $f_0 = 2\Omega \sin \varphi_0$ and $\tilde{f}_0 = 2\Omega \cos \varphi_0$ are used, where φ_0 is a constant local latitude. Advantageously, results obtained in this way are not only valid at the Equator, but in turn they hold in a small area around a central latitude φ_0 only.

Taking N to be constant and using the rescaled pressure $P = \tilde{p}/\varrho_*$ for convenience, the governing equations may be formulated as:

$$-i\omega u - f_0 v + \tilde{f}_0 w = -P_x \tag{6.1.1a}$$

$$-i\omega v + f_0 u = -P_y \tag{6.1.1b}$$

$$-i\omega \left(1 - \frac{N^2}{\omega^2}\right) w - \tilde{f}_0 u = -P_z \tag{6.1.1c}$$

$$u_x + v_y + w_z = 0 \tag{6.1.1d}$$

The coordinates defined in subsection 2.4 are used again, such that gravity points in negative $z-$direction. Moreover, it is assumed that the time dependency of all quantities is just $e^{-i\omega t}$. Unlike

what is done in most textbooks like LeBlond and Mysak (1978), a pressure equation will form the basis of the further derivation here. First, the velocities are expressed in terms of the pressure from the momentum equations:

$$v = -\frac{i}{\omega}\left(f_0 u + P_y\right) \qquad w = \frac{i}{\omega(1 - \frac{N^2}{\omega^2})}\left(\tilde{f}_0 u - P_z\right) \qquad u = \frac{(i\omega P_x - f_0 P_y)\left(\omega^2 - N^2\right) + \tilde{f}_0\omega^2 P_z}{(f_0^2 - \omega^2)(\omega^2 - N^2) + \tilde{f}_0\omega^2}$$

Application of these relations to the continuity equation (6.1.1d) yields an equation containing P only. The same relations could be used to get explicit expressions for the velocity fields once the pressure equation is solved. This equation turns out to be

$$\left(\omega^2 - N^2\right) P_{xx} + \left(\omega^2 - N^2 - \tilde{f}_0^2\right) P_{yy} - 2f_0\tilde{f}_0 P_{yz} + \left(\omega^2 - f_0^2\right) P_{zz} = 0. \tag{6.1.2}$$

Plane wave solutions $P_{\vec{k}} \propto e^{i\vec{k}\cdot\vec{x}}$ to the latter equation are found, where $\vec{k} = (k, l, m)^T$. They are subject to the dispersion relation

$$\begin{aligned}
\omega^2 &= N^2 \frac{k^2 + l^2}{k^2 + l^2 + m^2} + (2\Omega)^2\frac{(l\cos\varphi_0 + m\sin\varphi_0)^2}{k^2 + l^2 + m^2} \\
&= N^2\cos^2\vartheta + (2\Omega)^2\cos^2\alpha.
\end{aligned} \tag{6.1.3}$$

Here, ϑ is the angle between $\vec{k}$ and the $x-y$ plane (thus the plane perpendicular to the gravity vector $\vec{g}$), and α is the angle between $\vec{k}$ and $\vec{\Omega} = (0, \Omega\cos\varphi_0, \Omega\sin\varphi_0)^T$. Apparently, the frequency depends only on these angles but not on the absolute value of $\vec{k}$ (or its components), which is a surprising feature of such waves. For a fixed frequency, the admissible values of $\vec{k}$ lie on cones, as it is depicted for various situations in figure 6.1.

It becomes immediately clear from the dispersion relation that the frequency is bounded by the condition

$$\omega^2 < N^2 + 4\Omega^2. \tag{6.1.4}$$

Remarkably, it appears that all waves *must have* a meridional component in case of $N \equiv 0$ due to eq. (6.1.4) right at the Equator, as otherwise $\alpha = 0$ and hence $\omega = 0$, too. This fact is worth noting, as at an earlier stage in section 3.1, Kelvin waves were presented that are just characterized by a vanishing meridional component. Yet, they are surface waves and they were found in models including the $\beta-$effect only.

The group velocity turns out to be

$$\vec{c}_{\mathrm{gr}} = \frac{1}{\omega\vec{k}^2}\left[\vec{k}^2\begin{pmatrix} N^2 k \\ (N^2 + 4\Omega^2\cos^2\varphi_0)l \\ 4\Omega^2\sin^2\varphi_0 m \end{pmatrix} - \left(N^2(k^2 + l^2) + 4\Omega^2(l^2\cos^2\varphi_0 + m^2\sin^2\varphi_0)\right)\begin{pmatrix} k \\ l \\ m \end{pmatrix}\right].$$

With this expression, it is easy to check that the group velocity is always perpendicular to $\vec{k}$ (and hence to the phase velocity) for waves of this type.

Turning surfaces.   Like it was done in previous chapters, the partial differential equation (6.1.2) can be classified from a mathematical viewpoint, which will reveal an interesting feature. Firstly, restrict to the case of lacking zonal propagation for a moment, which means $\partial_x \equiv 0$ in eq. (6.1.2). Only the derivatives in y and z remain, and the factors in front of these terms are identified as

$$A = \omega^2 - N^2 - \tilde{f}_0^2 \qquad B = -f_0\tilde{f}_0 \qquad \text{and} \qquad C = \omega^2 - f_0^2.$$

Oscillating solutions exist consequently, if

$$AC - B^2 = \omega^2\left(\omega^2 - N^2 - 4\Omega^2\right) + 4\Omega^2 N^2\sin^2\varphi_0 < 0. \tag{6.1.5}$$
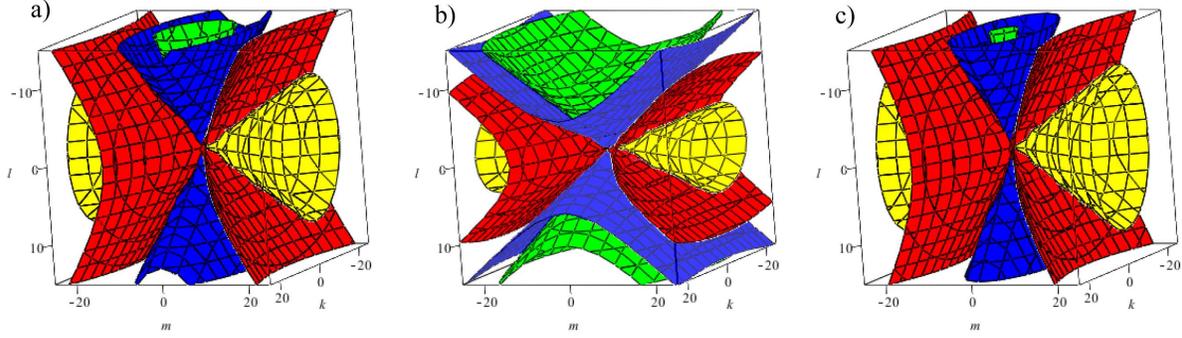
Figure 6.1: Values for $\vec{k} = (k, l, m)^T$ resulting from eq. (6.1.3) are plotted for different frequencies $\omega = 1$ (yellow), $\omega = 1.8$ (red), $\omega = 2.2$ (blue) and $\omega = 2.5$ (green). The situation $\varphi_0 = 0$ right at the Equator is shown, such that $\vec{\Omega}$ points in $l-$direction and $\vec{g}$ points in negative $m-$direction. For $\omega < N$, $\vec{k}$ lies on a cone aligned with the rotation axis, whereas for $\omega > N$, $\vec{k}$ lies on a cone aligned with gravity. $N = 2$ is kept fixed. (a) $\Omega = \frac{N}{2}$ (b) $\Omega = N$ (c) $\Omega \ll N$.

This is the condition for eq. (6.1.2) to be of the *hyperbolic type*, and it also illustrates the symmetric role of N and 2Ω. The definitions of the Coriolis parameters have been inserted again, and consequently, the latter relation is solved for φ_0 in case ω is given. This establishes the *critical latitudes*[1] (Hughes 1964; LeBlond and Mysak 1978; Gerkema et al. 2008)

$$\varphi_0^{(c)} = \pm \arcsin \left[\frac{\omega^2}{4\Omega^2} + \frac{\omega^2}{N^2} \left(1 - \frac{\omega^2}{4\Omega^2} \right) \right]^{1/2}. \tag{6.1.6}$$

This equation has a striking meaning, as it defines a frequency range within which the waves can exist for given central latitude as depicted in figure 6.2. With increasing latitude, this frequency band becomes smaller. Waves traveling polewards that are created at low latitudes may thus reach a critical latitude that they cannot cross. In the area beyond $\varphi_0^{(c)}(\omega)$, only exponentially decaying solutions exist and the medium becomes non-permeable. Hence, the waves will be reflected by their so-called *turning surfaces* which coincide in this simple view with the surfaces defined by $\varphi_0^{(c)}$, and there is no energy flux into the non-permeable area[2]. This insight could motivate the usage of fixed boundaries in the $y-$direction under certain circumstances.

The behavior of the critical latitude also depends strongly on the presence of nontraditional terms: by looking at the traditional version ($\tilde{f}_0 \equiv 0$) of the hyperbolicity condition eq. (6.1.5)

$$\left(\omega_{\text{TA}}^2 - f_0^2 \right) \left(\omega_{\text{TA}}^2 - N^2 \right) < 0 \quad \Rightarrow \quad \min(|f_0|, N) < \omega_{\text{TA}} < \max(|f_0|, N), \tag{6.1.7}$$

it appears that only one of the bounds on frequency is latitude-dependent under the traditional approximation. It corresponds to the "traditional" critical latitude

$$\varphi_0^{(c, \text{TA})} = \pm \arcsin \left(\frac{\omega}{2\Omega} \right), \tag{6.1.8}$$

whereas the buoyancy frequency N constitutes the second bound in the traditional case. Thus, the curves in figure 6.2 are then cut by the dashed line associated with N.

If waves are considered that lack meridional propagation, then $\partial_y \equiv 0$ in eq. (6.1.2). The resulting (nontraditional) turning latitude then coincides with the traditional result eq. (6.1.8), which can be

---

[1]It should be noted that the term "critical latitude" is used differently by different authors, which may create some confusion.

[2]This process is somewhat similar to the total reflection of electromagnetic waves; however, Snell's law does *not hold* for internal waves!
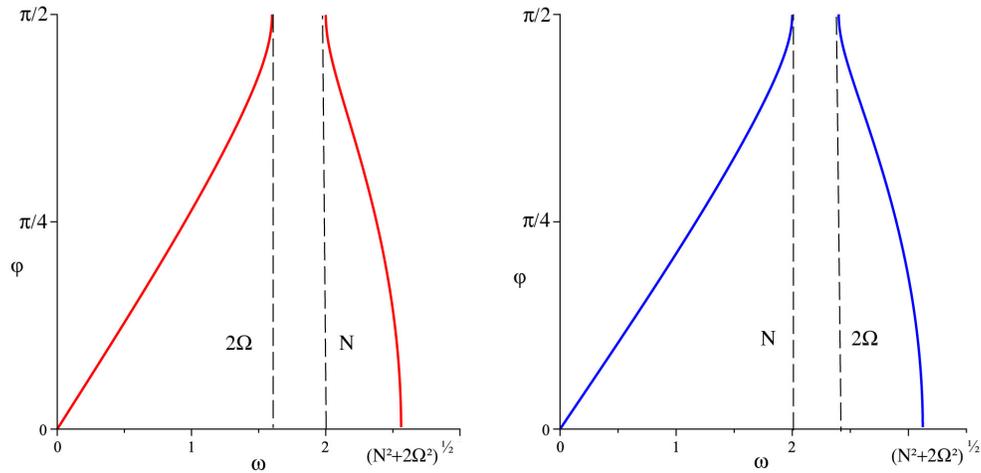
Figure 6.2: Critical latitude $\varphi_0^{(c)}$ as a function of ω for waves lacking zonal propagation according to eq. (6.1.6). On the left-hand side, $2\Omega = 1.6 < N = 2$, while on the right-hand side $N = 2 < 2\Omega = 2.4$. In the frequency band between these boundaries, there are no restrictions on latitude. Typically, $2\Omega < N$ is found in the ocean.

seen directly from eq. (6.1.2) or from the fact that eq. (6.1.3) then reduces to

$$\omega^2 = N^2 \cos^2 \vartheta + f^2 \sin^2 \vartheta.$$

For an arbitrary direction of propagation, the result will lie in between these values.

The simple approach to turning latitudes pursued here is based on a $f-$plane, like it was done by LeBlond and Mysak (1978) and Gerkema et al. (2008). While catching some basic features of turning surfaces like their existence and the fact that they depend also on the nontraditional terms, it does however neither account for curvature terms nor for a non-constant buoyancy frequency N. It was put forward for example by Friedlander and Siegmann (1982) and Winters et al. (2011), respectively, that both effects independently can cause the turning surfaces to become dependent on the radial coordinate (in other words, on the depth). This can in turn lead to so-called point attractors at the sea bottom; point attractors will be introduced in section 6.3. Yet, these are purely nontraditional phenomena.

6.2   The challenge of a rotating spherical shell

In the preceding section, an unbounded domain was considered and both the rotation axis and the gravity vector were kept fixed. Adding suitable boundary conditions, some *local* effects involving internal waves might be described by $f-$plane models, even involving the traditional approximation. A prominent example for such local phenomena are the internal wave effects due to the sill in the Strait of Gibraltar. They are documented on many pictures taken from space (see, for example, http://www.internalwaveatlas.com).

However, by looking at the equatorial area, such an approach is not satisfactory since it completely neglects the distinct nature of the equatorial region. It has to be taken into account eventually that the ocean is a thin spherical shell and that the relative orientation between gravity vector and rotation axis depends on position. The resulting task turns out to be extremely difficult, and no exact solutions are known up to now. One reason is that the underlying problem is mathematically ill-posed in a sense that it combines a hyperbolic differential equation (like the pressure equation from the preceding section) with boundary conditions rather than with initial conditions.

Bryan (1889) found implicit solutions for a rotating fluid sphere, and the explicit expressions for the velocity fields were derived recently by Zhang et al. (2001). This latter approach however still involves equations that have to be solved numerically. Numerous attempts to handle the full inviscid problem of a spherical shell were in vain. One can resort to ray theory approaches that are based on the WKB method known also from quantum mechanics, see LeBlond and Mysak (1978). The rays obtained in this way are often directly related to the characteristics of the corresponding differential equation. A description of these characteristics (together with a pressure equation generalizing eq. (6.1.2) and a sophisticated classification of possible solutions) can be found in Friedlander and Siegmann (1982).

Singular solutions? Actually, ray theory and related approximations are beyond the scope of this work which is devoted in first instance to exact solutions and their consequences for the equatorial region. However, using influences from both approaches and applying them to the equatorial region, Bretherton (1964) already proposed a trapping mechanism that may lead to (inviscid) solutions which can become *singular* at certain locations in the fluid domain. The first comprehensive mathematical treatment in this context was given by Stewartson and Rickard (1969), in the following abbreviated as SR. They reported about so-called pathological oscillations of a homogenous rotating fluid in a spherical shell, which where found in the second order of an asymptotic expansion using the thickness of this shell as a small parameter.

Before briefly turning to these astonishing findings, the *lowest order* of this expansion will be discussed critically and it will be revealed that it is at least partly unbounded at the poles. As a consequence, the frequency quantization used by SR may be doubted in the light of contemporary knowledge about internal waves.

Singularities in the lowest order. As the asymptotic expansion of the fields is set up using the thickness of the shell as a parameter, the lowest order corresponds to an infinitely thin shell that does not admit for radial motion. The computation of SR includes the full Coriolis force and is done in spherical coordinates, since the whole domain is under consideration. The key to these previously unnoticed singularities lies in equation (2.13) of SR for the lowest-order meridional velocity. Rewriting this equation in the denomination used here throughout yields

$$\cos^2\varphi \frac{d^2\tilde{v}}{d(\sin\varphi)^2} - 4\sin\varphi \frac{d\tilde{v}}{d(\sin\varphi)} + \left(\frac{2(m-\omega)}{\omega} + \frac{1-m^2}{\cos^2\varphi} \right) \tilde{v} = 0. \tag{6.2.1}$$

Polar oceanographic coordinates as introduced in section 2.3 are used again, with $\varphi \in [-\frac{\pi}{2}, +\frac{\pi}{2}]$ being the latitude. Moreover, m is the zonal wave number resulting from a separation ansatz $\propto e^{im\lambda}$, $\tilde{v} = m \cdot v$ is the rescaled meridional velocity and ω is the frequency as usual. At a first glimpse, this equation might have solutions in terms of associated Legendre functions for certain discrete values of ω which in turn result from the condition that the solutions should be bounded as $\varphi \to \pm\frac{\pi}{2}$. That is what SR state and all in all, this seems to be a typical application of Sturm-Liouville theory.

Unfortunately, eq. (6.2.1) is *not* a Legendre-like equation, as the first derivative of $\tilde{v}$ here has a numerical factor of 4 instead of 2. This tiny detail prevents the equation even from being self-adjoint, meaning that it cannot be written in the form

$$\frac{d}{d(\sin\varphi)} \left(\cos^2\varphi \frac{d\tilde{v}}{d(\sin\varphi)} \right) + Q(\sin\varphi)\, \tilde{v} = 0$$

for some function Q. As a consequence, Sturm-Liouville theory is not applicable so far, and neither boundedness of solutions nor further statements on the spectrum of the eigenvalues ω seem to be possible. To clarify the situation, it is worthwhile to inspect how eq. (6.2.1) is connected to the work done by Haurwitz (1940), to which SR refer in this context. By means of a substitution

$$\tilde{v}(\varphi) = \frac{i}{\cos\varphi} \tilde{\psi}(\sin\varphi), \tag{6.2.2}$$

Haurwitz's equation (11) can indeed be recovered. This equation describes the dynamics of the meridionally dependent part of his stream function which is called $\tilde{\psi}$ here and results from the same type of separation ansatz $\propto e^{im\lambda}$. It reads[3]

$$\cos^2\varphi \frac{d^2\tilde{\psi}}{d(\sin\varphi)^2} - 2\sin\varphi \frac{d\tilde{\psi}}{d(\sin\varphi)} + \left(\frac{2m}{\omega} - \frac{m^2}{\cos^2\varphi}\right)\tilde{\psi} = 0. \qquad (6.2.3)$$

This equation is indeed self-adjoint! One can assure oneself that the corresponding continuity equation $\frac{\partial}{\partial\lambda}u - \cos\varphi\frac{\partial}{\partial(\sin\varphi)}(v\cdot\cos\varphi) = 0$ is automatically satisfied, if the velocities u and v are induced by this stream function according to

$$u = \cos\varphi\frac{\partial}{\partial(\sin\varphi)}\left(e^{im\lambda}\tilde{\psi}\right) \qquad \text{and} \qquad v = \frac{1}{\cos\varphi}\frac{\partial}{\partial\lambda}\left(e^{im\lambda}\tilde{\psi}\right). \qquad (6.2.4)$$

It is well-known that eq. (6.2.3) has bounded solutions in terms of associated Legendre polynomials, if and only if $\omega = \frac{2m}{n(n+1)}$ with integer n, m and $0 \le m \le n$. However, the problems become obvious by looking closer at the meridional velocity v in eq. (6.2.4): it will always diverge at the poles due to the factor $(\cos\varphi)^{-1}$, regardless whether $\tilde{\psi}$ is bounded there or not! An easy calculation shows that, moreover, the pressures field given by SR will also contain a part that is singular at the poles.

From these findings, it becomes clear that already the lowest order solutions in the approach of SR surely contain some singularities, at least in the meridional velocity $\tilde{v}$ which is depicted in figure 6.3. How can this be interpreted, and how might it influence the second-order pathological behavior? Firstly, this fact might not be that surprising at all. If the lowest order was not divergent, we would already have had nice and regularly behaving solutions for non-traditional internal waves in a thin shell with rigid-lid boundary conditions: namely, the ones given by Haurwitz! Such a theory was unfortunately not found up to now, as already pointed out. Secondly, the question arises to what extent the quantization condition that

$$n, m \in \mathbb{N} \qquad \text{in} \qquad \omega = \frac{2m}{n(n+1)}$$

can be sustained from today's point of view, for two reasons:

1. The condition does not allow to remove all polar singularities in the fields, as it is usually required in similar cases to retain physical validity. Only those in the zonal velocity can be removed in this manner.

2. The resulting quantization condition would persist through *all* orders in the approach of SR, meaning that even for a spherical shell of finite thickness, the frequency spectrum would be quantized rather than continuous.

All current understanding of internal wave behavior however predicts a continuous spectrum even in the presence of boundaries, which is thought to be a direct consequence of the independence of frequency and wavelength illustrated by eq. (6.1.3). Finally, it can be remarked that upon admitting non-integer n and m, there is no more reason to rule out the second, linearly independent family of solutions to eq. (6.2.2). These are the well-known *associated Legendre Functions of the Second Kind* that are always divergent at the poles.

As a matter of fact, already the lowest-order solutions discussed by SR show divergences that again illustrate the typical problems in dealing with inertial waves even in rather simplified approaches.

---

[3]An additional parameter α representing the "angular motion of the air motion relative to the earth" used by Haurwitz (1940) is not needed here.
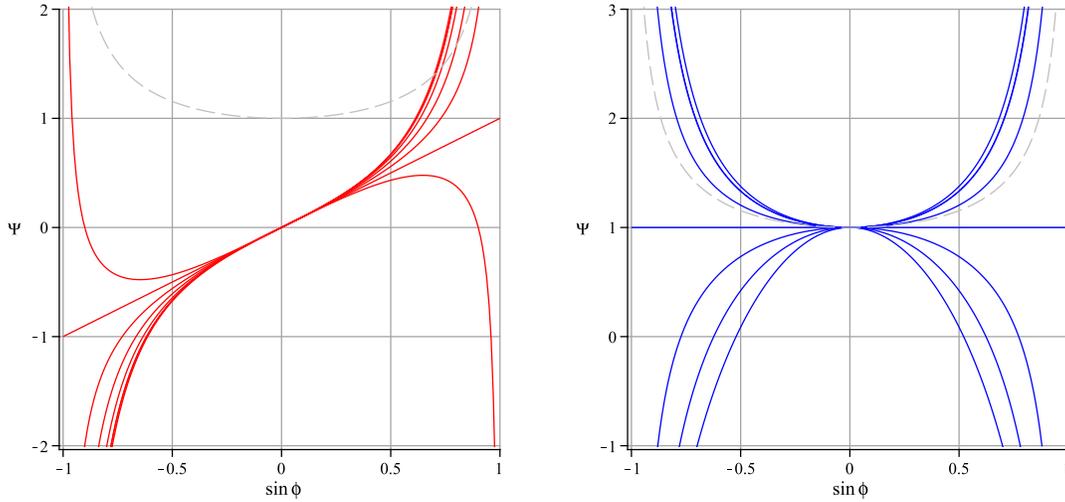
Figure 6.3: The two linearly independent solutions for Ψ resulting from eq. (6.2.1) with $m = 1$ and $\omega = \frac{2}{n(n+1)}$ are plotted for some $n = -1, -\frac{1}{2}, \cdots + \frac{5}{2}$, non-integer as well as integer. All of them diverge at the poles. Only in case of $n = 2$ (left) and $n = 1$, respectively, the solutions are trivially bounded. The dashed gray line shows the function $(\cos\varphi)^{-1}$.

Second-order singularities. While it is not a good basis for an expansion if the lowest order faces serious problems, this does not mean that the conclusions made by SR over the second order have to be generally discarded, especially as they were gained by an enviable mathematical mastery. Remember that many modern (quantum) field theories perpetually face infinities and singularities, and nevertheless, they yield useful results.

The point finally made by SR is that the second order fields in their expansion develop another singularity which is originally located at the cone spanned by

$$\varphi = \pm \arcsin \frac{\omega}{2\Omega}.$$

This is exactly the inertial wave beam defined by eq. (6.1.3) for $N = 0$ and $\alpha + \varphi = \frac{\pi}{2}$, and it can indeed directly be identified with the characteristic curves inspected in this case. After hitting a respective boundary, the singularity spreads along the opposite directed wave beam. In this way, it continues bouncing from one spherical boundary to another along the beams according to SR.

Results like this look suspicious at a first glimpse, and one might rather tend to deny the existence of internal wave solutions for this setting. The wave attractor exemplified in the next section however provides hard evidence that such singular effects really appear in comparable lab experiments.

Of course, the singularities are regularized by viscosity in the real world. Comprehensive numerical simulations including viscosity in a rotating spherical shell that were based on a multipole expansion[4] of the vector fields in terms of vector spherical harmonics were performed by Rieutord and Valdettaro (1997). In this and several subsequent papers, also locally pronounced solutions were found. It is however not clear whether they correspond to the (inviscid) singular solutions discussed so far or to (inviscid) wave attractors, as they can fundamentally change their shape and character upon varying viscosity. This might only illustrate the well-known fact that the limit $\nu \to 0$ can not necessarily be taken in fluid dynamics.

---

[4] Remarkably, there is no coupling between different zonal modes in the dynamical equations resulting from this exact expansion.
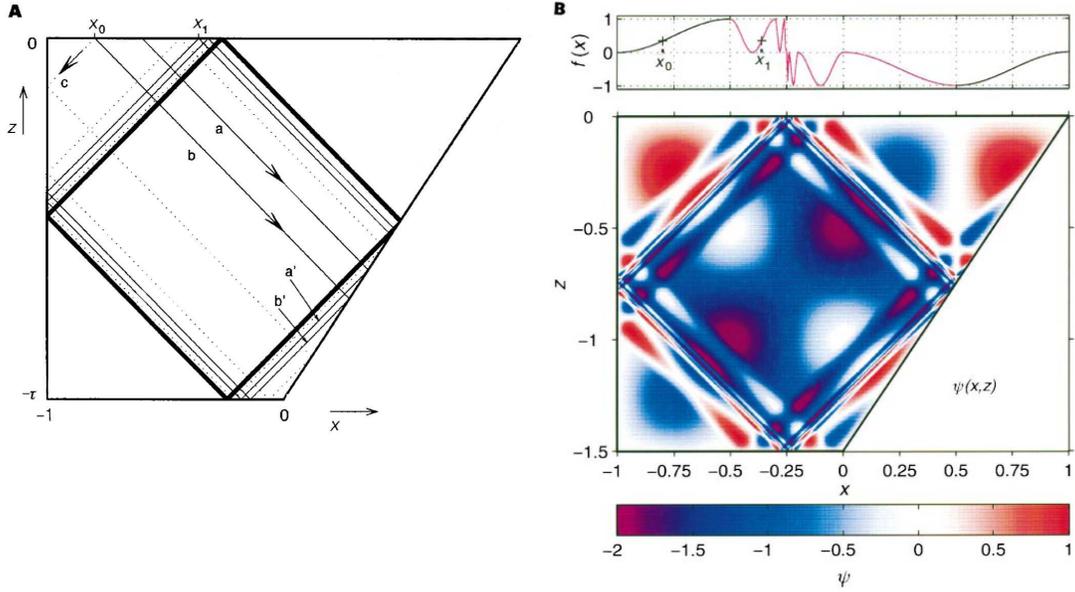
Figure 6.4: (A) Sketch of the basin and the attractor for $\tau = \frac{3}{2}$, the three rays a, b and c all converge towards the attractor. By comparing the distances between a and b and between a' and b', respectively, the focusing due to reflection can be seen clearly. Note that ray c results from ray b upon reversing its direction. (B) The stream function ψ and the function $f(x)$ that is here prescribed on the upper boundary in the intervals $x \in [-1, -\frac{1}{2}]$ and $x \in [\frac{1}{2}, 1]$ are depicted. Both functions show self-similar patterns (from Maas et al., 1997, slightly simplified).

6.3   Wave attractors

A fascinating property of internal waves is their ability to become geometrically focused by the container enclosing them. This phenomenon occurs for nearly all shapes involving some kind of symmetry breaking. The wave field solutions then exhibit so-called *wave attractors* in an inviscid description, that are strongly localized singularities (possibly akin to the second-order singularities described in the preceding section). In the real world, friction regularizes these divergences while their general presence still can be observed.

Away from being an interesting dynamical feature, wave attractors also give rise to another method of constructing solutions through a geometrical and algorithmic approach, and a lot of the pivotal work on this field was done at the NIOZ. Three different aspects of a particular setting featuring a wave attractor are sketched in the following: beside the geometrical construction principle and very extensive experimental results of high quality, also an analytical solution is known for this case, justifying the particular choice.

General setting. A non-rotating two-dimensional domain is considered that contains an incompressible and uniformly stratified ($N = const.$) fluid, where gravity still acts in negative z-direction. This is just a special case of the inertial-internal gravity waves described in section 6.1 and a modified version of eq. (6.1.2) still holds, which is understood to be dimensionless here. Dropping the superfluous terms yields just the two-dimensional hyperbolic wave equation

$$P_{xx} - \frac{1}{\tau^2} P_{zz} = 0, \qquad \text{where} \qquad \tau = \sqrt{\frac{N^2 - \omega^2}{\omega^2}}.$$

Rescaling the coordinates according to $X = x$ and $Z = \tau z$ allows to absorb the only remaining factor τ in this equation, shifting it towards the boundary conditions. Moreover, a stream function ψ can be introduced that turns out to satisfy the same wave equation,

$$\psi_{XX} - \psi_{ZZ} = 0, \tag{6.3.1}$$

having solutions of the well-known form

$$\psi = f^+(X + Z) - f^-(X - Z). \tag{6.3.2}$$

Hence, the two quantities $f^\pm$ remain constant along their corresponding straight lines $X \pm Z = const$. These lines (with slope ± 1) furthermore coincide with the characteristic curves of eq. (6.3.1). The boundary condition $\psi = 0$ along a certain boundary translates then into the functional relation

$$f^+ = f^- \tag{6.3.3}$$

along this boundary.

Originally, analytical solutions of eq. (6.3.1) were only known for some basic geometries. An early attempt to analyze more general topographies mathematically came from Manton and Mysak (1971), who considered an upper boundary at $z = 0$ and a bottom topography $z = -h(x)$. However, it usually fails for closed containers since it requires the integral $\int \frac{dx}{h(x)}$ along the whole length to be finite, which is typically not the case.

Geometrical construction principle. Maas and Lam (1995) firstly added a new point of view to the setting described so far by realizing that the condition eq. (6.3.3) along a boundary can be interpreted as a reflection law: if the partial pressure f^+ has a certain value, say f, along a characteristic curve $X + Z = const$. and this curve hits a boundary, the partial pressure f^- along the outgoing characteristic $X - Z = const$. must have the same value f due to eq. (6.3.3).

Unlike in many other situations in physics, it is symptomatic for this kind of reflections that *the angle with the vertical is preserved*, and not the angle with the normal to the boundary. A particular characteristic curve together with all its subsequent boundary reflections is called a *characteristic web* in this context. Dependent on the shape of a particular domain, basically two things[5] may happen:

1. All characteristic webs are periodic and the distance between two parallel characteristics remains unchanged upon reflection at all boundaries. This happens typically in simple, harmonious geometries like untilted rectangles, for which (separable) analytical solutions were often originally known.

2. The distance between two parallel characteristics changes upon reflection at at least one boundary, owing to its slope or curvature. Only one particular characteristic web is periodic and constitutes a *wave attractor*. All other characteristic webs are infinitely long and converge to this attractor. Surprising phenomena like self-similar scaling behavior of some quantities may occur.

From now on, a geometry of the second kind is considered: the trapezoidal domain enclosed by a horizontal surface at $z = 0$, a vertical side wall at $x = -1$, a horizontal bottom at $z = -\tau$ and a sloping side wall $z = \tau(x - 1)$. Applying the rigid-lid boundary condition at the surface, ψ has to vanish at all boundaries. The left-hand side of figure 6.4 shows this setting and the respective attractor for $\tau = \frac{3}{2}$, on which will be focused.

It was already mentioned that along each characteristic web, the respective partial pressure f remains constant due to eq. (6.3.3). As a consequence, convergence of the characteristic webs towards the attractor and decrease of the distance between parallel characteristics imply that the gradient of

---

[5]As pointed out by Maas and Lam (1995), two asymmetric attractors may appear in certain geometries. Additionally, hybrid situations are possible.
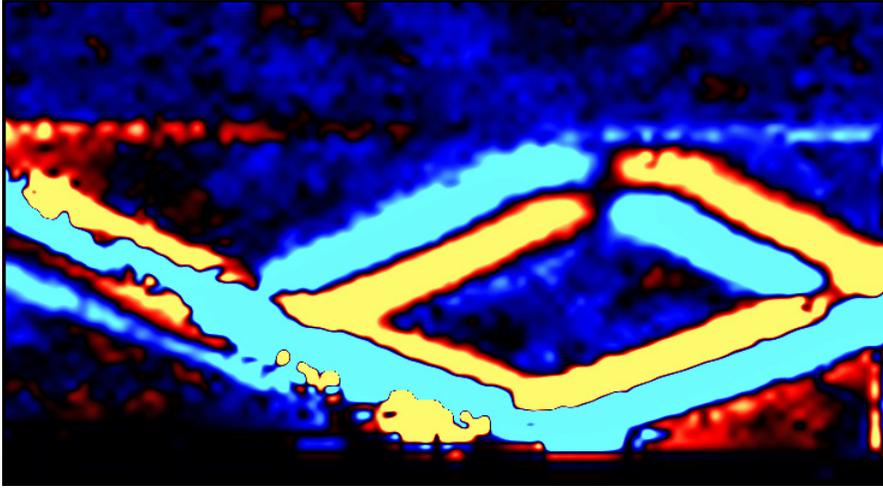
Figure 6.5: A wave attractor observed with the synthetic schlieren method at NIOZ. The sloping wall, which is on the left-hand side in this experiment, can be seen through the additional distortions it causes. The bright red and blue areas correspond to high positive and negative density perturbations with respect to the rest state (thanks to Anna Rabitti for this picture).

the stream function increases by approaching the attractor. It will finally diverge at the attractor, whereas the stream function itself may stay finite.

Furthermore, the stream function in the whole domain can be fixed by prescribing the partial pressure f along the boundary (regarding it as a closed curve) in the so-called *fundamental intervals*. The characteristic curves then project the fundamental intervals allover the boundary. Determining the fundamental intervals is tricky, and in this setting, there are infinitely many possibilities for this choice. For example, x is prescribed in the intervals $[0, \frac{1}{2}]$ and $[\frac{3}{2}, 2]$ along the surface ($z = 0$) in the right-hand side figure 6.4, but the intervals $[0, -\frac{1}{2}]$ and $[-1, \frac{3}{2}]$ for z along the left vertical ($x = -1$) or the intervals $[0, \frac{2}{5}]$ and $[\frac{8}{5}, 1]$ for x on the sloping wall (z corresponding) would be possible just as well.

Figure 6.4 also shows that these fundamental intervals are mapped (or focused) onto smaller and smaller intervals by approaching the attractor, such that the stream function develops a self-similiar structure.

Experimental results.   First experimental observations of attractors in the setting under consideration were reported by Maas et al. (1997), using a rectangular plexiglass container with one sloping wall. Stratification in density was experimentally realized by varying the salinity, and the flow was visualized using dye bands which allows only for a rather coarse resolution.

Recent experiments make use of the "synthetic schlieren" method firstly proposed by Sutherland et al. (1999) that provides a more powerful visualization tool. It is based on the fact that in a uniformly stratified fluid, the refractive index varies due to the variations in density respective salinity. An illuminated pattern behind the transparent tank containing the fluid is monitored by a camera, and local density variations cause local distortions of this pattern. Upon taking a reference picture at a reference time, a computer algorithm can detect and quantify the density variations by comparing the current picture to the reference. Remarkably, the fluid remains several days in a stratified state, once it is prepared by carefully piling water layers of well-defined salinity.

Predefined internal waves can be excited by oscillating the tank either horizontally or vertically with a suitable frequency, which may be a multiple of the frequency to excite. Despite the presence of viscosity and the possible influence of nonlinear effects as well as a moving surface, a strongly localized oscillatory motion is reached after a certain transient period. It forms a stable diamond-shaped pattern that is most pronounced in the predicted area, as depicted in figure 6.5.
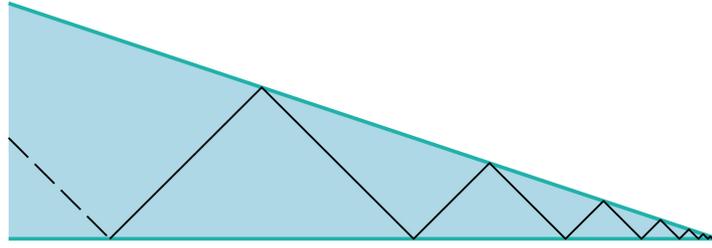
Figure 6.6: Internal wave beams that get trapped in a wedge constitute a point attractor.

Analytical solution.   Maas (2009) succeeded to find an analytical description for this special case of an attractor with $\tau = \frac{3}{2}$. Making use of the fact that a stream function that satisfies the boundary conditions on the three straight walls can be formulated as

$$\psi = \sum_{n=1}^{\infty} a_n \sin \frac{2}{3} n\pi(x+1) \sin \frac{2}{3} n\pi z,$$

the Fourier coefficients a_n were determined such that the fourth boundary condition is obeyed. Particularly, the self-similar mapping that clones the fundamental intervals is used in a tricky manner by choosing these fundamental intervals to lie on the sloping wall, where additionally two symmetry axes appear. It is needless to say that the resulting stream function patterns are akin to the ones found experimentally and geometrically. More surprisingly, the Fourier coefficients turn out to be related to a Weierstrass function, but in its differentiable regime which is *not* self-similar. However, the spectral energy turns out to obey a likewise log-periodicity, showing again self-similarity.

Unfortunately, no general analytical approach to this phenomenon is known up to now. This is contrary to the fact that a periodic orbit constituting an attractor should exist for *every* frequency ω, but its shape can become much more complex, and consequently, the closed trajectory can become much longer. The focusing strength can be described by the *Lyapunov exponent* λ that quantifies how fast two different characteristic webs diverge from each other in time. Since here, the webs in fact approach each other, it always holds that $\lambda < 0$. In general, the focusing strength and hence the absolute value of λ decrease as the length of the attractor increases. By plotting the Lyapunov exponent for different frequencies using numerical simulations, fractal structures are found again.

Point attractors.   In tapered geometries, another kind of attractor may occur whose nature is illustrated in figure 6.6. Due to geometrical reflections, internal wave beams may converge towards the tip of a wedge-shaped domain. This is called a *wedge attractor* or *point attractor*, and its importance is discussed for example in the bottom region of (nontraditional) turning surfaces, see section 6.1.

Chapter 7

The Stern equation

As pointed out in the preceding chapter, the question whether internal waves play a pronounced role in the equatorial region is hard to access mathematically in a direct manner. Hence, further simplifications are needed which again can be achieved by means of multiple scale analysis. In the first section, it is shown how the usage of anisotropic scales directly leads to the equation proposed by Stern (1963), an equation that lacks any zonal dependencies. Subsequently, the structure of its solutions in a domain that is vertically bounded on the top only is revealed.

A proof is given next that an additional boundary at the bottom forces possible inviscid solutions to be either not continuous in every point or constant, provided that the meridional domain is unbounded. These considerations are rather theoretical, but they elucidate again the general difficulties of the problem under consideration. In section 7.4, a frictional boundary layer at the bottom is introduced that is able to close the upper-boundary solutions from section 7.2. It shows however singular behavior for $y = \pm \omega$, similar to the inviscid (!) second-order singularities described by Stewartson and Rickard (1969) mentioned in section 6.2.

7.1 Anisotropic scaling

Usually, horizontally isotropic scales are used to make the governing equations dimensionless, like in section 2.7. In the following, *different* scales are used for the meridional and the zonal directions. This is motivated by the fact that the equatorial area is rather a belt than a square, as it was already pointed out at the end of section 2.7. Starting point is the set of equations

$$-i\omega u - \frac{2\Omega}{r_0} yv + 2\Omega w = -\frac{\tilde{p}_x}{\varrho_*} \tag{7.1.1a}$$

$$-i\omega v + \frac{2\Omega}{r_0} yu = -\frac{\tilde{p}_y}{\varrho_*} \tag{7.1.1b}$$

$$-i\omega w - 2\Omega u = -\frac{\tilde{p}_z}{\varrho_*} + b \tag{7.1.1c}$$

$$-i\omega b + N^2 w = 0 \tag{7.1.1d}$$

$$u_x + v_y + w_z = 0. \tag{7.1.1e}$$

Numerous choices for the scales are possible, but in most of the cases the lowest order system resulting from an asymptotic expansion does not even lead to a pressure equation[1]. Here, two different horizontal length scales but only one horizontal velocity scale are used, which is in good agreement with

---

[1] In the appendix A.1, an example is presented that uses three velocity scales as well as three different length scales. It still leads to a pressure equation. This equation is however always elliptic, and hence, it does *not* exhibit internal wave solutions.

the typical observations made at the Equator that were mentioned in section 1.1. Surprisingly, the result is a slightly extended version of Stern's equation and Stern's equation itself is obtained for the homogenous case $N = 0$. This novel derivation of a well-known relation broadens the scope of possible interpretations, as it will be discussed below.

All quantities in eq. (7.1.1a)-(7.1.1e) are made dimensionless (and thus gain a hat) according to

$$x = L\hat{x} \qquad y = B\hat{y} \qquad z = D\hat{z} \qquad \omega = 2\Omega\frac{D}{B}\hat{\omega} \qquad N = 2\Omega\hat{N}$$

$$u = U\hat{u} \qquad v = U\hat{v} \qquad w = \frac{D}{B}U\hat{w} \qquad \tilde{p} = 2\Omega U D\varrho_*\hat{p} \qquad b = \frac{UN^2}{2\Omega}\hat{b}.$$

Note that the angular frequency 2Ω is used as frequency scale rather than N. Moreover, two fundamental assumptions are made:

1. A realistic zonal length scale for our problems is $L \approx r_0$, as this corresponds to a typical equatorial basin length.

2. The meridional length scale B is chosen in a way that both the traditional and the nontraditional Coriolis terms are of equal impact, $B = \sqrt{r_0 D} \approx 160\,\text{km}$.

Putting this together, it means that $\frac{L}{B} \approx \frac{B}{D}$, which matches the real situation quite well. The small parameter of interest is now $\varepsilon = \frac{B}{L} = \frac{D}{B}$, and from eq. (7.1.1a)-(7.1.1e) we find

$$-i\hat{\omega}\hat{u} - \hat{y}\hat{v} + \hat{w} \quad = \quad -\varepsilon\hat{p}_{\hat{x}} \tag{7.1.2a}$$

$$-i\hat{\omega}\hat{v} + \hat{y}\hat{u} \quad = \quad -\hat{p}_{\hat{y}} \tag{7.1.2b}$$

$$-i\hat{\omega}\left(\varepsilon^2 - \frac{\hat{N}^2}{\hat{\omega}^2}\right)\hat{w} - \hat{u} \quad = \quad -\hat{p}_{\hat{z}} \tag{7.1.2c}$$

$$\varepsilon\hat{u}_{\hat{x}} + \hat{v}_{\hat{y}} + \hat{w}_{\hat{z}} \quad = \quad 0 \tag{7.1.2d}$$

The buoyancy equation again reads $-i\hat{\omega}\hat{b} + \hat{w} = 0$ and is already incorporated in eq. (7.1.2c). An asymptotic power series expansion in ε

$$\vec{u} = \vec{u}^0 + \varepsilon\,\vec{u}^1 + \cdots \qquad \text{and} \qquad p = p^0 + \varepsilon\,p^1 + \cdots \tag{7.1.3}$$

can be performed, where the hats will be dropped from now on. The lowest order balance is then given by

$$-i\omega u^0 - yv^0 + w^0 \quad = \quad 0 \tag{7.1.4a}$$

$$-i\omega v^0 + yu^0 \quad = \quad -p_y^0 \tag{7.1.4b}$$

$$i\frac{N^2}{\omega}w^0 - u^0 \quad = \quad -p_z^0 \tag{7.1.4c}$$

$$v_y^0 + w_z^0 \quad = \quad 0 \tag{7.1.4d}$$

The continuity equation (7.1.4d) allows for a stream function, such that $v^0 = -\psi_z$ and $w^0 = \psi_y$. The zonal velocity is then obtained from eq. (7.1.4a) as $u^0 = -\frac{i}{\omega}(y\psi_z + \psi_y)$, and from the remaining equations we get

$$\left(1 + N^2\right)\psi_{yy} + 2y\psi_{yz} - \left(\omega^2 - y^2\right)\psi_{zz} + \psi_z = 0, \tag{7.1.5}$$

which is Stern's equation extended by the term $N^2\psi_{yy}$. The fact that the equation reduces to the normal Stern equation in case of $N = 0$ distinguishes eq. (7.1.5) from the *Stratified Stern equation* presented in Maas and Harlander (2007).

The approach using anisotropic scales brings subtle improvements. Firstly, it can be seen from table 7.1 that the scales used here match very well with a realistic situation in an equatorial basin,

L	B	D	$\varepsilon = W/U$	Time scale T
$6400\,\text{km}$	$160\,\text{km}$	$4\,\text{km}$	0.025	$\approx 20\,\text{d}$

Table 7.1: Numerical values of the scales used to derive Stern's equation.

whereas the conventional derivation is valid only on rather small zonal length scales of $L \approx 160\,\text{km}$. Next, the assumption of zonal symmetry is not necessary anymore due to the different length scales in the horizontal. Hence, ψ can still be a function of x that allows for zonal boundary conditions. In particular, it will enter the first order balance if and only if $\psi = \psi(x)$. In this way, the scope of validity of eq. (7.1.5) is extended to a very realistic setting for equatorial wave dynamics.

7.2   Solutions for an upper boundary

In the following, the focus lies on the homogenous case ($N \equiv 0$). Eq. (7.1.5) then becomes Stern's equation

$$\psi_{yy} + 2y\psi_{yz} - \left(\omega^2 - y^2\right)\psi_{zz} + \psi_z = 0, \tag{7.2.1}$$

and since the differential operator factorizes in this case, it can be written as

$$\left(\partial_y + (y+\omega)\partial_z\right)\left(\partial_y + (y-\omega)\partial_z\right)\psi = 0. \tag{7.2.2}$$

Hence, by means of the characteristic coordinates

$$\chi^{\pm} = \frac{(y \pm \omega)^2}{2} - z, \tag{7.2.3}$$

eq. (7.2.2) can be expressed using a single mixed derivative, $\partial_{\chi^+}\partial_{\chi^-}\psi = 0$. One can immediately conclude that its general solution is of the form

$$\psi = F^+(\chi^+) - F^-(\chi^-) \tag{7.2.4}$$

with $F^{\pm}$ each being again arbitrary functions of only one variable[2]. The pressure field then follows from eq. (7.1.4a)-(7.1.4d), yielding $p = i(F^+ + F^-)$, such that all fields are known now. Because of this special form, p is also called the *conjugated pressure*, and the $F^{\pm}$ are called *partial pressure*.

It seems that the only remaining task is to adapt the stream function (7.2.4) to appropriate boundary conditions. This can become however rather tedious. One reason is that, notably, the coordinates $\chi^{\pm}$ do not change under the symmetry transformation

$$y \longrightarrow \mp 2\omega - y \qquad z \longrightarrow z.$$

This just means that they have a symmetry axis at $\mp\omega$, respectively. Consequently, the composite functions $F^{\pm}(\chi^{\pm})$ are subject to *the same symmetries* as their particular coordinate, whereas no general symmetry statement can be made over the sum in eq. (7.2.4) so far.

In the characteristic coordinates, the solution eq. (7.2.4) takes a very convenient form, but in turn, surfaces with constant $z = -C$ become harder to describe. Due to the ambiguities caused by the quadratic nature of the $\chi^{\pm}$, there are no unique functions $\chi^-(\chi^+)$ that represent these surfaces. Nevertheless, boundary conditions of the type $\psi|_{z=-C} = 0$ can be handled, as they correspond to the functional equation

$$F^+\left(\chi^+(y, -C)\right) = F^-\left(\chi^-(y, -C)\right) =: F(y). \tag{7.2.5}$$

---

[2]This resembles of course eq. (6.3.2), and one can indeed change coordinates in a way that eq. (7.2.4) becomes the two-dimensional wave equation.
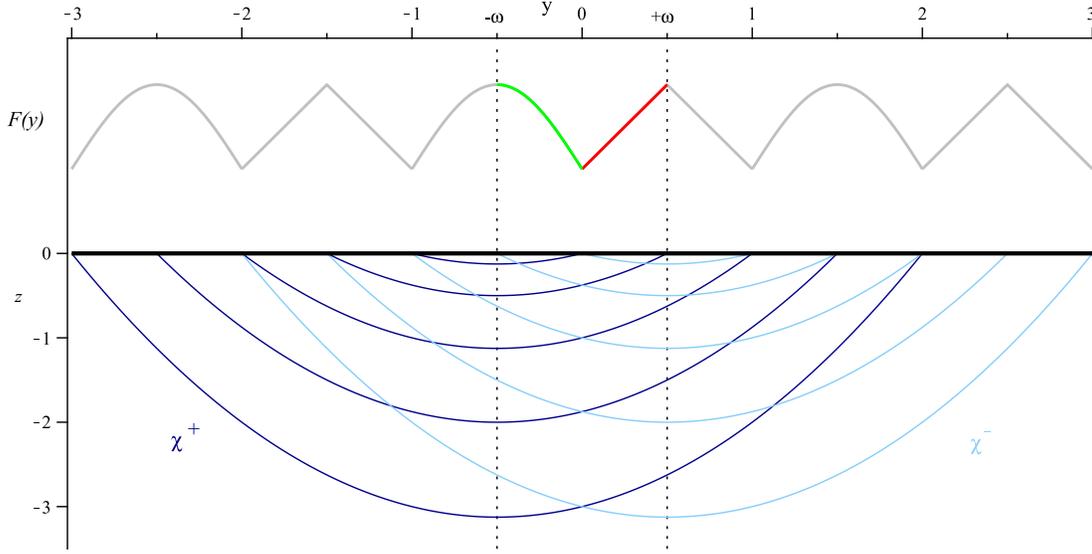
Figure 7.1: An arbitrary function $F(y)$ with two symmetry axes at $\pm\omega$ has to be periodic and only the red and green parts may be prescribed, as shown in the upper half. This function exists on the upper boundary (the thick black line) of the domain $0 \leq z < -\infty$ depicted in the lower half. As the functions $F^{\pm}$ are constant along their corresponding (symmetric) coordinate lines $\chi^{\pm}$, $F(y)$ completely determines the stream function ψ beneath the boundary. Here, $\omega = \frac{1}{2}$.

This means that a function $F(y)$ exists that represents the values of the $F^{\pm}$ at the boundary and at the same time fixes all values of ψ *below* this boundary, since all coordinate lines coming from below will intersect with this surface. In contrast, $F(y)$ does not fix the stream function in the whole domain *above* this horizontal boundary since not all coordinate lines in this upper domain intersect the boundary.

Moreover, as the functions $F^{\pm}$ are symmetric around $\mp\omega$, respectively, $F(y)$ must obey *both* symmetries. It immediately follows that $F(y)$ must be $4\omega-$periodic, additionally to the two symmetry axes it has to obey. *Regular* solutions having this properties can thus be expressed as an infinite series of sine functions,

$$F(y) = \sum_{0}^{+\infty} a_n \sin\left(\frac{2n+1}{2\omega}\pi y\right). \tag{7.2.6}$$

An upper boundary at $z = 0$ (corresponding to $C = 0$) will be considered in the following. The situation is depicted schematically in figure 7.1, where only the (preimages of the) red and green parts can be prescribed. Figure 7.2, depicting the situation in the $\chi^{\pm}-$plane, illustrates that this setting corresponds roughly to the equatorial region of a sphere filled with fluid, if one remembers the fact that the curvature terms are absent mainly due to linearization in $\vec{u}$.

The striking consequence is that it suffices to prescribe $F(y)$ between $-\omega$ and $+\omega$ in order to fix ψ for all $z < -C$, and thus in the whole domain. To put things into practice, two piecewise defined maps are introduced,

$$
\begin{aligned}
B^{+} &= \begin{cases} -\omega + \sqrt{(y+\omega)^2 - 2z}, & y \geq -\omega \\ -\omega - \sqrt{(y+\omega)^2 - 2z}, & y < -\omega \end{cases} \quad \text{and} \tag{7.2.7} \\
B^{-} &= \begin{cases} \omega + \sqrt{(y-\omega)^2 - 2z}, & y \geq \omega \\ \omega - \sqrt{(y-\omega)^2 - 2z}, & y < \omega. \end{cases}
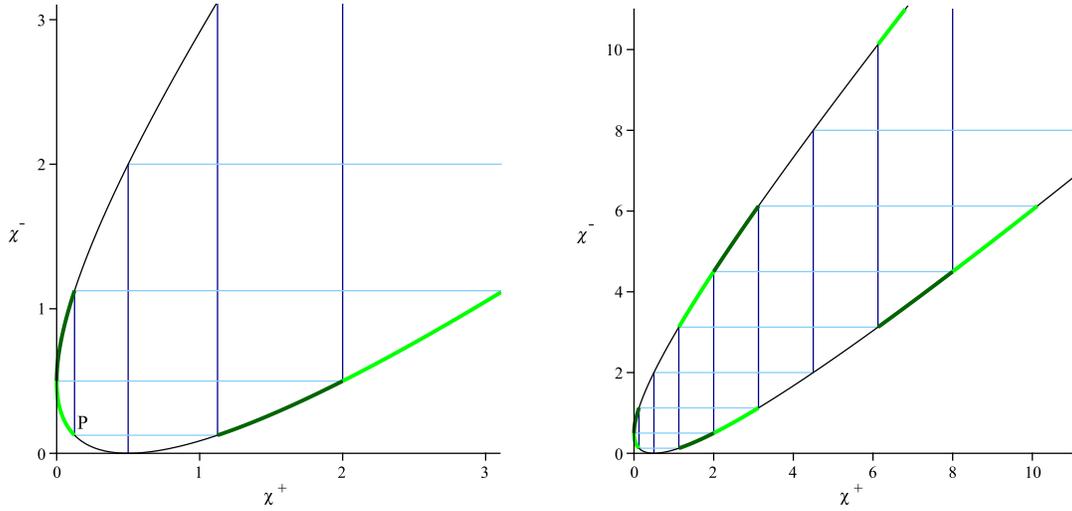\end{aligned}
$$

Figure 7.2: The characteristics (blue lines) transport the values of the functions $F^\pm$ along the surface $z = 0$, which is here depicted in the $\chi^\pm-$ plane. The light green pieces correspond to the light green interval shown in figure 7.1, the dark green pieces are their mirror images, and the $P = (\frac{\omega^2}{2}, \frac{\omega^2}{2})$ in (a) corresponds to $y = 0$. The region close to the center is enlarged on the left-hand side, and again $\omega = \frac{1}{2}$.

These functions map every point (y, z) via the respective characteristic curve $\chi^\pm$ onto the corresponding $y-$value on the upper boundary. But from eq. (7.2.4), it appears that the functions $F^\pm$ remain constant along their respective coordinate line and thus can be expressed in terms of the values of $F(y)$ for the appropriate values of y. Altogether, the stream function can just be written as

$$\psi^{\mathrm{UB}} = F\left(B^+(y,z)\right) - F\left(B^-(y,z)\right), \tag{7.2.8}$$

with F of the form of eq. (7.2.6), still having arbitrary Fourier coefficients a_n (the index UB means "upper boundary").

Although, due to the absence of the lower boundary, this is not the problem one is actually interested in when looking at equatorial dynamics, it is worth noticing that the first two modes (solely $a_0 = 1$ and solely $a_1 = 1$, respectively) visualized in figure 7.3 show an intensification towards the equatorial region $y = 0$. Obviously, the upper surface acts here like a parabolic lens, but with a reflection law different from Snell's more familiar law. It is pointed out in great detail in Harlander and Maas (2006) that the characteristics correspond to energy rays of internal waves, associated with the group velocity of such waves described in section 6.1.

Other kinds of boundary conditions. In fact, there are accessible boundary conditions in the $\chi^\pm-$coordinates. An example is a boundary at $\frac{y^2}{2} - z = C$, for which regular solutions are given in Maas and Harlander (2007). As in this case

$$\chi^\pm = \pm 2\omega y + \tfrac{1}{2}\omega^2 + C,$$

the bounding surface can straightforwardly be expressed in the new coordinates: it is just $\chi^- + \chi^+ = 2\omega^2 + C$, and the line corresponding to eq. (7.2.8) then immediately leads to the solution

$$\psi = F^+\left(\chi^+\right) - F^+\left(2\omega^2 + C - \chi^-\right).$$

Only F^+ remains here, being still arbitrary and allowing yet for additional conditions. Unfortunately, such boundaries do not occur in the ocean. The attentive reader might however recognize the particular
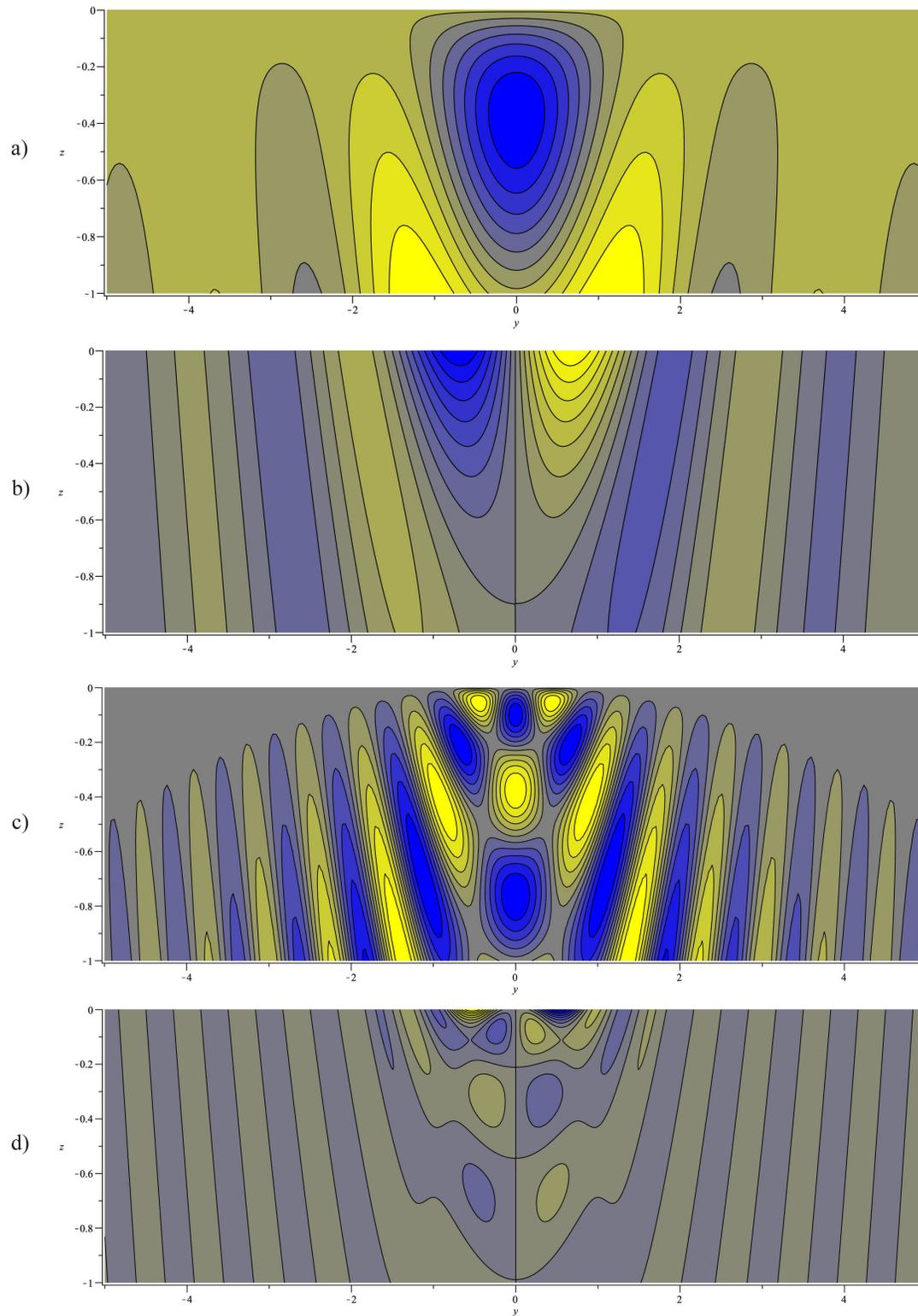
Figure 7.3: Contour plots of the solutions from eq. (7.2.8) and eq. (7.2.6) for an upper boundary only in case of $\omega = 0.5$. The stream function ψ (a) and the zonal velocity u (b) for the $n = 0$ mode as well as the stream function ψ (c) and the zonal velocity u (d) for the $n = 1$ mode are depicted. The absence of a lower boundary can be seen clearly in the stream function patterns. Remarkably, the zonal velocities have their maxima at the top whereas the other velocity components peak in the interior.

dependence on these coordinates from chapter 5, where solutions to equations that are formally similar to Stern's equation were found.

7.3 Adding a lower boundary in an infinite meridional domain

The consequential next step to refine the solutions obtained in the last section is to take a lower boundary at $z = -1$ into account, as shown in figure 7.4. The claim is that for an infinite domain in the $y-$direction, the function $F(y)$ at the upper boundary (and hence also the stream function ψ) is either not continuous in every point or constant.

This might be surprising, and the proof involves several steps. First, define the functions

$$\tilde{B}^\pm := B^\pm(y, -1)$$

that map points on the lower boundary along one of the characteristic curves $\chi^\pm$ onto points on the upper boundary, and their counterparts

$$T^+ = \begin{cases} -\omega + \sqrt{(y+\omega)^2 - 2}, & y \geq -\omega + \sqrt{2} \\ -\omega - \sqrt{(y+\omega)^2 - 2}, & y \leq -\omega - \sqrt{2} \end{cases} \text{ and } T^- = \begin{cases} \omega + \sqrt{(y-\omega)^2 - 2}, & y \geq \omega + \sqrt{2} \\ \omega - \sqrt{(y-\omega)^2 - 2}, & y \leq \omega - \sqrt{2} \end{cases}$$

that map points on the surface onto points at the bottom in the corresponding way. The latter functions are not defined between $(\mp\omega - \sqrt{2}, \mp\omega + \sqrt{2})$, where the coordinate lines do not reach the bottom. Now let $y > \max(-\omega + \sqrt{2}, \omega)$, this is possible without loss of generality due to the periodicity of F, and define the composite map

$$BT(y) := B^- \circ T^+(y) = \omega + \sqrt{\left(\sqrt{(y+\omega)^2 - 2} - 2\omega\right)^2 + 2}$$

that maps points on the upper surface back on the upper surface via a certain single "reflection" at the bottom. $BT(y)$ has the properties

$$BT(y) > y, \qquad \lim_{y \to +\infty} (BT(y) - y) = 0 \qquad \text{and} \qquad \lim_{y \to +\infty} y^2 \cdot (BT(y) - y) = 2\omega. \qquad (7.3.1)$$

From the latter property, it follows[3] that $BT(y) \sim y + \frac{2\omega}{y^2}$ for big y. The question if the successive application of BT onto itself, say $BT^k(y)$, corresponding to k reflections between top and bottom, converges against a fixed point for $k \to \infty$ or keeps growing can thus be answered by inspecting a recursively defined sequence

$$a_0 = BT^{k_0}(y), \qquad a_n = a_{n-1} + \frac{2\omega}{a_{n-1}^2} \qquad n \in \mathbb{N}.$$

It has to be shown that this sequence diverges. Indeed, one finds

$$\begin{aligned} a_n &= a_0 + (a_1 - a_0) + (a_2 - a_1) + \cdots + (a_n - a_{n-1}) \\ &= a_0 + \sum_{k=0}^{n-1} \frac{2\omega}{a_n^2} \\ &> a_0 + n \cdot \frac{2\omega}{a_n^2} \end{aligned}$$

since $a_{n_1} > a_{n_2}$ for $n_1 > n_2$. It follows that $2\omega n < a_n^2(a_n - a_0) < a_n^3$ and finally

$$a_n > (2\omega n)^{\frac{1}{3}} \to \infty \qquad \text{for} \qquad n \to \infty$$

Hence, $BT^k(y)$ always keeps growing while the distance between two reflection points at the top boundary becomes arbitrary small. Now, use the following

---

[3]Moreover, one can assure oneself that $BT(y) > y + \frac{2\omega}{y^2}$ for big y.

Definition. A function F is continuous in the point y_0, if and only if for every $\varepsilon > 0$ exists a $\delta > 0$, such that for all y with $|y - y_0| < \delta$ it holds that $|F(y) - F(y_0)| < \varepsilon$ (see for example Heuser, 1998).

Consider an arbitrary point $y_0 \in [-2\omega, +2\omega]$ on the top boundary. If F is not constant, then there exists a y_1 in the same interval with $F(y_0) \neq F(y_1)$. Now, choose ε with $\varepsilon < |F(y_0) - F(y_1)|$. According to the definition above, F can only be a continuous function in y_0 if a δ can be found, such that within distance δ of y_0, the function F does not take the value $F(y_1)$.

Next, let $\tilde{y}_1 = y_1 + 4\omega \cdot l$ with integer l, such that $\tilde{y}_1 > \max(-\omega + \sqrt{2}, \omega)$. Since $F(\tilde{y}_1) = F(y_1)$ due to the periodicity of F, one can apply $BT^k(\tilde{y}_1)$ to generate an infinite number of points where F takes the value $F(y_1)$. As it was shown above, the sequence of these points does not converge but extends to $+\infty$ while the distance between two successive points becomes arbitrarily small. Moreover, each of this points has a preimage in the interval $[-2\omega, +2\omega]$ due to periodicity.

Consequently, if there was a δ as required, one could always find a interval $[4\omega n, 4\omega(n+1)]$, $n \in \mathbb{N}$ in which the distances between successive points $BT^k(\tilde{y}_1)$ are smaller than δ and project them back to $[-2\omega, +2\omega]$. Thus, one of these points will be less than δ away from y_0. This means that for F being not constant, F cannot be continuous in *any* point, since y_0 was arbitrary.

Interpretation. Comparing the setting investigated here to the trapezoid problem of Maas et al. (1997) presented in section 6.3, one major difference is that the reflection points at the upper surface do *not* converge. As the symmetry conclusions at the beginning of this section were made for arbitrary horizontal boundaries, the new condition $\psi|_{z=-1} = 0$ implies the existence of another periodic function $\tilde{F}(\tilde{y})$ at the bottom. Seemingly, this double periodicity is incompatible with the parabolic nature of the characteristics on an infinite domain. Or, in a reference frame analogous to figure 7.2 where the characteristics are straight lines and the boundaries are curved, the domain appears to be not convex anymore in mathematical terms.

However, this result is still rather theoretical, as y in fact is bounded in reality for at least four reasons:

1. Remember that y represents a redefined and rescaled coordinate for the latitude. It is thus bounded by a $y_{\max}$ that is of $\mathcal{O}\left(\frac{\pi}{2B}r_0\right) < 10^3$.

2. The usage of the $\beta-$plane approximation again restricts the reasonable range of y to the area around the Equator where this approximation is valid.

3. In the real ocean, stratification is present and causes turning latitudes that constitute another limiting surface, see section 6.1.

4. Finally, there are continental boundaries in the real ocean.

Nevertheless, it illustrates a general phenomenon that renders the problem more difficult even in a meridionally bounded domain. Apparently, surprising feedback and constraints may emerge from symmetry conditions and through the non-convex shape of the domain.

7.4 Frictional bottom boundary layer solutions

The results of the previous section suggest that it might be at least difficult to find regular solutions to the Stern equation between two boundaries even in a finite meridional domain. This motivates an investigation whether it is possible to close the solutions obtained in section 7.2 by means of a viscous bottom boundary layer. Boundary layers are particular applications of the method of matched asymptotic expansions, see Chorin (1992), and they became a standard technique in fluid dynamics.

The most prominent examples in oceanography are the Ekman layers for the geostrophic flow and the various layers used to close the Sverdrup flow, covered by introductory textbooks like the one by Dijkstra (2008). In the case under consideration, they will however provide some rather surprising
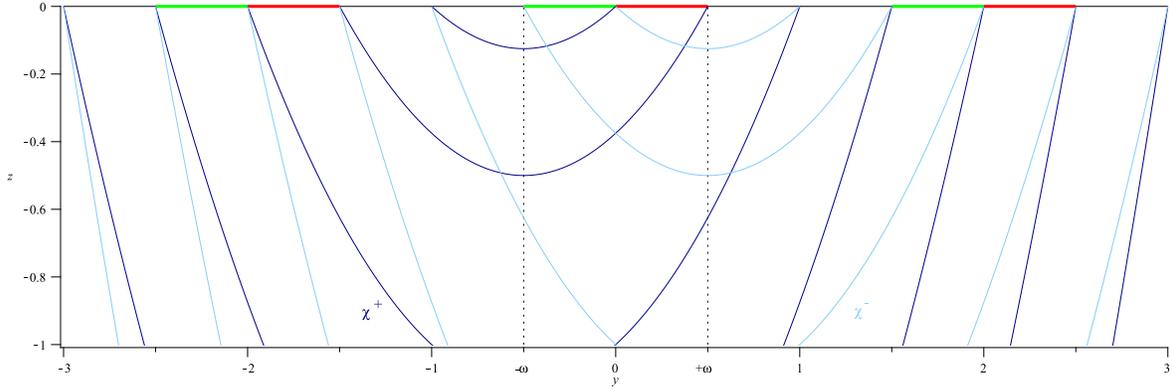
Figure 7.4: On a bottom boundary at $z = -1$, another periodic function $\tilde{F}$ has to exist. Its values are linked to the periodic function F at the upper boundary via the characteristic curves, as both F^+ and F^- are constant along these curves. In an infinite domain, the problem of finding a suitable function F is over-constrained in the sense that F (and hence also ψ) is either not continuous in every point or constant. Here, $\omega = 0.5$.

results beyond the closure of the Stern equation and two horizontal boundaries. As a first step, friction has to be included. Writing ν for the kinematic viscosity, a friction term

$$\nu \triangle \vec{u}$$

can be added to the right-hand side of the system of governing equations (7.1.1a)-(7.1.1c). This term is scaled subsequently in the same way as the other terms in each of the corresponding lines in eq. (7.1.1a)-(7.1.1e). Only two contributions remain in lowest order in $\varepsilon = \frac{B}{L} = \frac{D}{B}$ after the asymptotic expansion eq. (7.1.3),

$$\alpha \begin{pmatrix} \varepsilon^4 \hat{u}_{xx} + \varepsilon^2 \hat{u}_{yy} + \hat{u}_{zz} \\ \varepsilon^4 \hat{v}_{xx} + \varepsilon^2 \hat{v}_{yy} + \hat{v}_{zz} \\ \varepsilon^5 \hat{w}_{xx} + \varepsilon^3 \hat{w}_{yy} + \varepsilon \hat{w}_{zz} \end{pmatrix} \xrightarrow{\text{ass. exp.}} \alpha \begin{pmatrix} \hat{u}_{zz}^0 \\ \hat{v}_{zz}^0 \\ 0 \end{pmatrix},$$

where the dimensionless parameter $\alpha = \frac{\nu B}{2\Omega D^3}$ has been introduced. As typically $\nu = \mathcal{O}(10^{-6} \frac{\text{m}^2}{\text{s}})$ for sea water, $\alpha = \mathcal{O}(10^{-8})$ for the scales under consideration. Still, the case $N \equiv 0$ is investigated. Working the two new terms in the equation for ψ, an additional term that accounts for the friction appears in comparison to the Stern equation (7.2.1). The result reads

$$\psi_{yy} + 2y\psi_{yz} - \left(\omega^2 - y^2\right)\psi_{zz} + \psi_z - \alpha^2 \psi_{zzzzzz} = 0. \tag{7.4.1}$$

So far, we have won nothing as this equation is still not solvable in a direct manner. The key assumption is now that inviscous Stern equation (7.2.1) governs the dynamics nearly in the whole domain, and that the friction term becomes important in a thin boundary layer above the bottom only, motivating the ansatz

$$\psi = \psi^{\text{UB}}(y, z) + \psi^{\text{BL}}(y, \zeta) \tag{7.4.2}$$

for the stream function. Here, ψ^{UB} is the inviscous *outer* solution from eq. (7.2.8) that already satisfies the upper boundary condition. The *inner* boundary layer solution ψ^{BL} shall depend on the rescaled vertical coordinate $\zeta = \frac{z+1}{l}$, where the small length scale l is a priori unknown. It is thus assumed that the variations of ψ^{UB} on the length scale of ζ are small. The inner solution has to obey the boundary conditions

$$\psi^{\text{BL}}\big|_{\zeta=0} = -\psi^{\text{UB}}\big|_{z=-1} \qquad \text{and} \qquad \lim_{\zeta \to +\infty} \psi^{\text{BL}} = 0. \tag{7.4.3}$$

Plugging the ansatz (7.4.2) in eq. (7.4.1), using the fact that solves eq. (7.2.1) and transforming the respective derivatives yields

$$l^2\psi_{yy}^{\text{BL}} + 2yl\psi_{y\zeta}^{\text{BL}} - \left(\omega^2 - y^2\right)\psi_{\zeta\zeta}^{\text{BL}} + l\psi_{\zeta}^{\text{BL}} - \alpha^2\psi_{zzzzzz}^{\text{UB}} - \frac{\alpha^2}{l^4}\psi_{\zeta\zeta\zeta\zeta}^{\text{BL}} = 0.$$

With the choice $l^4 = \alpha^2$, the boundary layer length scale is indeed small, $l = \mathcal{O}(10^{-4})$. The resulting lowest order equation in l is

$$(\omega^2 - y^2)\psi_{\zeta\zeta}^{\text{BL}} + \psi_{\zeta\zeta\zeta\zeta}^{\text{BL}} = 0, \tag{7.4.4}$$

which apparently has a singularity at $y = \pm\omega$. It can be integrated twice to yield

$$(\omega^2 - y^2)\psi^{\text{BL}} + \psi_{\zeta\zeta\zeta}^{\text{BL}} = C_1\zeta + C_2. \tag{7.4.5}$$

The solution to eq. (7.4.5) can be obtained from the solution $\psi_{\text{H}}^{\text{BL}}$ of the corresponding homogenous equation according to $\psi^{\text{BL}} = \psi_{\text{H}}^{\text{BL}} + C_1\zeta + C_2$. Using the ansatz $e^{\lambda\zeta}$, the characteristic equation of the homogenous equation has the four roots

$$\lambda = \begin{cases} \pm\frac{1}{\sqrt{2}}(1 \pm i)\sqrt[4]{\omega^2 - y^2}, & |y| < |\omega| \\ i^n\sqrt[4]{y^2 - \omega^2}, \quad n \in \{0, 1, 2, 3\} & |y| > |\omega| \end{cases}$$

Of course, only those roots can be accepted that meet the asymptotic boundary condition in eq. (7.4.3), which moreover implies that $C_1 = C_2 = 0$. The real part of the boundary layer stream function reads then

$$\psi^{\text{BL}} = \begin{cases} C^< e^{-\frac{1}{\sqrt{2}}\sqrt[4]{\omega^2 - y^2}\,\zeta} \cos\left(\frac{1}{\sqrt{2}}\sqrt[4]{\omega^2 - y^2}\,\zeta + \phi\right), & |y| < |\omega| \\ C^> e^{-\sqrt[4]{y^2 - \omega^2}\,\zeta}, & |y| > |\omega| \end{cases}$$

The phase $\phi \neq (\mathbb{Z} + \frac{1}{2})\pi$ is taken to be zero in the following, facilitating the constants. Its physical implication is not yet clear. If $\lim_{y\downarrow|\omega|}\psi^{\text{BL}} = \lim_{y\uparrow|\omega|}\psi^{\text{BL}}$ is demanded, it follows for the constants $C^{\lessgtr}$ that $C^< = C^>$. Applying lastly the boundary condition on the left-hand side in eq. (7.4.3) that connects inner and outer solutions, the complete stream function is

$$\psi(y, z) = \psi^{\text{UB}}(y, z) + \psi^{\text{UB}}(y, -1) \cdot \Delta(y, \zeta), \tag{7.4.6}$$

where the decay of the boundary layer amplitude is represented by the function

$$\Delta(y, \zeta) = \begin{cases} e^{-\frac{1}{\sqrt{2}}\sqrt[4]{\omega^2 - y^2}\,\zeta} \cos\left(\frac{1}{\sqrt{2}}\sqrt[4]{\omega^2 - y^2}\,\zeta + \phi\right), & |y| < |\omega| \\ e^{-\sqrt[4]{y^2 - \omega^2}\,\zeta}, & |y| > |\omega|. \end{cases} \tag{7.4.7}$$

The inviscous outer solution ψ^{UB} was derived in section 7.2, it has the structure

$$\psi^{\text{UB}} = F\left(B^+(y, z)\right) - F\left(B^-(y, z)\right), \qquad \text{where } F(X) = \sum_{0}^{+\infty} a_n \sin\left(\frac{2n+1}{2\omega}\pi X\right) \tag{7.4.8}$$

and the two piecewise defined maps $B^\pm$ are given by eq. (7.2.7). It should be stressed that the undetermined parameters of this solution are the amplitudes a_n *and* the phase ϕ. The latter has been chosen to be zero here, whereas for general $\phi \neq (\mathbb{Z} + \frac{1}{2})\pi$, only the rate between $C^<$ and $C^>$ will change. Its presence suggests another difference in the behavior of the boundary layer for $|y| \lessgtr |\omega|$, respectively.

Figure 7.5 shows the first two modes, which can be compared to the inviscid stream function in figure 7.3. The boundary condition at the bottom is clearly satisfied, but in return, the modes show discontinuous behavior around $y = \pm\omega$. This can be also seen from eq. (7.4.7), where Δ basically
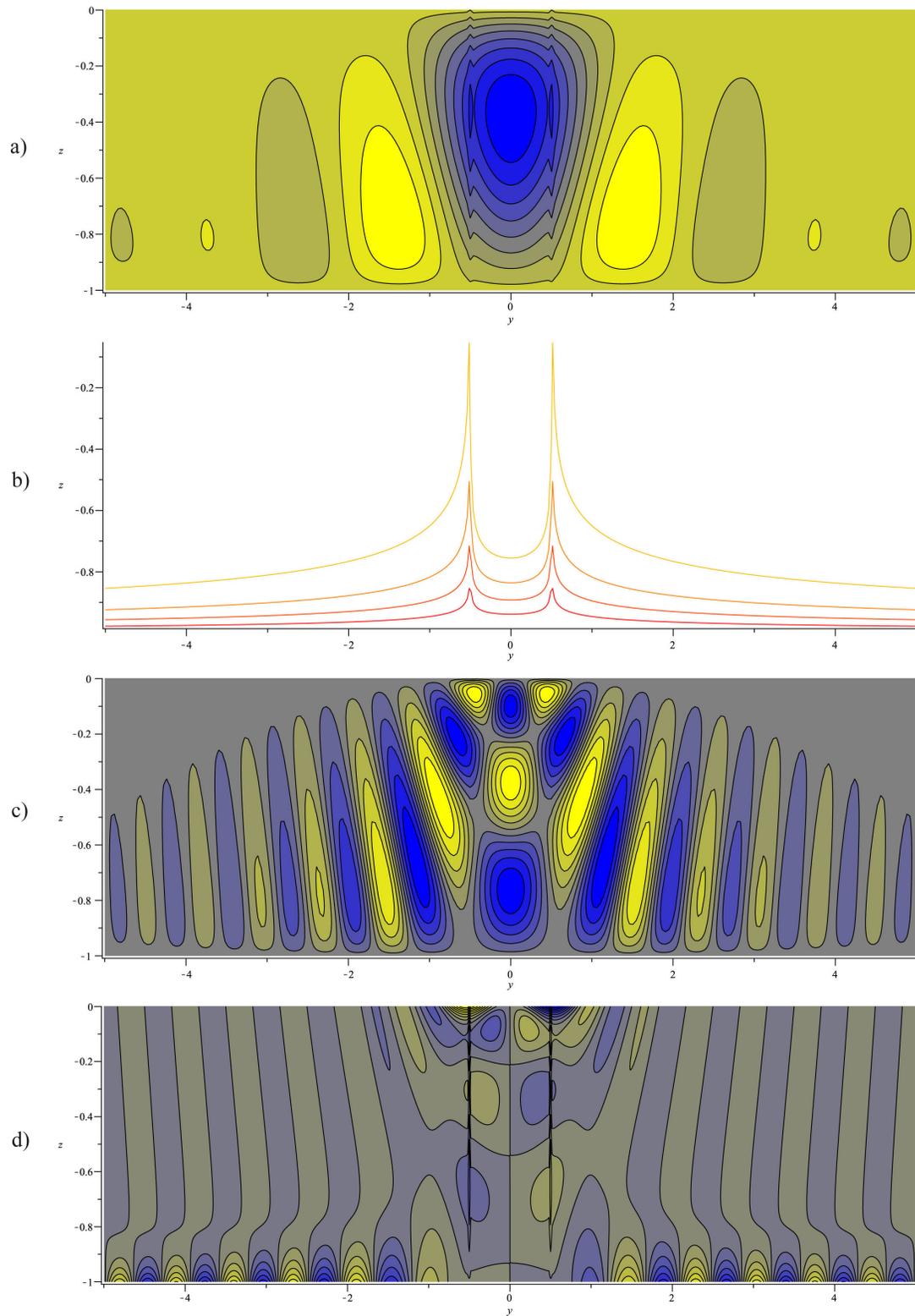
Figure 7.5: Contour plots of the solutions from eq. (7.4.6) for a frictional bottom boundary layer in case of $\omega = 0.5$, compare figure 7.3 for the solutions without boundary layer. (a) Stream function ψ for the $n = 0$ mode. (b) The boundary layer function Δ, showing singularities at $y = \pm\omega$. (c) Stream function ψ and (d) zonal velocity u for the $n = 1$ mode. The singularities at $y = \pm\omega$ can be seen clearly in (a) and (d). In (c), they are not visible with the naked eye due to the grid resolution.

determines the decay of the boundary layer for $\zeta \to \infty$. The length scale $\Lambda(y)$ for this decay is supposed to be at most $\mathcal{O}(1)$ with respect to ζ to maintain the assumptions underlying boundary layer theory. Eq. (7.4.7) however states that

$$\Lambda \propto \frac{1}{\sqrt[4]{|y^2 - \omega^2|}} \qquad \text{and thus} \qquad \lim_{|y| \to |\omega|} \Lambda = \infty.$$

In other words, the boundary layer blows up around the *traditional critical latitudes*, as $y = \pm\omega$ is just the dimensionless version of eq. (6.1.8), leading there to singularities in the velocity fields. This is shown explicitly in figure 7.5b. It is in a way surprising that such singularities appear in the viscous boundary layer theory pursued here, especially as they are found at the same location as the singularities described by Stewartson and Rickard (1969) in their inviscid approach that was discussed in section 6.2. We are thus facing the same question as Stewartson and Rickard (1969), namely whether these singularities and discontinuities indicate a real physical effect like flow separation or whether they are just a consequence of the coordinates and/or the approximation method[4].

In case of a filled sphere, viscous boundary layers that blow up at the traditional critical latitudes were however described by Roberts and Stewartson (1963). Noir et al. (2001) succeeded to observe the generation of internal wave cones at these locations in a forced precessing spheroid. From this point of view, it seems likely that the discontinuities found here in theory for a spherical shell also exist in reality. In particular, as forcing through libration or precession is transferred to the fluid in the bottom boundary layer, the internal wave disturbances likewise should enter the interior of the fluid domain at the traditional critical latitudes, where the boundary layer blows up.

By means of numerical simulations, it will however be demonstrated in the next chapter that in a completely inviscid setting, the critical latitudes may form an interior barrier that is clearly unphysical and due to a bad choice of coordinates. From this point of view, the nature of the phase ϕ still remains dubious.

Two more conceptual details should be noted. Firstly, the boundary layer approach used here allows only for free slip-boundary conditions at the bottom. This is seemingly a consequence of the numerous approximations made so far that particularly break down the full three-dimensional problem into a two-dimensional equation for a stream function. For example, the zonal velocity in figure 7.5d even reaches some of its maximum values at the sea bottom. It is an open question how these maxima translate into a fully viscous setting that includes no-slip boundary conditions. Secondly, the method presented here cannot be reversed by using an upper boundary layer instead. As mentioned in section 7.2, the presence of a *lower* boundary does not fix the stream function in the whole domain *above*. Even inviscid solutions with a modal structure comparable to eq. (7.4.8) cannot be obtained in this case.

---

[4]Stewartson and Rickard (1969) write that "[...] it is possible that the pathology we have just been describing is a creature of the particular limiting process adopted [...]".

Chapter 8

A numerical approach to equatorial wave attractors

Numerical methods are a mighty tool in fluid dynamics, as in most cases, analytical solutions cannot be found. Unfortunately, there are no standard methods for problems that are mathematically ill-posed like Stern's equation.

The aim of this chapter is to develop a numerical method that allows for a detailed and reliable description of equatorial wave attractors. The concept of such attractors emerging from Stern's equation is introduced in section 8.1. The approach put forward by Harlander and Maas (2007) is developed further in section 8.2, which will make clear its limitations and give a hint how to overcome them. This is achieved in section 8.3 by means of a new method. Parts of this new method are used to make a first attempt towards forced problems in section 8.4. Finally, conclusions and limitations are discussed. For all computations in this chapter, the software MATLAB was used.

8.1 Equatorial wave attractors

The general concept of wave attractors has been introduced in section 6.3, where it has been pointed out that for particular shapes of a domain a *sole closed* path along characteristic curves may exist. This closed path then constitutes an attractor, and all other such paths converge towards it while never reaching it. Hence, they become infinitely long and are eventually trapped along the closed trajectory. Now consider again Stern's equation

$$\left(\partial_{yy} + y^2\partial_{zz} + 2y\partial_{yz} + \partial_z\right)\psi = \omega^2\partial_{zz}\psi, \tag{8.1.1}$$

which was derived in section 7.1. Here, it is restated as a generalized eigenvalue problem for later convenience. Bretherton (1964) firstly recognized that eq. (8.1.1) together with the boundary conditions $\psi|_{z=0} = \psi|_{z=-1} = 0$ exhibits such closed paths. A modern interpretation in terms of wave attractors was given by Maas and Harlander (2007).

One can see the analogy to section 6.3 better upon introducing new variables according to

$$Y = 4y \qquad \text{and} \qquad Z = 2(2z - y^2). \tag{8.1.2}$$

Then, eq. (8.1.1) transforms into the spatial wave equation

$$\psi_{YY} - \omega^2\psi_{ZZ} = 0, \tag{8.1.3}$$

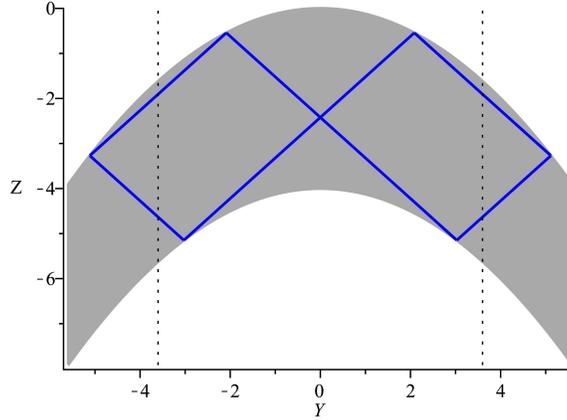that resembles eq. (6.3.1) and will be abbreviated as *SWE* from now on. Bottom and top of the basin

Figure 8.1: For $\omega = 0.9$, a closed path along characteristic curves/energy rays is constructed geometrically. It is unique for this frequency and constitutes a wave attractor. The parabolically shaped basin representing the equatorial ocean under the β−plane approximation is colored gray, the rotation axis points in Y−direction. In the new coordinates, the traditional critical latitudes eq. (6.1.8) lie at $Y = \pm 4\omega$, they are represented by the dashed lines.

are in the new coordinates[1] represented by the parabolas

$$Z_{\text{bottom}}(Y) = -\frac{Y^2}{8} - 4 \qquad \text{and} \qquad Z_{\text{top}}(Y) = -\frac{Y^2}{8}, \tag{8.1.4}$$

whereas the characteristic curves eq. (7.2.3) simply become straight lines

$$\chi^{\pm} = \omega Y \pm Z. \tag{8.1.5}$$

In this coordinate frame, it becomes apparent that the parabolas eq. (8.1.4) represent the curvature of the Earth in the β−plane approximation. Like it was the case for the inertial waves presented in section 6.1, the inclination with respect to the rotation axis of the lines eq. (8.1.5) depends on the frequency. Indeed, they represent energy rays traveling in parallel to the group velocity of such waves, as pointed out in detail by Harlander and Maas (2006).

   Figure 8.1 shows a geometrically constructed closed ray path which turns out to be unique for that particular frequency and forms a wave attractor. In the appendix of Harlander and Maas (2007), it is demonstrated in great detail how the principle of fundamental intervals mentioned in section 6.3 can be transferred in a clever way to such equatorial wave attractors. However, this method considers mainly the region enclosing the attractor. Hence, it might not catch some phenomena due to the periodicity of the partial pressure along the boundaries derived in section 7.2 that also underlie the problems with continuity described in section 7.3. Numerical approaches to the problem seem thus advantageous and very objective, as they do not require any assumptions on the nature of the solutions.

8.2   Eigenfunctions of Stern's equation

In a first approach, Stern's equation is treated directly as generalized eigenvalue problem according to eq. (8.1.1). The appropriate eigenvalues and eigenvectors (i.e. eigenfunctions) are determined numerically by means of the *method of finite differences*. Details on this method can be found in many books on numerical mathematics, like the one by Quarteroni et al. (2000).

---

[1] In order to enable easy comparison, *all* results in this chapter will be presented and printed in these new coordinates, regardless whether they were obtained in the (y, z)−frame or in the (Y, Z)−frame.
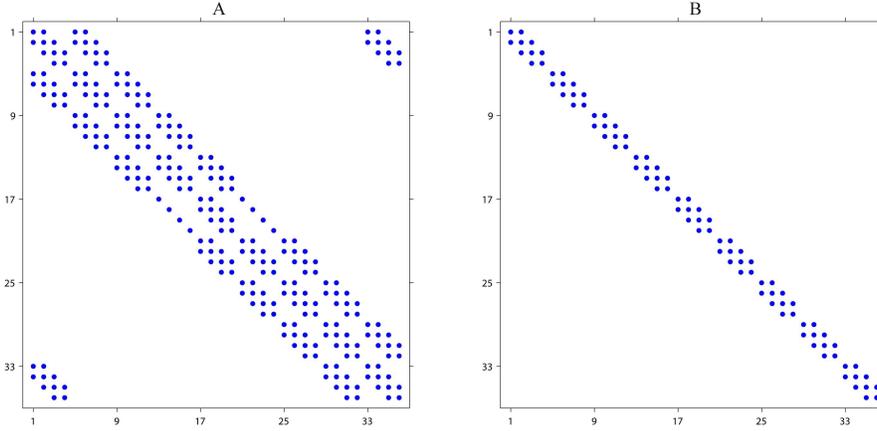
Figure 8.2: For a small $(4 \times 9)-$grid, the sparse $(36 \times 36)-$matrices A (left) and B (right) are shown that represent the differential operators according to eq. (8.2.1). Most of the entries are zero (white areas), which makes it advantageous to save and process only the nonzero entries (blue dots). Then, much larger grids containing about 10^6 points can be used.

A discrete $(k \times j)$-grid is introduced on the $y - z-$plane, where the indices $k = 1 \cdots N_z$ and $j = 1 \cdots N_y$ describe the vertical and horizontal position, respectively. Moreover, let h_y and h_z be the resulting grid spacing in terms of y and z. The differential operators are replaced by *central differences*:

$$\psi_{yy} \to \frac{\psi_{k,j+1} - 2\psi_{k,j} + \psi_{k,j-1}}{h_y^2} \qquad \psi_{zz} \to \frac{\psi_{k+1,j} - 2\psi_{k,j} + \psi_{k+1,j}}{h_z^2}$$

$$\psi_z \to \frac{\psi_{k+1,j} - \psi_{k-1,j}}{2h_z} \qquad \psi_{yz} \to \frac{\psi_{k+1,j+1} - \psi_{k+1,j-1} - \psi_{k-1,j+1} + \psi_{k-1,j-1}}{4h_y h_z}$$

The next step is to bring the grid points into *lexicographical order*, such that a single index characterizes the grid points uniquely[2]. Let N_z be the number of rows, then this index reads

$$n = (j - 1) \cdot N_z + k,$$

where $n = 1 \cdots N$ and $N = N_z \cdot N_y$. In this indexing, the stream function ψ is represented by a vector $\vec{\psi}$ with N entries and the differential operators become $(N \times N)-$matrices. Denominating

$$\partial_{yy} + y^2 \partial_{zz} + 2y\partial_{yz} + \partial_z \to A \qquad \text{and} \qquad \partial_{zz} \to B,$$

the discrete version of the generalized eigenvalue problem eq. (8.1.1) reads

$$A\vec{\psi} = \omega^2 B\vec{\psi}. \tag{8.2.1}$$

Appropriate boundary conditions have to be implemented in the matrices A and B, too. For a finite domain in $y-$direction, both periodic and vanishing boundary conditions are possible. In reality, the influence of these boundary conditions on the results proved to be negligible as long as the meridional extent of the domain is large enough. In the results presented in the following, periodic boundary conditions were used as they appear to be more objective by not possibly presuming trapping effects.

Harlander and Maas (2007) presented first attempts to solve eq. (8.2.1) numerically in this way. The computational effort for finding all eigenvalues and eigenvectors is however high. In particular, the

---

[2]More details on lattices and data structures, but in the context of statistical physics, can be found in the book by Newman and Barkema (1999).
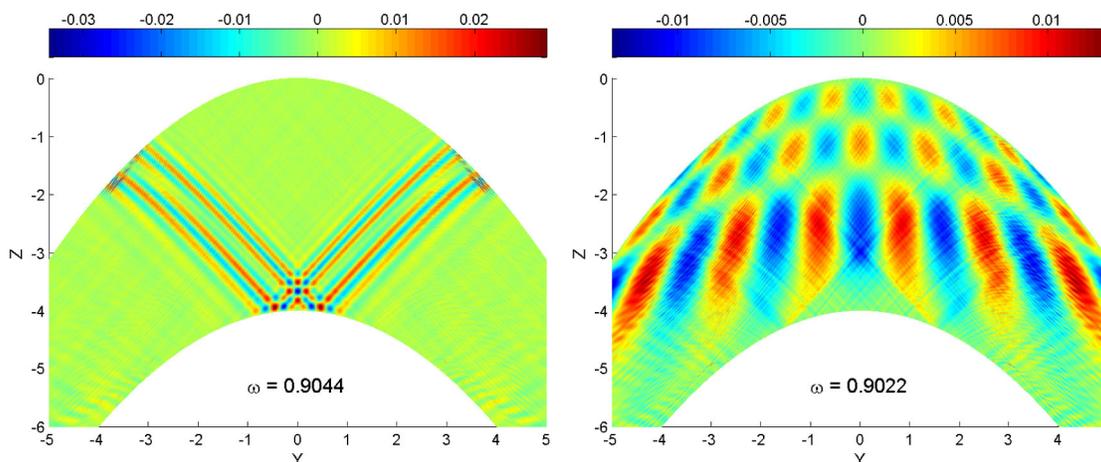
Figure 8.3: Details (central parts) of two selected eigenfunctions of Stern's equation (8.2.1) are plotted in the $Y - Z$−frame. A (201×1001)- grid that represents the domain $|Y| \leq 20$ was used to look for eigenfunctions around $\overline{\omega} = 0.9$. While resembling the solution constructed geometrically by Maas and Harlander (2007) and the boundary layer solutions presented in section 7.4, respectively, the match is not exact in both cases.

size of the matrices A and B corresponds to the *squared* number of grid points N^2. Both the memory and the CPU speed available on a well-equipped PC then restrict the grid size to about 10^3 points. The resulting low resolution makes the assessment of results very difficult.

In this work, a major improvement in resolution is achieved by utilizing the fact that most entries of the matrices A and B are zero, see figure 8.2. MATLAB provides a special data format for these *sparse matrices* which reduces the memory needed considerably. The routine **sptarn** from the MATLAB PDE toolbox finally is used to solve the problem eq. (8.2.1) for a given interval of the spectrum. It is optimized for sparse matrices and based on an Arnoldi iteration. For further details, the reader may refer to the example code given in the appendix A.3 and to the MATLAB documentation.

The fact that **sptarn** scans only a part of the spectrum for its eigenfunctions is another benefit, as then by narrowing this interval, also the computational effort can be lowered. Anyway, closed ray paths of a certain shape will exist only in a certain frequency range.

Resulting stream function patterns. The method described so far indeed allows to raise the number of grid points considerably to $N = \mathcal{O}(10^6)$ and should therefore yield clear and sharp pictures of ψ. Multiple scans around a center frequency[3] $\overline{\omega} = 0.9$, for which the closed ray path of figure 8.1 exists, were performed while varying the parameters like particularly the meridional size of the simulated domain. In contrast to what was expected, about 99% of all eigenfunctions obtained in this way show strong discontinuities, noise and unexpected irregular small-scale patterns that render their physical significance highly doubtful.

In figure 8.3, two well-behaving examples out of the remaining 1% are depicted. Notably, the function shown on the left-hand side of figure 8.3 resembles the geometrically constructed solution in figure 2 of Maas and Harlander (2007), whereas the function depicted on the right-hand side resembles the boundary layer solutions presented in section 7.4. But a closer look quickly reveals that in both cases, the match is far from exact.

The problem becomes more evident by looking at frequencies around $\overline{\omega} = 0.52$, for which another closed ray path can occur according to Maas and Harlander (2007). Several runs were performed for different settings and again, noise and distortion were dominating but many eigenfunctions clearly

---

[3]Like in section 7.1, the frequency scale is $\frac{\omega}{2\Omega} = \frac{D}{B} \approx \frac{1}{40}$.
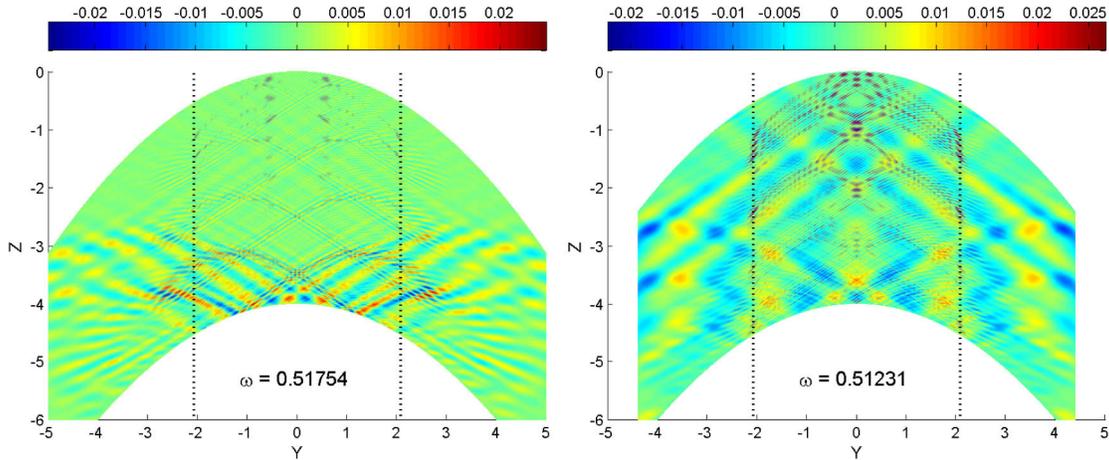
Figure 8.4: Two exemplary eigenfunctions of Stern's equation (8.2.1) for frequencies around $\overline{\omega} = 0.52$ are plotted in the $Y - Z-$frame. The simulated domain was $|Y| \leq 5.6$ (left) and $|Y| \leq 4.4$ (right), respectively. Ray patterns can be seen clearly, but surprisingly, they are reflected partly at the critical latitudes $Y = \pm 4\omega$ (dotted lines). The distortions showing up in both pictures are symptomatic for this approach.
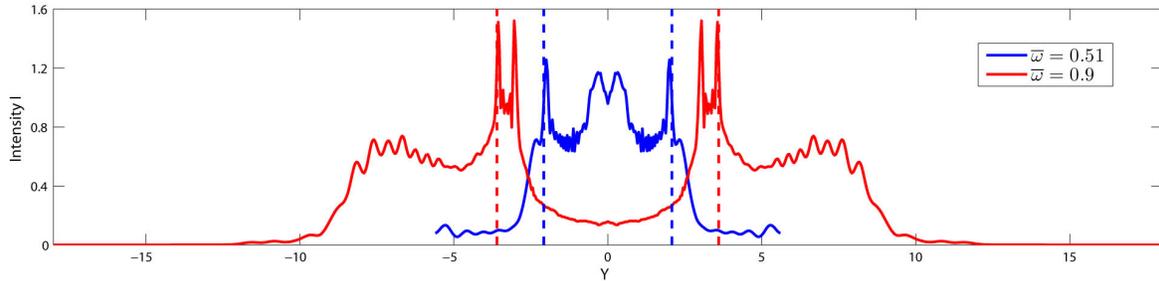

Figure 8.5: The quantity I from eq. (8.2.2) is plotted for numerical solutions of Stern's equation in the intervals $\omega = 0.90 \pm 0.005$ and $\omega = 0.51 \pm 0.01$. The curves are normalized to fit the figure. There are strong peaks at the critical latitudes $\pm 4\omega$ (dashed lines), and the stream function decays significantly far beyond the critical latitudes.

exhibit ray-like structures. Surprisingly, these rays turn out to reflect partly at the critical latitudes $Y = \pm 4\omega$, where no physical barrier is present, rather than at the real boundaries in order to coincide with the predicted shape. In this respect, figure 8.4 shows two typical patterns while no attractor structures could be observed at all.

The concept of turning surfaces was introduced in section 6.1. For the Stern equation, no turning surfaces should be found as it describes a nontraditional homogenous setting and hence is covered by eq. (6.1.6) for $N \to 0$. However, the method used here establishes traditional turning surfaces like those described by eq. (6.1.8), which is the wrong behavior. The numerical results presented so far therefore have to be dismissed in the light of internal wave theory.

Equatorial trapping.   Despite the shortcomings found in the numerical solutions to Stern's equation, it is very instructive to examine whether these solutions show effects of equatorial trapping. This requires to explore first how the infinite degenerate and continuous spectrum that is characteristic for internal waves translates to a discrete system. From an inspection of the numerical eigenvalues it is found that the spectrum is non-degenerate and discrete. The eigenvalues lie however closely together
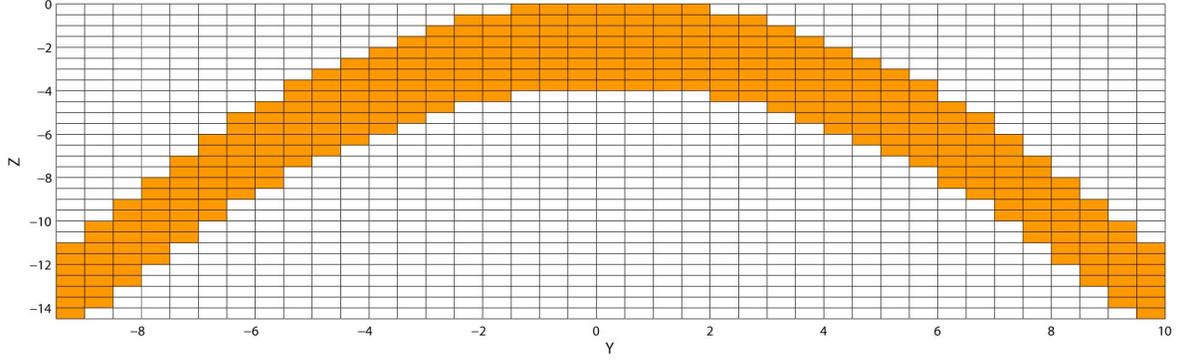
Figure 8.6: The stream function in a discretized $Y - Z-$frame is nonzero only in the small orange colored domain described by eq. (8.1.4). Processing the vector $\vec{\psi}$ over the whole domain leads to nearly singular matrices and wastes computer power. It is thus better to build up $\vec{\psi}$ by concatenating the orange columns directly in order to solve the SWE numerically, see text.

within the full precision available.

An empiric quantity can be introduced by integrating the squared eigenfunctions over a small part of the spectrum and over the vertical coordinate, reading thus

$$I(y) = \int\limits_{-1}^{0} \int\limits_{\overline{\omega}-\epsilon}^{\overline{\omega}+\epsilon} |\psi_\omega(y, z)|^2 \, d\omega \, dz. \tag{8.2.2}$$

This quantity will be called an intensity due to its quadratic nature, and it should catch at least basic tendencies of the meridional distribution of the stream function. The integrals are replaced by sums in the discrete case, and typically, the small parameter $\epsilon = \mathcal{O}(10^{-2}\overline{\omega})$.

In figure 8.5, the outcome of this procedure is plotted for the two central frequencies discussed so far. An extreme equatorial intensification as well as strong spikes at the critical latitudes can be observed. However, taking into account the shady provenience of the eigenfunctions processed, these effects are mainly due to the unphysical reflections and distortions revealed in the last paragraph. The bottom line is thus that trapping effects also can arise from inaccurate numerical methods, which makes a close look at the used method indispensable for a proper assessment of such results.

8.3 Eigenfunctions of the SWE in a curvilinear domain

The only hint that Stern's equation (8.1.1) may develop the unexpected reflections found in the previous chapter is the term $(y^2 - \omega^2)\psi_{zz}$, which vanishes at the critical latitudes. Since this term can be removed by switching to the $Y - Z-$frame and considering the spatial wave equation instead, an improper choice of coordinates might cause these problems. It appears thus promising to solve the generalized eigenvalue problem

$$\partial_{YY}\psi = \omega^2 \partial_{ZZ}\psi$$

directly in the curvilinear geometry described by eq. (8.1.4).

Figure 8.6 illustrates the main challenge with this approach: the stream function ψ is zero in the major part of the domain, leading to nearly singular matrices that cause numerical problems. In addition, the maximum resolution available in the nonzero areas decreases due to a waste of computer power. By creating the vector $\vec{\psi}$ only from the nonzero parts of the domain, these problems can be overcome at the expense of a more challenging programming. Keeping track of the vertical offset between neighboring columns of nonzero points (orange colored columns in figure 8.6), the matrices

representing the differential operators have to be determined point by point. Now, bottom and top boundary conditions have a bearing also on the $Y-$direction since not every point in a column has a left and a right neighbor.
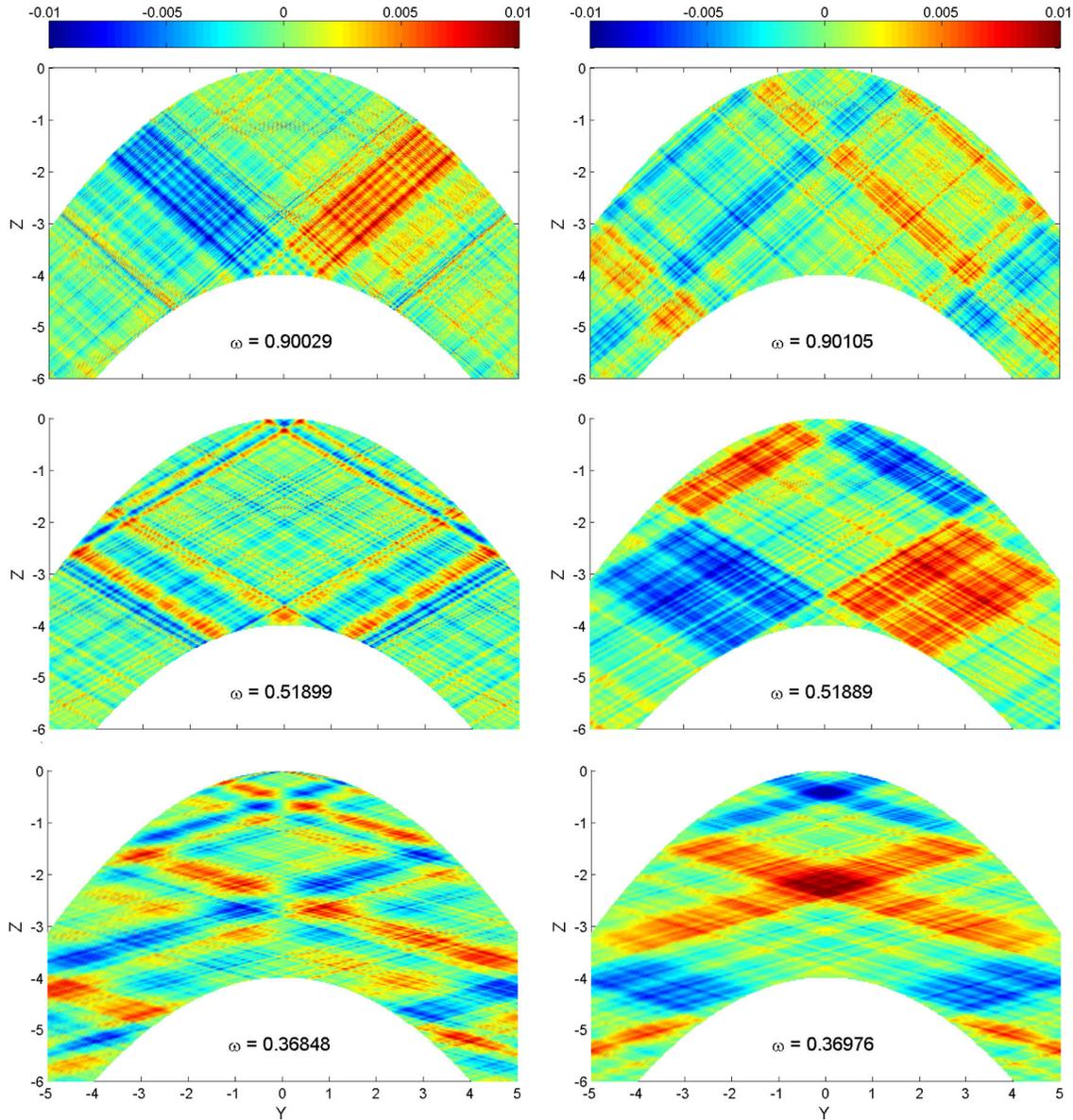
Figure 8.7: Details (central part) of representative eigenfunctions of the spatial wave equation (8.1.3) from three different scans around $\overline{\omega} = 0.9$, $\overline{\omega} = 0.52$ and $\overline{\omega} = 0.37$. All of them match very well with the solutions constructed geometrically by Harlander and Maas (2007). Suspect distortions and reflections in the interior observed in section 8.2 are absent in *all* eigenfunctions obtained with this method. The detailed settings can be found in table A.2.

The remainder of the programming is then quite similar to the previous method. An exemplary MATLAB code together with the settings used to produce the figures in this section can be found in the appendix A.4.
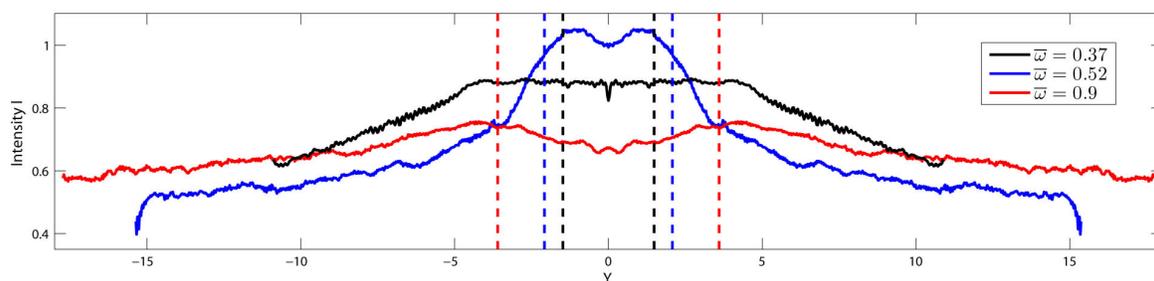
Figure 8.8: The quantity I from eq. (8.2.2) is evaluated for the spatial wave equation, again the curves are normalized to fit the figure. An intensification of the wave action towards the equatorial area can be seen clearly, whereas the decay away from the Equator is much slower in comparison to figure 8.5. The dashed lines mark the critical latitudes.

Enhanced stream function patterns. Similar to what was done in the previous section, small frequency bands were scanned for eigenfunctions at a high spatial resolution. Some selected but typical results for the center frequencies $\overline{\omega} = 0.9$, $\overline{\omega} = 0.52$ and $\overline{\omega} = 0.37$ are shown in figure 8.7. All three frequencies exhibit closed ray paths, and the corresponding attractor solutions were constructed geometrically by Harlander and Maas (2007) by means of the fundamental interval method. The results found here are clearly in line with their patterns, and it is stressed again that they are purely numerical and do not require any presumptions. Hence, one may regard them as an independent verification.

Notably, two different types of stream function patterns emerge, namely modes that are localized around the Equator and modes that extend over the whole domain. The latter ones can be identified in figure 8.7 through rays that leave the central area. Contrary to what was found in the previous section, neither unaccountable reflections at the critical latitudes nor discontinuous distortions occur. This confirms the conjecture that these were actually symptoms of an inaccurate choice of coordinates.

It is however observed that the patterns are slightly but uniformly blurred or overlain by noise. In other words, the resolution appears to be lower than expected for the chosen settings (details can be found in table A.2). On the one hand, these observations could be caused by the fine structures typically associated with wave attractors, a very interesting topic covered by Harlander and Maas (2007). On the other hand, by interpreting them as discontinuities that are spread uniformly in space, they could be a weaker manifestation of the feedback effects described in section 7.3 in case of a finite domain. Discontinuities are a general phenomenon coming along with hyperbolic ill-posed problems, as pointed out for example in the book by Quarteroni et al. (2000).

Lastly, it should be mentioned that even the point attractors described briefly in section 6.3 occasionally formed at the outer boundaries of the domain, but those outer boundaries are of course artificial.

Trapping strength. The discrete version of the intensity eq. (8.2.2) can be evaluated for the SWE, too, and figure 8.8 shows the outcome for the three center frequencies under consideration. The curves are smooth in comparison to figure 8.5, and there are no longer peaks at the critical latitudes. An equatorial intensification is clearly present while less pronounced. The artificial point attractors just mentioned could cause corruption in the off-equatorial region. In this regard, the true trapping strength might be underestimated by this method.

8.4 Forced modes

Even though the generalized eigenvalue problem eq. (8.1.1) could be tackled successfully in the previous section, this is a rather theoretical result so far. It gains only significance by investigating the corresponding forced problem, which emerges upon adding a term $\vec{f} = e^{i\omega t}(0, f^{(y)}, f^{(z)})^T$ to the right-hand
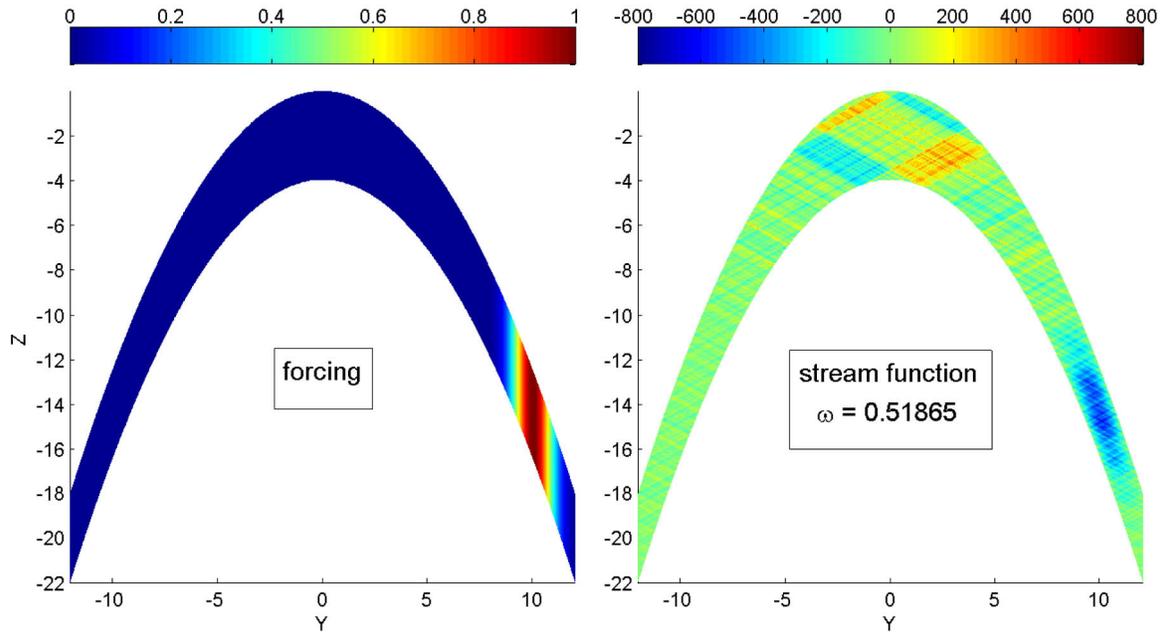
Figure 8.9: An asymmetric, off-equatorial periodic forcing (left-hand side) can excite a stream function ψ that contains an equatorial attractor (right-hand side). Here, $\mathcal{F} = e^{-(Y-10)^2}$.

side of eq. (7.1.1a)-(7.1.1c) and carry it through the whole scaling procedure of section 7.1. Here, $\vec{f}$ is a periodic body force whose zonal component is assumed to be zero for the sake of simplicity. After undergoing the coordinate transformation eq. (8.1.2), the forced spatial wave equation

$$\left(\partial_{YY} - \omega^2 \partial_{ZZ}\right)\psi = \mathcal{F} \tag{8.4.1}$$

is obtained. The dimensionless forcing term $\mathcal{F}$ turns out to be proportional to the zonal component of the vorticity vector,

$$\mathcal{F}(Y,Z) \propto \frac{i}{\omega}(f_y^{(z)} - f_z^{(y)}). \tag{8.4.2}$$

Interestingly, a phase factor of $\frac{\pi}{2}$ appears and the impact of forcing is expected to be inversely proportional to the frequency. The strongest candidate for forcing in the interior of the real ocean is by the way the tide, but it derives always from a potential. Hence, it has no curl and cannot enter eq. (8.4.1) in a direct manner. Oglivie (2005), who investigated the dissipation rate for forced attractors in a tilted square domain, however pointed out that a vortical effective forcing still may result in more realistic settings. Wind forcing, on the other hand, typically has a curl, but it is restricted to the surface.

Owing to the work already done, it is very easy to treat the forced problem as the matrices representing ∂_{YY} and ∂_{ZZ} can be taken simply from the algorithm of section 8.3. Once $\mathcal{F}$ and ω are given, eq. (8.4.1) can be solved in MATLAB directly for ψ by means of the backslash operator. Of course, the forcing term has to be brought to an appropriate vector form.

It is not surprising that the resulting stream function patterns mostly look like a superposition of the forcing and of patterns akin to the eigenfunctions from the preceding section. It is however quite remarkable that a forcing which is strongly localized *off the Equator* can excite attractor structures that are strongly localized *at the Equator*. An example for such a situation is shown in figure 8.9. The detailed conditions for this to happen are however unclear. Most likely, they are related to the values of the (partial) pressure at the boundaries. In theory, there is an infinite number of possibilities to set these values, which reflects the infinite degeneracy of internal waves. The absence of this

infinite degeneracy in a grid-based numerical model makes it hard to elucidate such questions with this approach.

8.5 Discussion

Zeros of the coefficients in a PDE can manifest themselves as virtual barriers which may reflect and distort ray patterns. For Stern's equation, it was demonstrated that these unphysical effects cause an erroneous overestimation of equatorial trapping. Hence, reports over extreme trapping observed in numerical simulations should be considered with caution. However, a suitable coordinate transformation removes the zeros in Stern's equation, leads to a more realistic trapping strength and allows a concrete interpretation in terms of internal waves in a curvilinear geometry representing the equatorial ocean.

If stratification is included like in eq. (7.1.5), no such coordinate choice exists. As a matter of fact, turning surfaces then emerge from eq. (6.1.6). The assessment of numerical results may become hard in this case, since virtual barriers due to zeros as well as physically meaningful turning surfaces may occur at the same time. One way out might be to solve eq. (7.1.5) again in the $Y - Z-$frame, where it yields the extended spatial wave equation

$$16 \left(\psi_{YY} - \omega^2 \psi_{ZZ} \right) + N^2 \left(16 \psi_{YY} + Y^2 \psi_{ZZ} - 8Y \psi_{YZ} - 4 \psi_Z \right) = 0.$$

Both modes localized at the Equator and modes spreading over the whole domain were found, which is in line with the numerical results Rieutord and Valdettaro (1997) got from inspection of a thick shell. According to these authors, it is viscosity which breaks the infinite degeneracy and helps to pick a unique eigenfunction for a given frequency. This remark in Rieutord and Valdettaro (1997) is based on the idea that the higher order derivatives appearing due to friction transform the hyperbolic problem into an elliptic problem. The latter one is well-posed and has an unique solution.

However, one may ask how this insight can be proved from discrete numerical computations, as one of their limitations is the absence of degeneracy. As the viscosity is small here, it seems just as possible that its impact is not sufficient to change the character of the problem. Indeed, the boundary layer solutions from section 7.4 still had an infinite number of degrees of freedom causing degeneracy, namely the amplitudes a_n in eq. (7.2.6) and the phase ϕ in eq. (7.4.7). The nature of this phase remains unclear, which could be a hint that the $y - z-$ frame is a bad choice for boundary layer theory, too. Consequently, the predicted boundary layer separation at the critical latitudes would not exist. In the end, only laboratory experiments and observations can be decisive.

It was shown that modes localized at the Equator can be excited even by an asymmetric off-equatorial forcing, and the dimensionless forcing strength is predicted to be proportional to $\frac{1}{\omega}$ from the equations. Again, the most important open question is under what conditions these localized modes form. Still, more theoretical work needs to be done in this regard.

Finally, the origin of the blurring effects described in section 8.3 should be inspected in the future. Raising the computer power and consequently the resolution then might reveal a fine structure or small discontinuities.

Chapter 9

Conclusion

The present work has been dedicated to the dynamics of equatorial waves. In particular, the possibilities of incorporating the full Coriolis force have been inspected, an approach that is rarely pursued in literature. The problem seems to be simple, but as mostly in earnest science, there is no definite answer. Even worse, there are different opinions as this is an active field of research.

After summarizing the results achieved in section 9.1, another contribution to this discussion will be given in section 9.2 by posing possible implications of this study on current and further research.

9.1   Summary

Chapter 2 has introduced the approximations commonly used to render our problems accessible to analytical approaches. The derivation of the traditional shallow water equations has been inspected, which is based on scale analysis and drops the angular velocity components that lie in the $\beta-$plane. Clearly, these give the largest contributions in an equatorial $\beta-$plane. It has been found that the underlying scale analysis applies to square domains, and hence, it might be incorrect at the Equator.

Surface and interface waves.   The *traditional shallow water equations* form the basis of the classical equatorial wave theory described by Matsuno (1966), which has been reviewed in chapter 3. This approach focuses on trapped waves by definition, as an asymptotic boundary condition $\lim_{y \to \pm \infty} \vec{u} = 0$ is used. The reduced gravity model uses the modes found by Matsuno to describe waves traveling along the thermocline. The resulting phase velocity matches well with observations, as it is about two orders of magnitude lower than the phase velocity of the corresponding surface waves. However, it has been found that these waves do not satisfy the proper kinematic and dynamic boundary conditions at the sea surface, but rather, the surface elevation is determined by the thermocline elevation via eq. (3.2.3). Out of a whole bunch of waves arising in this model, only equatorial Kelvin waves and long Rossby waves are needed to explain observations like in figure 3.1.

The question whether equatorial Kelvin waves can still exist if the full Coriolis force is taken into account has been addressed in chapter 4. Solutions have been constructed by means of stream function-based methods, but they turn out to be incompatible with rigid boundaries like the sea bottom. Interestingly, they split into a co-rotating and a contra-rotating mode whose wave lengths are shortened and prolonged, respectively. It has been demonstrated that nontraditional equatorial Kelvin waves can exist only as deep water waves ($k \gg \frac{1}{D}$) that decay exponentially away from the sea surface. Traditional equatorial Kelvin waves have been recovered in the limit of high frequencies, $\omega \gg 2\Omega$, contrary to what is expected from Matsuno's theory. The bottom line is that nontraditional equatorial Kelvin waves can exist in theory, but their predicted properties do not match with observations like those illustrated in figure 3.1.

Solutions resulting from the quest for nontraditional waves with a non-zero meridional velocity component have been inspected in chapter 5. Due to their vertical structure, they cannot be transformed into Matsuno's solutions by taking some suitable limit. These waves suffer even more from the inability to satisfy proper boundary conditions in the vertical, making it unlikely that they play a role in the ocean. A peculiar similarity between their spatial pattern through all orders and the lowest order Rossby waves of Matsuno (1966) has been pointed out, which would make an observational distinction hard if these waves existed in reality. It has been found that the vertical and meridional components of the problem are not separable anymore upon adding the nontraditional Coriolis terms to an equatorial $\beta-$plane model. Consequently, it is not possible anymore to apply asymptotic boundary conditions in the meridional direction while demanding a rigid bottom and a material surface on top.

Internal waves. In chapter 6, the properties of mixed inertial-internal gravity waves have been recapitulated. As their frequency depends only on the angle between wave vector and rotation axis, inertial waves show an infinite degeneracy. In case of the full Coriolis force acting in a rotating spherical shell, Stewartson and Rickard (1969) firstly reported on divergences at the critical latitudes[1] $\hat{y} = \pm\hat{\omega}$ in the second-order solutions of a formal power series in terms of the thickness of this shell. It has been revealed that already the underlying lowest-order solutions (Haurwitz waves) exhibit divergences, though at the poles. Wave attractors have been introduced with a particular example from literature which demonstrates that this astonishing phenomenon can lead to self-similar focusing of internal waves upon exciting them in an irregular geometry.

Stern's equation has been inferred in chapter 7 using fully anisotropic length scales but two different velocity scales. Though this is a minor change, the coverage of Stern's equation has been extended in this way as the used scales match very well with the situation at the Equator. It has been derived that solutions to Stern's equation beneath *a single rigid surface* are uniquely determined by the (partial) pressure on this surface, as this pressure is mapped to the domain via the characteristic curves. A periodicity condition has been inferred from the particular form of the characteristic coordinates. It allows to describe the stream function as a composition of a Fourier series and the characteristic curves. In case of an additional bottom surface in a *meridionally unbounded* domain, a proof has been given that no inviscid and physically meaningful solutions exist due to discontinuities. Starting from the previously derived composite stream function, a viscous bottom boundary layer has been added. In this way, analytical solutions to Stern's equation in case of small viscosity have been constructed. The boundary layer however blows up around the critical latitudes $\hat{y} = \pm\hat{\omega}$, leading there to discontinuities. A phase factor controlling the relation between both sides of the critical latitudes has been spotted, its nature is yet unclear.

Numerical solution schemes for Stern's equation have been explored in Chapter 8. For an existing method, the resolution attainable has been increased significantly. As a result, reflections and distortions in the stream function patterns have been discovered at the critical latitudes $\hat{y} = \pm\hat{\omega}$. Their occurrence is contrary to the theory from chapter 6, which rules out turning surfaces in a homogenous nontraditional setting. However, a suitable algorithm that solves the spatial wave equation in a curvilinear geometry has been developed which overcomes these problems. Slight uniform blurring occurs, but the overall structure is in very good agreement with the stream function patterns Harlander and Maas (2007) constructed from fundamental intervals. Both patterns that are strongly localized around the Equator (equatorial attractors) and patterns spreading over the whole domain (global attractors) have been found. In a first attempt towards the numerical description of forced motion, it has been shown that even a asymmetric off-equatorial forcing can excite equatorial attractors.

---

[1]Here, the scaling adopted in chapter 7 is used again.

9.2   Implications

Firstly, it is remarkable that the well-established textbook theory (Matsuno, 1966) on equatorial waves cannot be generalized to include the full Coriolis force, but rather breaks down. Apparently, the reason is the coupling between vertical and meridional coordinates caused by the non-traditional terms. This coupling entails that the vertical coordinate is not accessible for a boundary condition of its own, contrary to what has been incorrectly claimed by Fruman (2009).

Consequently, boundary conditions are an intrinsic issue of non-traditional approaches, though it should not be forgotten that the reduced gravity model suffers from similar problems as recapitulated in the preceding section. The prerequisite to rely on the reduced gravity model in order to apply the classical theory to the ocean beclouds this seemingly self-contained and appealing theory: a motionless layer underneath the thermocline (that is, below a few hundred meters) clearly does not agree with the observed deep jets and deep waves. A different concept for translating the classical theory to the ocean used, for example, by Hua et al. (2008) assumes a constant stratification (N = const.) and separates the vertical dependence by means of a structure function. This allows for vertically variable motion in the entire water column, but the thermocline is lost in return. Finally, the classical theory is unsuitable to explain equatorial trapping of waves because it plainly presumes that the velocity vanishes asymptotically for high latitudes.

A further issue encountered in two rather different contexts during this study are the pitfalls of the method of asymptotic expansions, where small details can have striking effects. In the first case, Dellar and Salmon (2005) set up a formal power series expansion in the aspect ratio δ to compute higher order non-traditional corrections to the classical solutions. However, taking into account the preceding considerations about the coupling of coordinates, it seems highly probable that only the trivial solution exists for the full problem with Matsuno's boundary conditions. One may ask, however, how significant a sum of the first three terms of an infinite series is when this infinite series adds up to zero.

The second case takes us already into the field of internal waves in a rotating fluid enclosed by a spherical shell. The lowest-order solutions in the formal power series expansion used by Stewartson and Rickard (1969) have been found to be always divergent at the poles. Hence, the quantization condition they impose on the frequency is superfluous because it is incapable of completely regularizing the lowest-order solutions. This is crucial as such a quantization condition would persist throughout all higher orders. In this regard, the second order divergencies at the critical latitudes $\hat{y} = \pm\hat{\omega}$ described by these authors appear less special.

During this study, these critical latitudes have turned up unexpectedly in two further situations: firstly, in the boundary layer solutions in Stern's equation where they are accompanied by the ominous phase factor mentioned above. Secondly, in the direct numerical solutions of Stern's equation where they form a barrier for the rays and pretend strong trapping. As the latter case frankly contradicts theory and can be overcome by a better choice of coordinates, one may ask whether the choice of coordinates might also be the reason in the other two situations. Hence, it would be an interesting question for further research to look for analytical boundary layer solutions of the spatial wave equation on a curved domain, similar to what has been done for the numerical part.

This would be worth a try because it might explain deep jets in a more direct way by trapping of internal waves that thereupon feed a main flow. Other approaches like Hua et al. (2008) have to make a detour via baroclinic instability of traditional equatorial Rossby and Kelvin waves which face the flaws described above. It is noted once again that the scales leading to Stern's equation are more realistic in regard of the equatorial area than the scales leading to the shallow water equations. With this new comprehension, equatorial wave attractors may play the key part in focusing the wave action towards the Equator. It is interesting that the forcing could originate from the ocean's interior (not necessarily at the Equator) through processes such as a tide hitting a bottom topography, whereas the spatial pattern of the attractor would be controlled by the pressure distribution at the surface (which however does not constitute a forcing). These considerations are roughly in line with the observational results by Brandt et al. (2011), though these authors provide a different explanation.

In addition to the studies on boundary layer solutions suggested above, some further efforts need

to be made in order to achieve better understanding of these phenomena. On the one hand, the same problems with discontinuities that arise in meridionally unbounded non-convex domains could put additional constraints on the method of fundamental intervals (Harlander and Maas, 2007) in case of meridionally bounded non-convex domains.

On the other hand, the enhancement of numerical methods is of outmost importance as they provide an independent test of the theory, as shown sometimes with surprising results. Moreover, they make it possible to incorporate stratification which, up to now, is hardly possible with analytical methods. In numerical methods, creative new ideas are necessary in order to make the values controllable that are attained by the partial pressure at the boundaries and to adequately describe the degeneracy caused thereby.

Appendix A

A.1 Fully anisotropic scales

By using for the three spatial directions both three different velocity scales as well as three different length scales, the lowest order system does not even lead to a pressure equation in most of the cases. One criterion to get a pressure equation seems to be that the buoyancy equation (7.1.1c) should not involve the small parameter used for an asymptotic expansion, i.e. the buoyancy terms are still present in lowest order of such an expansion. Doing so, a pressure equation is gained in the example presented here. It however suffers from being always elliptic, and hence, it does *not* exhibit internal wave solutions.

Dimensionless quantities are introduced in the set of equations (7.1.1a)-(7.1.1e) according to

$$x = L\hat{x} \qquad y = B\hat{y} \qquad z = D\hat{z} \qquad \omega = 2\Omega\frac{D}{L}\hat{\omega} \qquad N = 2\Omega\hat{N}$$

$$u = U\hat{u} \qquad v = \frac{B}{L}U\hat{v} \qquad w = \frac{D}{L}U\hat{w} \qquad \tilde{p} = 2\Omega U D\varrho_*\hat{p} \qquad b = \frac{UN^2}{2\Omega}\hat{b}.$$

Upon inserting these scales, the aspect ratio $\delta = D/L$ remains the only parameter in the resulting set of equations:

$$-i\hat{\omega}\hat{u} - \hat{y}\hat{v} + \hat{w} = -\hat{p}_{\hat{x}} \tag{A.1.1a}$$

$$-i\delta\hat{\omega}\hat{v} + \hat{y}\hat{u} = -\hat{p}_{\hat{y}} \tag{A.1.1b}$$

$$-i\hat{\omega}\left(\delta^2 - \frac{\hat{N}^2}{\hat{\omega}^2}\right)\hat{w} - \hat{u} = -\hat{p}_{\hat{z}} \tag{A.1.1c}$$

$$\hat{u}_{\hat{x}} + \hat{v}_{\hat{y}} + \hat{w}_{\hat{z}} = 0 \tag{A.1.1d}$$

The buoyancy equation reads again $-i\hat{\omega}\hat{b} + \hat{w} = 0$, and b is already eliminated in the usual way from the third momentum equation. By means of an asymptotic power series expansion $\vec{u} = \vec{u}^0 + \delta\,\vec{u}^1 + \cdots$ and $p = p^0 + \delta\,p^1 + \cdots$, the lowest order balance reads after dropping the hats:

$$-i\omega u^0 - yv^0 + w^0 = -p_x^0 \tag{A.1.2a}$$

$$yu^0 = -p_y^0 \tag{A.1.2b}$$

$$i\frac{N^2}{\omega}w^0 - u^0 = -p_z^0. \tag{A.1.2c}$$

$$u_x^0 + v_y^0 + w_z^0 = 0 \tag{A.1.2d}$$

Now it is easy to express the velocities in terms of the pressure, yielding

$$u^0 = -\frac{p_y^0}{y}, \qquad v^0 = \frac{p_x^0}{y} + \frac{i\omega p_y^0}{y^2}(1 + \frac{1}{N^2}) + \frac{i\omega p_z^0}{yN^2} \qquad \text{and} \qquad w^0 = \frac{i\omega}{N^2}(p_z^0 + \frac{p_y^0}{y}).$$

The desired equation is obtained by inserting the latter relations into the continuity equation,

$$(1 + N^2)p_{yy}^0 + 2yp_{zy}^0 + y^2 p_{zz}^0 + i\frac{N^2}{\omega}p_x^0 - \frac{2}{y}(1 + N^2)p_y^0 - p_z^0 = 0.$$

In order to classify this equation, identify $A = 1 + N^2$, $B = y$ and $C = y^2$. Hence, the discriminant is $B^2 - AC = -y^2 N^2$, which means that the equation is always elliptic and shall not exhibit internal wave solutions.

A.2 Constants and spherical coordinates

Mean Earth radius r_0	$6.731 \cdot 10^6$ m
Angular speed of Earth's rotation $\Omega_\oplus$	$7.292 \cdot 10^{-5}$ $\frac{1}{s}$
Mean ocean depth $\overline{H}$	4 km

Table A.1: Constants

In oceanography, spherical coordinates (λ, φ, r) are usually defined such that the angular coordinates coincide with geographical longitudes and latitudes, as pointed out in section 2.3 and illustrated in figure 2.1. The following expressions are taken from Olbers et al. (2012) or converted from Bronstein and Semendjajew (2000), respectively.

$$
\begin{aligned}
x &= r\cos\varphi\cos\lambda \\
y &= r\cos\varphi\sin\lambda \\
z &= r\sin\varphi
\end{aligned}
$$

$$
\hat{e}_\lambda = \begin{pmatrix} -\sin\lambda 0 \\ \cos\lambda \\ 0 \end{pmatrix} \qquad
\hat{e}_\varphi = \begin{pmatrix} -\sin\varphi\cos\lambda \\ -\sin\varphi\sin\lambda \\ \cos\varphi \end{pmatrix} \qquad
\hat{e}_r = \begin{pmatrix} \cos\varphi\cos\lambda \\ \cos\varphi\sin\lambda \\ \sin\lambda \end{pmatrix}
$$

$$
\begin{aligned}
\nabla f &= \hat{e}_\lambda \frac{1}{r\cos\varphi}\partial_\lambda f + \hat{e}_\varphi \frac{1}{r}\partial_\varphi f + \hat{e}_r \partial_r f \\
\text{div } \vec{V} &= \frac{1}{r\cos\varphi}\partial_\lambda V_\lambda + \frac{1}{r}\left(\partial_\varphi - \tan\varphi\right)V_\varphi + \left(\frac{2}{r} + \partial_r\right)V_r \\
\triangle f &= \frac{1}{r^2\cos^2\varphi}\partial_\lambda^2 f + \frac{1}{r^2}\left(\partial_\lambda^2 - \tan\varphi\partial_\lambda\right)f + \left(\partial_r^2 + \frac{2}{r}\partial_r\right)f
\end{aligned}
$$

A.3   Exemplary MATLAB code for Stern's equation

```
% Compute and display the eigenfunctions to Stern's equation for a given interval of eigenvalues,
    that are in fact the squared frequencies


% Set meridional size of simulated area and resolution
ymax=1.4;
ystep=0.01;
zstep=0.005;


% Set eigenvalue interval of interest
min_eig=0.80;
max_eig=0.82;


% Create grid
y = −ymax:ystep:ymax;
nocol=2*ymax/ystep +1; % Number of columns
z = −1:zstep:0;
norow=1/zstep −1;        % Number of rows
Nmax=norow*nocol;        % Number of grid points


% Create sparse matrices representing the  differential  operators, pseudo−periodic boundary
    conditions in y−direction are incorporated
Syy=spdiags([ones(Nmax,1) ones(Nmax,1) −2*ones(Nmax,1) ones(Nmax,1) ones(Nmax,1)],[−(
    nocol−1)*norow −norow 0 norow (nocol−1)*norow],Nmax,Nmax);
Szz=spdiags([ones(Nmax,1) −2*ones(Nmax,1) ones(Nmax,1)],[−1 0 1],Nmax,Nmax);
Sz=spdiags([ones(Nmax,1) ones(Nmax,1)],[−1 1],Nmax,Nmax);
Syz=spdiags([−ones(Nmax,1) ones(Nmax,1) ones(Nmax,1) −ones(Nmax,1) −ones(Nmax,1) ones(
    Nmax,1) ones(Nmax,1) −ones(Nmax,1)],[ −(nocol−1)*norow−1 −(nocol−1)*norow+1 −norow
    −1 −norow+1 norow−1 norow+1 (nocol−1)*norow−1 (nocol−1)*norow+1],Nmax,Nmax);
% The coefficient y must become a matrix, too
Y=kron(spdiags(y',[0],nocol,nocol),speye(norow));



% Assemble matrices A and B
A=Syy/ystep^2 + Y^2*Szz/zstep^2+2*Y*Syz/(4*ystep*zstep) + Sz/(2*zstep);
B=speye(Nmax)*Szz/zstep^2;


% Incorporate vertical boundary conditions
for i = 1:norow:Nmax
    if i−1>0
                A(i,i−1)=0;
                B(i,i−1)=0;
        end;
        if i−1+norow<=Nmax
                A(i,i−1+norow)=0;
                B(i,i−1+norow)=0;
        end;
        if i−1−norow>0
                A(i,i−1−norow)=0;
                B(i,i−1−norow)=0;
        end;
```

```
end;
for i = norow:norow:Nmax
        if i+1<=Nmax
                A(i,i+1)=0;
                B(i,i+1)=0;
        end;
        if i+1+norow<=Nmax
                A(i,i+1+norow)=0;
                B(i,i+1+norow)=0;
        end;
        if i+1−norow>0
                A(i,i+1−norow)=0;
                B(i,i+1−norow)=0;
        end;
end;
A(norow*(nocol−1),1)=0;          % Still some single points left ...
A(1,norow*(nocol−1))=0;
A(Nmax,norow+1)=0;
A(norow+1,Nmax)=0;


% Solve generalized sparse eigenvalue problem
[xv,lmb,iresult ] = sptarn(A,B,min_eig,max_eig,0,1*eps,1000,10000);
% sptarn is part of the PDE toolbox − for details, consult the MATLAB documentation.
% The columns of xv are the eigenvectors, the entries of lmb the corresponding eigenvalues.
% iresult is the number of eigenvalues found − if iresult is positive, all eigenvalues have been
    found


% Create grid for plotting in the Y−Z−frame, in which the characteristic curves are straight lines
MY=4*ones(norow+2,1)*y;
MZ=2*(2*(z'*ones(1,nocol)) −(ones(norow+2,1)*y).^2 );


% Plot eigenfunctions on screen, press any key to go to next eigenfunction
for n=1:1:abs(iresult)
        % Some eigenvalues and eigenfunctions come as pairs of complex conjugated expressions
        % Here, simply the real parts are taken instead of adding them up pairwise
        R=[zeros(1,nocol);real(reshape(xv(:,n),norow,nocol));zeros(1,nocol)];
        pcolor(MY,MZ,R)
        shading interp
        title ([ '\omega_=_' num2str(sqrt(real(lmb(n))))]);
pause
end
```

A.4   Exemplary MATLAB code for the spatial wave equation

$\overline{\omega}$	Ystep	Ymax	Zstep	min_eig	max_eig	iresult
0.3676	0.034	10.88	0.025	0.134	0.137	180
0.5208	0.024	7.68	0.025	0.265	0.275	450
0.9025	0.0277	17.728	0.025	0.81	0.82	767

Table A.2: From the scans performed with these settings, figure 8.7 is taken. Here, $\overline{\omega}$ is the frequency for which the characteristic lines lie exactly on the grid points, and iresult is the number of eigenfunctions in the respective interval.

```
% Compute and display the eigenfunctions to the spatial wave equation for a given  interval  of
    eigenfrequencies

% Set eigenvalue interval  of  interest
min_eig=0.265;
max_eig=0.275;
% Set meridional size and resolution
Ymax=7.68;
Ystep=0.024;
Zstep=0.025;

% Create outer grid
Y = −Ymax:Ystep:Ymax;
nocol=floor(2*Ymax/Ystep +1);
Zmin=−ceil((Ymax.^2)/8+4);          % Vertical size  is  determined by Ymax
Z = Zmin:Zstep:0;
norow=−Zmin/Zstep +1;

% Determine inner grid area in which Psi is nonzero
ZS=−(Y.^2)/8;                       % Top
ZB=ZS−4;                            % Bottom
OFF=ceil((ZB−Zmin)/Zstep);          % Offset of each column with respect to  left  lower edge
HI=4/Zstep;                         % Height of the nonzero area
N=HI*nocol;                          % Number of points in the nonzero area
Nmax=norow*nocol;                   % Number of points in the total  area

% Create sparse matrices representing the  differential  operators
SYY=spalloc(N,N,3*N);               % empty matrices
SZZ=spalloc(N,N,3*N);
for j=1:1:nocol
      for k=1:1:HI                  % k is the row index in the nonzero area
            n=(j−1)*HI+k;           % Lexicographic index of grid  point  under  consideration

            SYY(n,n)=−2;            % First the  Y−derivative, set the diagonals
            if  j>1                     % If this  is  not the  first  column...
                  if and(−HI+k+OFF(j)−OFF(j−1)<1,−HI<−HI+k+OFF(j)−OFF(j−1))
                        SYY(n,(j−2)*HI+k+OFF(j)−OFF(j−1))=1; % ... then set the left
                        neighbour in SYY...
```

```
                        end
            else                              % ... else apply periodic bc's in y−direction to  first
                    column
                        SYY(n,(nocol−1)∗HI+k)=1;
            end
            if  j<nocol                   % If this  is not the  last  column...
                        if  and(k+OFF(j)−OFF(j+1)<HI+1,0<k+OFF(j)−OFF(j+1))
                                    SYY(n,j∗HI+k+OFF(j)−OFF(j+1))=1; % ...  then set  the  right
                                        neighbour in SYY...
                        end
            else                              % ... else apply periodic bc's in y−direction to  last
                    column
                        SYY(n,k)=1;
            end

                        SZZ(n,n)=−2;              % Now, the Z−derivative, set diagonals
            if  k>1                % If the point  is not at the bottom...
                        SZZ(n,n−1)=1; % ... set lower neighbour in SZZ
            end
            if  k<HI                          % If the point  is  not on top...
                        SZZ(n,n+1)=1; % ... set upper neighbour in SZZ
            end
        end
end

% Solve generalized sparse eigenvalue problem
[V,D,iresult ]  = sptarn(SYY,SZZ,0.81,0.82,0,1∗eps,10000,1000);
% sptarn is part of the PDE toolbox − for details,  consult  the  MATLAB documentation.
% The columns of V are the eigenvectors, the entries  of D the corresponding eigenvalues.
% iresult  is  the  number of eigenvalues found − if iresult  is  positive ,  all  eigenvalues have been
    found

% Create matrices containing the Y− and Z−coordinates of every grid point in the nonzero inner
    area
MY=ones(HI,1)∗Y;
clear MZ;
for  j =1:nocol
        MZ(1:HI,j)=Z((1+OFF(j)):(HI+OFF(j)))'; % Offset has to be taken into account
end

% Plot eigenfunctions on screen, press any key to go to next eigenfunction
for  i =1:1:abs(iresult )
        l=i
        R=real(reshape(V(:,l),HI,nocol));
        pcolor(MY,MZ,R)
        shading interp
        title ([ '\omega␣=␣' num2str(sqrt(real(D(l))))]);
        pause
end
```

Bibliography

Boulanger, J.-P., Fu, L.-L., 1996. Evidence of boundary reflection of Kelvin and first-mode Rossby waves from TOPEX/POSEIDON sea level data. Journal of Geophysical research 101, 16.361–16.371.

Brandt, P., Funk, A., Hormann, V., Dengler, M., Greatbatch, R. J., Toole, J. M., 2011. Interannual atmospheric variability forced by the deep equatorial Atlantic Ocean. Nature 473, 497–500.

Bretherton, F. P., 1964. Low frequency oscillations trapped near the equator. Tellus 16, 181–185.

Bronstein, I. N., Semendjajew, K. A., 2000. Taschenbuch der Mathematik, 5th Edition. Harri Deutsch, Frankfurt am Main.

Bryan, G., 1889. The waves on a rotating liquid spheroid of finite ellipticity. Philosophical Transactions of the Royal Society 180, 187–219.

Chelton, D. B., Schlax, M. G., 1996. Global observations of oceanic Rossby waves. Science 272, 234–238.

Chorin, A., 1992. A Mathematical Introduction to Fluid Mechanics, 3rd Edition. Springer, New York.

Courant, R., Hilbert, D., 1968. Methoden der Mathematischen Physik II, 2nd Edition. Springer, Berlin.

Dellar, P. J., Salmon, R., 2005. Shallow water equations with a complete Coriolis force and topography. Physics of Fluids 17, 106601.

Dengler, M., Quadfasel, D., 2002. Equatorial deep jets and abyssal mixing in the Indian Ocean. Journal of Physical Oceanography 32, 1165–1180.

Dijkstra, H. A., 2008. Dynamical Oceanography. Springer, Berlin.

Dijkstra, H. A., Burgers, G., 2002. Fluid dynamics of El Niño variability. Annual Review of Fluid Mechanics 34, 531–558.

Friedlander, S., Siegmann, W. L., 1982. Internal waves in a rotating stratified fluid in an arbitrary gravitational field. Geophysical and Astrophysical Fluid Dynamics 19, 267–291.

Fruman, M. D., 2009. Equatorially bounded zonally propagating linear waves on a generalized beta-plane. Journal of the atmospheric sciences 66, 2937–2945.

Gerkema, T., Zimmerman, J. T. F., Maas, L. R. M., van Haren, H., 2008. Geophysical and astrophysical fluid dynamics beyond the traditional approximation. Review of Geophysics 46, RG2004.

Gill, A. E., 1982. Atmosphere-Ocean Dynamics. Academic Press, New York.

Harlander, U., Maas, L. R. M., 2006. Characteristics and energy rays of equatorially trapped, zonally symmetric internal waves. Meteorologische Zeitschrift 15, 439–450.

Harlander, U., Maas, L. R. M., 2007. Internal boundary layers in a well-mixed equatorial atmosphere/ocean. Dynamics of Atmospheres and Oceans 44, 1–28.

Haurwitz, B., 1940. The motion of atmospheric disturbances on the spherical earth. Journal of Marine Research 3, 254–267.

Heuser, H., 1998. Lehrbuch der Analysis Teil 1, twelfth Edition. Vieweg+Teubner, Wiesbaden.

Hua, B. L., D'Orgeville, M., Fruman, M. D., Menesguen, C., Schopp, R., Klein, P., Sasaki, H., 2008. Destabilization of mixed Rossby gravity waves and the formation of equatorial zonal jets. Journal of Fluid Mechanics 610, 311–341.

Hughes, B., 1964. Effect of rotation on internal gravity waves. Nature 201, 798–801.

LeBlond, P. H., Mysak, L. A., 1978. Waves in the Ocean, 1st Edition. Elsevier, Amsterdam.

Maas, L. R. M., 2009. Exact analytical self-similar solution of a wave attractor field. Physica D (Nonlinear Phenomena) 238, 502–505.

Maas, L. R. M., Benielli, D., Sommeria, J., Lam, F.-P. A., 1997. Observation of an internal wave attractor in a confined, stably stratified fluid. Nature 388, 557–561.

Maas, L. R. M., Harlander, U., 2007. Equatorial wave attractors and inertial oscillations. Journal of Fluid Mechanics 570, 47–67.

Maas, L. R. M., Lam, F.-P. A., 1995. Geometric focusing of internal waves. Journal of Fluid Mechanics 300, 1–41.

Manton, M. J., Mysak, L. A., 1971. Construction of internal wave solutions via a certain functional equation. Journal of Mathematical Analysis and Applications 35, 237–248.

Matsuno, T., 1966. Quasi-geostrophic motions in the equatorial area. Journal of the Meteorological Society of Japan 44, 25–43.

Newman, M. E. J., Barkema, G. T., 1999. Monte Carlo Methods in Statistical Physics, 1st Edition. Oxford University Press, Oxford.

Noir, J., Jault, D., Cardin, P., 2001. Numerical study of the motions within a slowly precessing sphere at low Ekman number. Journal of Fluid Mechanics 437, 283–299.

Oglivie, G. I., 2005. Wave attractors and the asymptotic dissipation rate of tidal disturbances. Journal of Fluid Mechanics 543, 19–44.

Olbers, D., Willebrand, J., Eden, C., 2012. Ocean Dynamics. Springer, Berlin.

Quarteroni, A., Sacco, R., Saleri, F., 2000. Numerical Mathematics. Springer, New York.

Raymond, W. H., 2001. Kelvin waves: rotationally induced circulations. Dynamics of Atmosphere and Ocean 34, 23–43.

Rieutord, M., Valdettaro, L., 1997. Inertial waves in a rotating spherical shell. Journal of Fluid Mechanics 341, 77–99.

Roberts, P. H., Stewartson, K., 1963. On the stability of a Maclaurin spheroid of small viscosity. Astrophysical Journal 137, 777–790.

Roundy, P. E., Janiga, M. A., 2012. Analysis of vertically propagating convectively coupled equatorial waves using observations and a non-hydrostatic Boussinesq model on the equatorial beta-plane. Quarterly Journal of the Royal Meterological Society 138, 1004–1017.

Stern, M. E., 1963. Trapping of low-frequency oscillations in an equatorial 'boundary layer'. Tellus 15, 246–250.

Stewartson, K., Rickard, J. A., 1969. Pathological oscillations of a rotating fluid. Journal of Fluid Mechanics 35, 759–773.

Sutherland, B. R., Dalziel, S. B., Hughes, G. O., Linden, P. F., 1999. Visualization and measurement of internal waves by synthetic schlieren. Journal of Fluid Mechanics 390, 93–126.

Thomson, W., 1879. On gravitational oscillations of rotating water. Proceedings of the Royal Society of Edinburgh 10, 92–100.

Winters, K. B., Bouruet-Aubertot, P., Gerkema, T., 2011. Critical reflection and abyssal trapping of near-inertial waves on a beta-plane. Journal of Fluid Mechanics 684, 111–136.

Zhang, K., Earnshaw, P., Liao, X., Busse, F. H., 2001. On inertial waves in a rotating fluid sphere. Journal of Fluid Mechanics 437, 103–119.